

ABSTRACT

Fundamental Particle and Wave Dynamics in Dusty Plasmas

Zhuanhao Zhang, Ph.D.

Mentor: Truell W. Hyde, Ph.D.

Dusty plasma is a low-temperature plasma containing dust particles varying in size from nanometers to micrometers. Due to plasma fluxes to its surface, a dust particle will charge negatively or positively depending on the charging mechanism involved. The motion of a dust particle within a dusty plasma can be recorded using a video camera, allowing for examination of the particle dynamics at the kinetic level.

Any investigation of dusty plasmas first requires a proper understanding of the fundamental particle-particle interaction, dust particle charge and screening length. Due to the perturbative nature of the majority of diagnostics in common use, all of these are difficult to measure properly.

Each of the fundamental parameters mentioned above are addressed in this thesis. First a minimally perturbative technique, allowing experimental detection of each of these parameters, will be introduced. Next, a study of vertically aligned, extended dust particle chains employing a glass box placed on the lower powered electrode in a ground-based RF plasma system will be discussed. Finally, by adjusting the discharge power and the gas pressure within the plasma chamber, it will be shown that a chaotic dust cloud can

form such vertical chains as well as self-excited dust acoustic waves. An investigation of both the particle and wave dynamics within various sizes of glass box and under a number of plasma conditions will be presented. A theoretical model is also introduced providing a comprehensive dispersion relationship for dust acoustic waves (DAWs) and examining the instabilities resulting from the effects created by the dust temperature, particle charge variation, and ion-drag-force fluctuations. It is shown that each plays a different role depending on the wavelength regime considered.

Fundamental Particle and Wave Dynamics in Dusty Plasmas

by

Zhuanhao Zhang, Ph.D

A Dissertation

Approved by the Department of Physics

Gregory A. Benesh, Ph.D., Chairperson

Submitted to the Graduate Faculty of
Baylor University in Partial Fulfillment of the
Requirements for the Degree
of
Doctor of Philosophy

Approved by the Dissertation Committee

Truell W. Hyde, Ph.D., Chairperson

Lorin S. Matthews, Ph.D.

Anzhong Wang, Ph.D.

Dwight P. Russell, Ph.D.

Manfred Dugas, Ph.D.

Accepted by the Graduate School
August 2012

J. Larry Lyon, Ph.D., Dean

Copyright © 2012 by Zhuanhao Zhang

All rights reserved

TABLE OF CONTENTS

LIST OF FIGURES.....	vii
LIST OF TABLES.....	xi
ACKNOWLEDGMENTS.....	xii
CHAPTER ONE.....	1
Introduction.....	1
1.1. Plasma	1
1.2. Dusty Plasma.....	4
1.3. Structure of the Dissertation.....	8
CHAPTER TWO.....	11
Basic Theory of Dusty Plasmas.....	11
2.1. Introduction.....	11
2.2. Dusty Plasmas in Laboratory	11
2.3. Debye Shielding.....	14
2.4. RF Plasma Sheath.....	16
2.5. Particle Charging Mechanisms.....	18
2.6. Forces on Particles.....	31
2.7. Waves in Dusty Plasmas.....	46
CHAPTER THREE.....	56
Experiment Setup.....	56
3.1. Introduction.....	56
3.2. GEC RF Reference Cell.....	56
3.3. CASPER GEC RF Reference Cell.....	60
3.4. RF Power Setup.....	67
3.5. DC Bias.....	69
CHAPTER FOUR.....	72
Particle Interaction Measurements.....	72
4.1. Introduction.....	72
4.2. Previous Contributions.....	73
4.3. Dependence on Gas Pressure.....	79
4.4. Single Particle Technique.....	79
4.5. Particle Motion in the Vertical Direction.....	81
4.6. Particle Motion in the Horizontal Direction.....	83
4.7. Interaction Potential Relationship to Neutral Gas Pressure.....	87
4.8. Conclusions.....	91

CHAPTER FIVE.....	94
Oscillation and Instability in Glass Box Confinement.....	94
5.1. Introduction	94
5.2. Applications of Glass Boxes in Dust Plasmas.....	95
5.3. 1-D Vertical Dust String in a Glass Box.....	96
5.4. Dust Acoustic Waves and Instabilities inside a Glass Box.....	106
CHAPTER SIX.....	127
Effects on the Dispersion Relation for DAW.....	127
6.1. Introduction.....	127
6.2. Previous Investigation of Effects on Dispersion Relation of DAW.....	128
6.3. Plasma and Dust Particle Parameters.....	130
6.4. Fluid Model Analysis.....	133
6.5. Analysis and Discussion.....	139
6.6. Conclusions.....	153
CHAPTER SEVEN.....	155
Summary and Outlook.....	155
BIBLIOGRAPHY.....	160
APPENDIX.....	172

LIST OF FIGURES

Figure 1.1: Process of state of H ₂ O from ice to plasma	2
Figure 1.2: Plasma parameters for various types of plasmas.....	2
Figure 1.3: Solar flares.....	2
Figure 1.4: Eagle Nebula.....	2
Figure 1.5: Comet tails.....	5
Figure 1.6: Saturn's rings.....	5
Figure 1.7: Dust particles suspended above silicon wafers.....	6
Figure 1.8: Killer particle.....	6
Figure 1.9: Top and side view of plasma crystals.....	7
Figure 1.10: Dust void under microgravity.....	8
Figure 2.1: DC discharge experimental setup.....	12
Figure 2.2: Capacitively coupled RF discharge experimental setup.....	14
Figure 2.3: Grazing collisions between plasma particles and dust particles.....	20
Figure 2.4: Dimensionless charge number in different gas plasmas.....	23
Figure 2.5: Dimensionless charge number as a function of ion drift	27
Figure 2.6: Dimensionless charge number as a function of Mach cone number	29
Figure 2.7: Dimensionless charge number as a function of collisionality index.....	30
Figure 2.8: Ion drag force.....	40
Figure 2.9: Simulated ion density distribution.....	42
Figure 2.10: Scheme of particle trapping experiments.....	44
Figure 2.11: Positions of two aligned particles when one was pushed.....	44

Figure 2.12: Horizontal component of the attractive force.....	45
Figure 2.13: Scheme of a lower electrode and attractive potentials.....	45
Figure 2.14: Phase diagram of Yukawa system.....	48
Figure 2.15: Phases and amplitudes of the particle oscillations.....	50
Figure 2.16: Theoretical and experimental dispersion relation.....	51
Figure 2.17: Image of a DAW pattern.....	52
Figure 2.18: Measured DAW dispersion relation.....	54
Figure 3.1: Photograph of the GEC RF reference cell main chamber.....	57
Figure 3.2: Photograph of a GEC RF reference cell sustaining a plasma.....	58
Figure 3.3: Schematic of a GEC RF reference cell.....	59
Figure 3.4: Pumps and mass flow control units.....	61
Figure 3.5: Schematic of the CASPER GEC RF reference cell vacuum system.....	62
Figure 3.6: Photographs of pump-out manifold and PVC tube.....	62
Figure 3.7: Photograph of an air bag.....	63
Figure 3.8: Photographs of a cutout and a glass box.....	64
Figure 3.9: CCP RF discharge and high speed camera in a CASPER cell.....	65
Figure 3.10: Locations of cameras, lasers and motors of a CASPER cell.....	67
Figure 3.11: Schematic of the RF power system.....	69
Figure 3.12: Schematic of the RF power system with variable DC bias.....	70
Figure 4.1: Experimental setup and potential energy of a dust particle.....	74
Figure 4.2: Experimental configuration and the attractive and repulsive forces.....	76
Figure 4.3: Cutout plate.....	80
Figure 4.4: Trajectory and spectrum of a falling particle.....	82

Figure 4.5: Measured drag coefficient.....	83
Figure 4.6: Trajectories of center of mass and relative motion.....	85
Figure 4.7: Measured horizontal potential energy.....	86
Figure 4.8: Measured interaction potential energy.....	87
Figure 4.9: Confining and interaction potentials at various pressures.....	88
Figure 4.10: Particle charge and screening length as functions of pressure.....	89
Figure 4.11: Theoretical and experimental normalized particle charge number.....	90
Figure 5.1: Superposition of forces and photographs of a Coulomb ball.....	95
Figure 5.2: Formation of a vertical string.....	98
Figure 5.3: Construction of propagating wave within a dust string.....	99
Figure 5.4: Oscillation spectra of a vertical string.....	101
Figure 5.5: Distribution of oscillation parameters.....	102
Figure 5.6: Relative phase distribution within a string.....	103
Figure 5.7: Linear phase fit and dispersion relation.....	104
Figure 5.8: Side view images of formation of a DAW.....	110
Figure 5.9: Conditions for creating DAWs.....	110
Figure 5.10: Image of a dust cloud inside a glass box.....	111
Figure 5.11: Space-time diagram for the cropped region.....	112
Figure 5.12: Spectrum in frequency domain.....	113
Figure 5.13: Phase distribution within a dust cloud.....	114
Figure 5.14: Power spectrum for DAWs in the dust cloud.....	114
Figure 5.15: Frequencies and wave numbers of DAWs in the dust cloud.....	115
Figure 5.16: Amplitudes of DAWs within the dust cloud.....	116

Figure 5.17: Growth rates of DAWs.....	117
Figure 5.18: Space-time diagram.....	118
Figure 5.19: Phases of the fundamental and harmonics of a DAW.....	118
Figure 5.20: Amplitudes of the fundamental and harmonics of a DAW.....	120
Figure 5.21: Exponential fit for the development of wave amplitudes.....	120
Figure 5.22: The energy index distribution	120
Figure 5.23: The initial growth point.....	123
Figure 5.22: The frequency spectra for self-excited and driven DAWs.....	126
Figure 6.1: Parameters for dust particles and plasma.....	134
Figure 6.2: Dust temperature function.....	141
Figure 6.3: Critical dust temperature.....	142
Figure 6.4: Normalized dispersion relation of a DAW considering dust temperature....	143
Figure 6.5: Normalized dispersion relation of a DAW considering charge effect.....	144
Figure 6.6: Normalized dispersion relation considering ion-drag-force fluctuation.....	146
Figure 6.7: Normalized dispersion relation considering all three effects.....	148
Figure 6.8: Comparison between theoretical and experimental results.....	150
Figure 6.9: Normalized dispersion relation under experimental conditions	151

LIST OF TABLES

Table 5.1: Experimental observations of DAWs.....	107
Table 6.1: Dust and plasma parameters.....	147

ACKNOWLEDGMENTS

None of the work presented in this thesis would have been possible without the impeccable support and guidance of many people, who I would like to express my thankfulness to.

First of all, I would like to thank my supervisor, Dr. Truell Hyde, for his support, patience and wisdom. During the past four years, the scientific discussions with you always broke the ice on my way to make progress. I thank you for the guidance, the encouragement and the freedom you gave me during the process. And also thank you for building such a wonderful research group at Center for Astrophysics, Space Physics and Engineering Research to make everything possible.

I also would like to express my gratitude to Dr. Lorin Matthews for extensive editing my papers and thesis and giving many suggestions by taking out of time from her busy schedules.

I am thankful for the scientific discussions from Dr. Jie Kong, Dr. Ke Qiao, and Dr. Victor land. Your research experience and many inspiring suggestions saved me a lot of time and make key results out of data ocean. I have learnt a lot from you guys.

I also thank Jorge Carmona Reyes for his patience and invaluable support in the lab and also in the Physics Circus. Jorge, you did a wonderful job. The talks with you about life stories in America filled my life here with many excited moments.

I'd also like to express my gratitude to my colleagues, Angela Douglass, Brandon Hariss, James Creel and Jay Murphree, who helped me through the process by listening to my research ideas and giving comments.

I'd like to thank Mike Cook and Jimmy Schmoke for keeping the experimental apparatus running properly.

I'd like to thank Dr. Anzhong Wang, Dr. Dwight Russell, and Dr. Manfred Dugas for agreeing to be seated in my dissertation committee.

Thank you all!

CHAPTER ONE

Introduction

1.1. Plasma

Plasma is the fourth and the most common state of matter, composing 99% of the visible universe. Plasmas are conductive assemblies of electrons, ions and neutral molecules. One of the main properties of plasma is the collective effect, in which charged particles interact with each other through the Coulomb force. Any single moving charged particle will also interact with its neighbors, resulting in polarization of the medium and the establishment of a local electric field. In return, nearby particles will move collectively to reduce this electric field. This is called the “collective effect.” Another important property of plasma is quasi-neutrality. If any deviation from neutrality emerges, the electrostatic interaction with ions and electrons will create a local electric field or current compensating the non-neutrality.

Plasma is the “hottest” state of matter. External energy is required to peel electrons from neutral atoms and generate plasma. Figure 1.1 illustrates the process of states of H₂O from ice to plasma. Plasma parameters vary across a large range; for example, the plasma density can be as low as 10^{-10} m^{-3} in space and as high as 10^{27} m^{-3} in some fusion reactors. Figure 1.2 shows common density and temperature ranges for different types of plasmas in the Universe. However, plasmas having parameters far beyond the ones illustrated also exist.

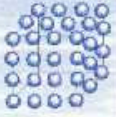



Solid	Liquid	Gas	Plasma
Example Ice H_2O	Example Water H_2O	Example Steam H_2O	Example Ionized Gas $H_2 \rightarrow H^+ + H^+ + 2e^-$
Cold $T < 0^\circ C$	Warm $0 < T < 100^\circ C$	Hot $T > 100^\circ C$	Hotter $T > 100,000^\circ C$ > 10 electron Volts
			
Molecules Fixed in Lattice	Molecules Free to Move	Molecules Free to Move, Large Spacing	Ions and Electrons Move Independently, Large Spacing

FIG. 1.1. Process of state of H_2O from ice to plasma. (Courtesy of General Atomics.)

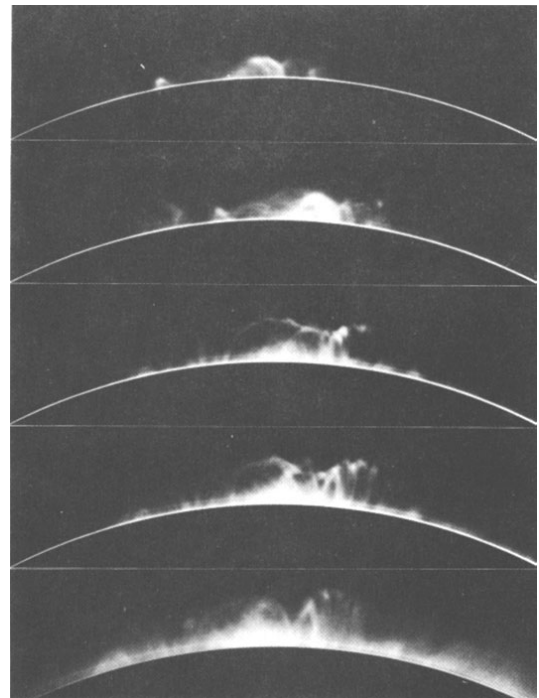


FIG. 1.3. Series of pictures showing plasma arches which are believed to mark the solar magnetic field after a major flare. (Eliezer S., Eliezer Y., 2001)

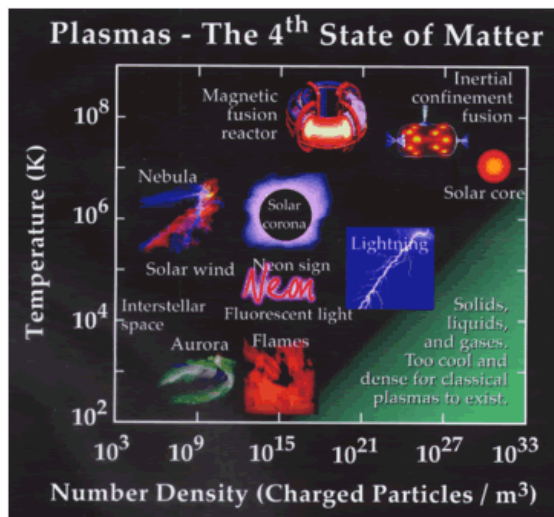


FIG. 1.2. Plasma parameters for various types of plasmas. (Courtesy of www.plasmas.org.)



FIG. 1.4. Star formation in the Eagle Nebula. (Courtesy of Space Telescope Science Institute, NASA.)

During the formation and explosion of *stars*, the composition of the materials is mostly in the plasma state. Figure 1.4 shows plasma during star formation in the Eagle Nebula as observed by the Hubble Space Telescope. *Solar flares* on the surface of the sun strongly affect solar winds and are eruptions of hot plasma which is believed to map the surface magnetic field of the sun. In Fig. 1.3, the occurrence and disappearance of solar flares is shown (Eliezer S. and Eliezer Y., 2001).

On earth, almost all plasmas are man-made, except a few natural phenomenon such as lightning, aurora, etc. The applications of plasma in industry broaden and enhance our ability to manufacture products. One of the primary advantages of plasma application in industry is associated with its high power density. For example, in DC electrical arcs or RF inductive plasma torches, the plasma power density can range from 100 W/cm^3 to 10 kW/cm^3 . Such plasmas are in thermodynamic or thermal equilibrium at high temperature and are capable of melting or even vaporizing materials. This is to their advantage in thermal plasma processing; for example, welding, plasma flame spraying, arc furnaces and other high temperature applications (Roth 2001).

Plasma-related techniques can also significantly increase the efficiency of energy consumption. This may allow them to eventually replace some of the chemical-related industries which can contribute to pollution or global warming problems. Plasma etching processing for microelectronics is also a widely applied technique in semiconductor production. This etching processing can be achieved using acids in a liquid state (“wet etching”) or using plasma (“dry etching”). The latter approach is faster, cleaner, and more accurate since current chip production requires etching within a highly anisotropic environment. In a plasma medium, atoms and molecules are excited to radiate efficiently

in any desired direction (anisotropic). Dry processing is required for small separation between circuit elements. Since a critical electronic device is of the order of one micron, a dry processing technique such as plasma etching is suitable manufacturing (Eliezer S. and Eliezer Y., 2001). Thus, plasma etching has become a highly regarded technique in modern semiconductor.

1.2. Dusty Plasma

Dusty plasma, also called “complex” plasma, consists of an ordinary low temperature plasma containing nanometer to micrometer-size particles suspended in it. Over the past two decades, interest in dusty plasma research has increased significantly. The initial driving motivation for this was primarily due to two main fields: astronomy and plasma industry. Recent discussion of applications of dusty plasma in others fields such as colloidal chemistry (Hollenstein 2000), granular materials (Hörlück and Dimon 1999), nanotechnology (Bouchoule 1999), and others has also contributed to its growth.

In space, much of the solid material found is in the form of small grains, which play an essential role in star formation, as observed in Eagle Nebula (Fig. 1.4). Comets often exhibit separate ion and dust streams in their tails. In Fig.1.5, the two visible tails of Hale-Bopp are the results of the light pressure induced by photons emitted from the sun. Since dust particles have heavier masses as compared to the ions, they are barely influenced by this light pressure and separate from the ions.

Dust in planetary rings is also of great interest. The optical depth modulation seen in Saturn’s *B* ring, called “*spokes*”, is believed to be composed of electrostatically levitated micron and submicron-sized dust grains (Smith *et al* 1981). The rings of Saturn were first observed by the Voyager spacecraft (Smith *et al* 1981; 1982), and later by

Hubble Space Telescope (McGhee *et al* 2005) and the Cassini spacecraft (Mitchell *et al* 2006) (see Fig. 1.6). Ring particles are composed primarily of water ice, with some contamination from dust and other chemicals, and range from microns to meters in size. They can appear either dark or bright depending on the light scattering direction.



FIG. 1.5. A view of comet Hale-Bopp showing two distinct tails, namely a thin blue plasma tail and a broad white dust tail. (Wurden *et al* 1999; Shukla, Mamun 2002 and courtesy of Dr. G Wurden, LANL, Los Alamos.)

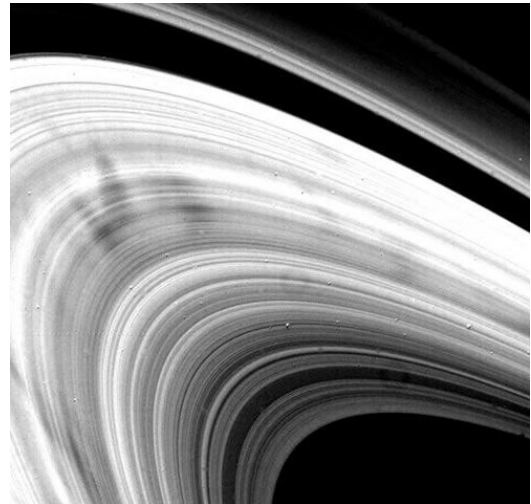


FIG. 1.6. A view of the nearly radial spokes in Saturn's B ring. (Courtesy of Jet Propulsion Laboratory.)

In semiconductor manufacturing, dust can become a critical issue in the plasma production of microelectronics. The contamination of a processing plasma by even very small particles ($\sim\mu\text{m}$) can render an entire semiconductor wafer useless. Such dust particles can cause voids and dislocations (Fig. 1.7) when they fall onto the wafer, causing a reduction in product viability and efficiency (Selwyn *et al* 1990). This has become much more important as the size of microchips produced continues to decrease since dust “killer” particles become smaller and harder to control (Fig. 1.8). The difficulty of dealing with such contamination effects is enhanced due to the variety of

sources contributing to creation of the dust. For example, when high velocity electrons/ions hit the wafer or reactor walls, they can cause sparks which sputter the material into the plasma where it becomes “dust.” Worse, the discharge gas itself can coagulate, growing large enough to produce “dust” from the atoms themselves (Bouchoule 1999).

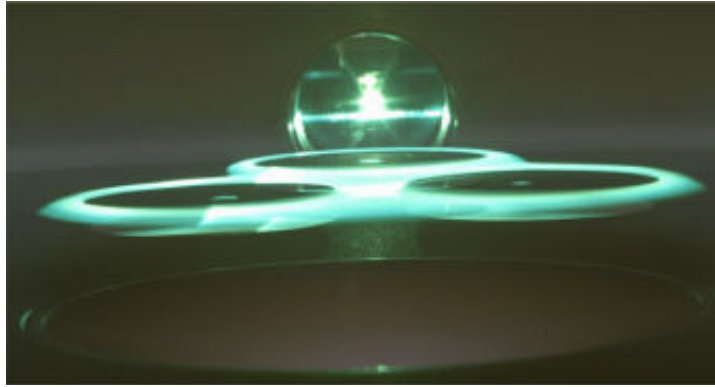


FIG. 1.7. Rings formed by dust particles suspended above silicon wafers (Selwyn *et al* 1990).

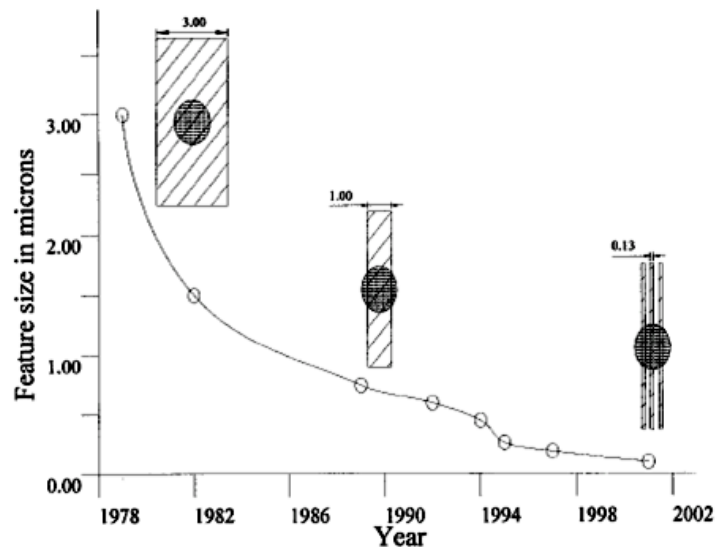


FIG. 1.8. As chip feature size decreases, a $1.5\ \mu\text{m}$ particle becomes a “killer” particle. (Courtesy of Intel.)

Many positive aspects of dusty plasmas have also been discovered and investigated. For instance, the performance of solar panels can be substantially improved by incorporating nanometer-size particles into silicon films (Roca *et al* 1996), and deposition rates can be increased by introducing dust into the plasma-enhanced chemical vapor deposition process (Boufendi and Bouchoule 2002).

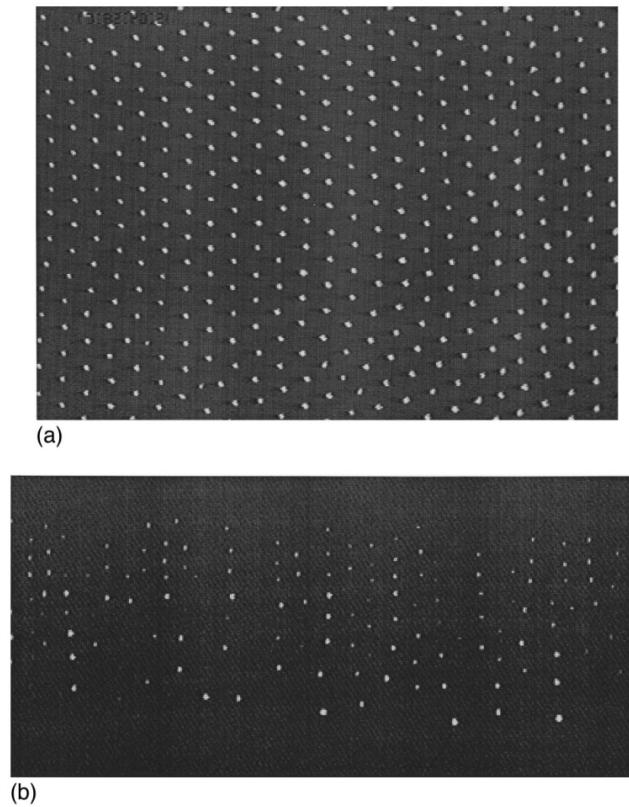


FIG. 1.9. (a) CCD image of a horizontal lattice plane of a plasma crystal. (b) A vertical slice through the crystal (Morfill and Thomas H 1996).

Since dust particles can be manually injected into a laboratory plasma and then illuminated by lasers, dusty plasma is now providing insight into fundamental research across multiple disciplines. In an ordinary plasma, ions and electrons can be created by ionization and annihilation through neutralization, making the plasma an open system. Due to the absorption and emission of electrons and ions on the surface of the dust, dust

particles can act as new sinks or sources in the plasma, resulting in a three component plasma system which is even more open. Under the proper boundary conditions, dust particles can form both horizontal crystalline planes and vertical chain structures, providing a unique opportunity to study such systems on the kinetic level (FIG. 1.9) (Morfill and Thomas H 1996). In microgravity, for example on the space station, dust particles can form voids due to the balance between the electric and ion drag forces (FIG. 1.10) (Thomas H *et al* 2005). Particles suspended in the plasma sheath can also be used as in-situ diagnostics, allowing direct determination of the sheath profile within a laboratory plasma (Konopka *et al* 2000).

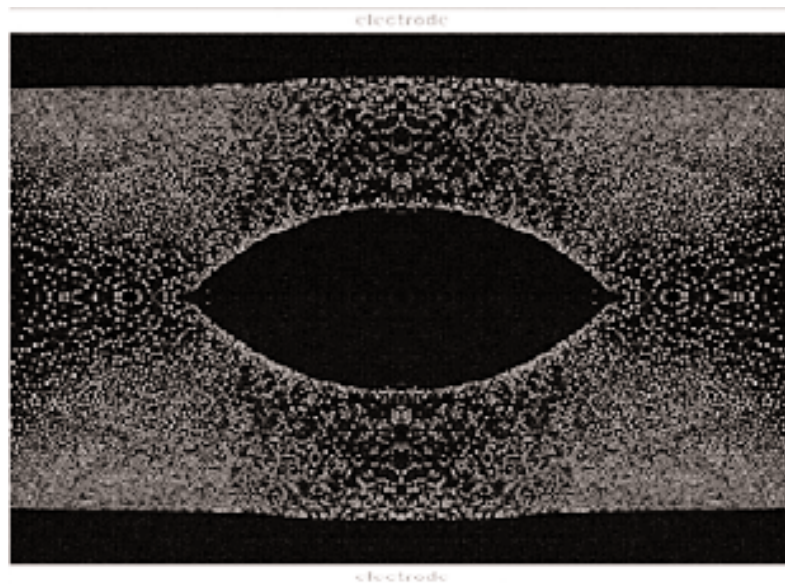


FIG. 1.10. Under microgravity, the dust particles disperse throughout the experimental volume, forming a void in a large 3-dimensional complex plasma (Thomas H *et al* 2005).

1.3. Structure of the Dissertation

This work investigates fundamental particle interactions and wave propagation in dusty plasmas, both experimentally and theoretically. The experiments presented were performed in a modified Gaseous Electronic Conference (GEC) radio- frequency (RF)

reference cell in the Hypervelocity Impacts & Dusty Plasma Lab (HIDPL) at the Center for Astrophysics, Space Physics and Engineering Research (CASPER) located at Baylor University.

In Chapter Two, a brief explanation of the dusty plasma knowledge needed for understanding the investigations provided in this dissertation is presented. Specific attention will be focused on particle charging mechanisms, the forces on particles and wave propagation.

In Chapter Three, the CASPER GEC RF reference cell setup where the experiments were conducted will be introduced. In particular, the two main confinement configurations employed, circular milled cutout plates and glass boxes, will be described. Each rests on the lower powered electrode and contributes to the confinement of the particles. As such, they each also contribute to the experimental phenomenon observed in the system.

In Chapter Four, the experimental investigation into particle interactions within the plasma sheath will be presented. A simple non-perturbative single particle approach will be introduced employing an uncertainty reduction technique based on the trajectory of the two particles interacting in the plasma system.

In Chapter Five, an additional experimental investigation of particle dynamics in a glass box within a dusty plasma will be discussed. Properties, such as the resonance frequencies, oscillation amplitudes, phase difference, etc., are investigated for a single vertical chain. The wave frequencies and wave numbers for self-excited dust acoustic waves will be also presented.

In Chapter Six, a theoretical calculation of the dispersion relationship for a dust acoustic wave in a dusty plasma will be presented, employing an ion-dust two stream instability fluid model and taking into account the effects of charge variation, ion-drag-force fluctuation and dust temperature. A brief description of the ion-dust two stream instability fluid model will be introduced and detailed calculations of a comprehensive dispersion relation for dust acoustic waves will be presented.

Finally, in Chapter Seven, a brief summary of the work discussed previously and a discussion of possible future work will be given.

CHAPTER TWO

Basic Theory of Dusty Plasma

2.1. Introduction

Plasma crystals were discovered in capacitively coupled RF discharges almost simultaneously in several laboratories in the early 1990's (Chu 1994; Thomas H *et al* 1994; Hayashi, Tachibana 1994; Melzer *et al* 1994). Since then, great interest in dusty plasma research has erupted. In this chapter, a brief description of the fundamental theory behind dusty plasma is given in order to provide the basic knowledge necessary for a prior understanding of the experimental and theoretical investigations provided in this dissertation. In Section 2.2, the two main types of dusty plasmas are briefly described. A basic theory of the plasma sheath is introduced in Section 2.3 and several particle charging mechanisms and their limitations are discussed in Section 2.4. Section 2.5 illustrates the common forces acting on the charged particles. Finally, one of the main collective behaviors seen in dusty plasma, waves, is discussed in Section 2.6.

2.2. Dusty Plasmas in the Laboratory

There are two primary types of discharge plasmas: DC and RF. RF plasma can be produced in either a capacitively coupled or inductively coupled manner. In this section, a typical laboratory experimental setup for a DC discharge and a capacitively coupled RF discharge is described. The majority of the dusty plasma phenomenon examined in this work occurs in one of these two discharges.

2.2.1. DC Discharge Plasma

DC discharges are extensively used for experimental investigation of dusty plasmas. Typically, discharge gas pressures are in the range of 10 – 1000 mTorr and the discharge current is ~ 0.1 -10 mA (Fortov *et al* 2005). A sketch of a typical DC discharge experimental setup for laboratory dusty plasma research is shown in Fig. 2.1 (Fortov *et al* 1997). Free electrons are accelerated away from the cathode by the electric field created between the two electrodes, and gain energy. During their travel, they collide with and ionize back ground neutral atoms, resulting in more charged particles. While the resulting electrons are accelerated and collide with more neutral atoms, the positive ions are accelerated to hit the cathode, emitting electrons through the secondary electron emission process. Thus, a self-sustained discharge is created. In a DC discharge, the dust particles introduced into the discharge region are located in the bulk plasma.

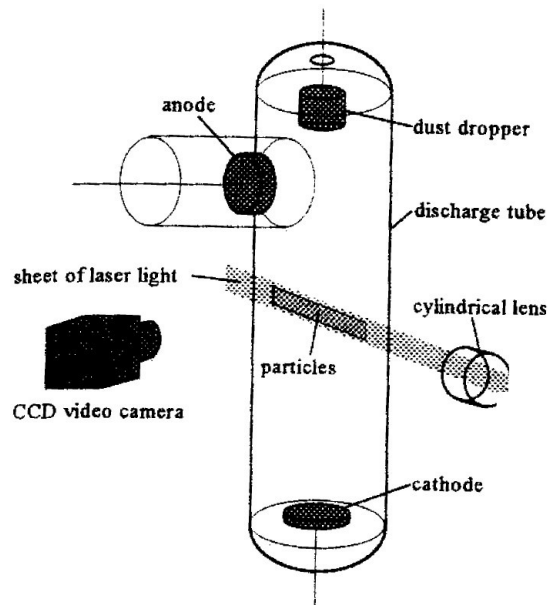


FIG. 2.1. Sketch of a typical DC discharge experimental setup for laboratory dusty plasma research (Fortov *et al* 1997).

2.2.2. *Capacitively Coupled RF Discharge*

Plasma crystals were first observed in capacitively coupled low-pressure RF discharges. A schematic of a typical capacitively coupled RF discharge experimental setup is shown in Fig. 2.2 (Thomas H *et al* 1994), analogous to the one used in the CASPER lab where the experiments presented in this dissertation were conducted. The top electrode and the chamber walls are grounded while the bottom electrode is powered by an RF generator with a frequency set to be 13.56 MHz. A description of the system setup within the CASPER lab will be given in Chapter Three.

When an electric field is applied to the lower electrode, neutral atoms are excited, becoming ionized through collisions with accelerated free electrons, and an RF discharge plasma is generated. When the kinetic energy of electrons and ions is comparable, the velocity of electrons is much higher than that of the ions. The free electrons are able to follow the high frequency signal provided by the RF power supply, due to their higher mobility, and are accelerated by the electric field to collide with neutral atoms, while the resulting ions with their lower mobility only feel the effective electric and are not accelerated by the alternating electric field. This means that most of the excitation and ionization involved within the RF plasma is created by collisions between high speed electrons and neutral atoms, while the secondary electron emission caused by ion collision with the electrodes is minor.

When the applied discharge power is strong enough, a small number of free electrons are subject to acceleration by the electric field, colliding and ionizing the atoms in the gaseous medium, thereby forming new electrons to undergo the same process in successive cycles, this is called “*electron avalanche*” (Sparks 1975). As soon as the

electron avalanche is triggered, the gas becomes electrically conductive due to abundant free electrons. A plasma is always accompanied by light emission observable even with the naked eye.

Different from what is found in a DC discharge, in a laboratory RF dusty plasma, dust particles are located in the dark region above the powered electrode. This region is known as the plasma “*sheath*.”

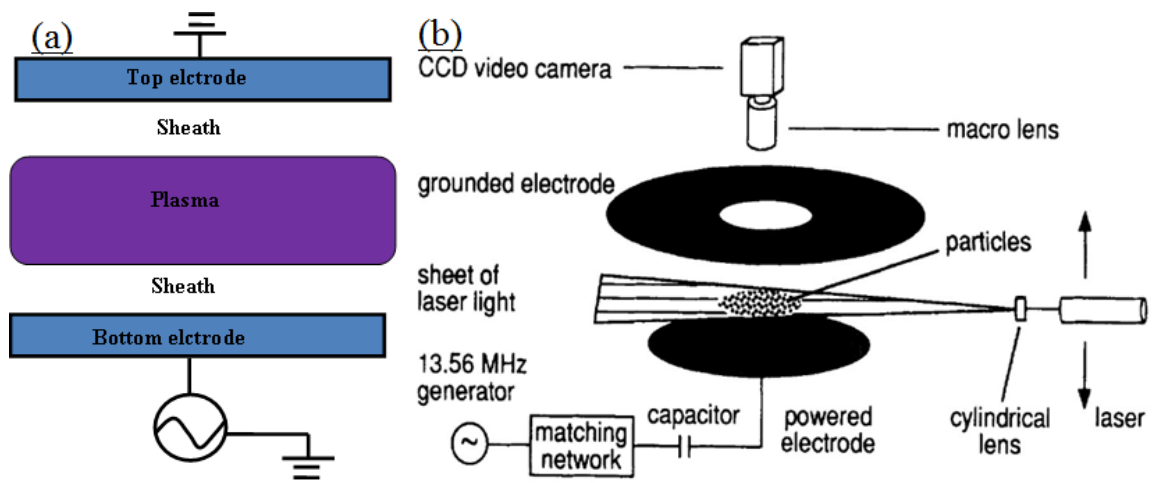


FIG. 2.2. (a) Schematic of a typical capacitively coupled RF discharge and (b) a typical experimental setup for laboratory RF dusty plasma research (Thomas H *et al* 1994). Details of the setup used in this work will be discussed in Chapter Three.

2.3. Debye Shielding (Screening Length)

It is well known that one of the most important properties of a plasma is its ability to shield the electric field of an individual particle or particles inside. The distance characterizing the influence of the electric field produced by an individual charged particle on another charged particle inside a plasma is defined as “the Debye shielding.” The Debye shielding in an ordinary ion-electron plasma has been well described in standard textbooks (Chen 1984). The Debye shielding in a dusty plasma will be briefly discussed below.

Assuming a dust particle is inserted into a dusty plasma composed of ions, electrons, neutral atoms and dust particles, the dust particle will become charged (see section 2.5) and then surrounded by plasma particles of the opposite charge. In the region close to the dust particle surface, the electrostatic potential can be described by the Poisson equation:

$$\nabla^2 \phi(r) = -\frac{\rho}{\epsilon_0}, \quad (2.1)$$

where $\rho = n_i e + q_d n_d - n_e e$ is the local charge density, and q_d and n_d are the dust particle charge and number density respectively. If it is assumed that the electrons and ions obey the Boltzmann distribution,

$$n_e = n_{e0} \exp\left(\frac{e\phi}{k_B T_e}\right), \quad (2.2)$$

$$n_i = n_{i0} \exp\left(\frac{e\phi}{k_B T_i}\right), \quad (2.3)$$

where n_{e0} and n_{i0} are the unperturbed electron and ion number density, respectively, the quasi-neutrality condition gives $q_d n_d = n_{e0} e - n_{i0} e$. Substituting equations (2.2) and (2.3) into (2.1) and assuming $e\phi \ll k_B T_e, k_B T_i$, the Poisson equation evolves to be:

$$\nabla^2 \phi = \left(\frac{1}{\lambda_{De}^2} + \frac{1}{\lambda_{Di}^2} \right) \phi, \quad (2.4)$$

where $\lambda_{De,Di} = (k_B T_{e,i} / 4\pi n_{e,i} e^2)^{1/2}$ is the electron/ion Debye length. Assuming

$\phi = \phi_0 \exp(-r / \lambda_D)$, the Debye length can now be obtained from Eq. (2.4) and expressed by:

$$\lambda_D = \left(\lambda_{De}^{-2} + \lambda_{Di}^{-2} \right)^{-1/2}. \quad (2.5)$$

2.4. RF Plasma Sheath

The plasma region located near a device boundary is known as the “*sheath*.” The properties of the sheath for an ordinary two component electron-ion plasma is well discussed in standard textbooks (Chen 1984). Even so, the sheath profile bears additional examination since it needs to be well understood given that dust particles are usually suspended in the sheath in a laboratory RF dusty plasma.

2.4.1. RF Sheath Formation

In order to describe the formation of a sheath in an RF plasma, a planar electrode with a floating potential is assumed to be in contact with a non-isothermal plasma having equal ion and electron densities, $n_{i,e}$. Due to the higher mobility of the electrons, the electron flux to the plate’s surface is larger than the ion flux, resulting in negative charging of the plate. As a result, electrons are repelled from the plate while ions are attracted towards it. When the reduced electron flux becomes equal to the ion flux, the current to the plate electrode remains balanced at a negative potential. Thus, when compared to the bulk plasma, a positive space charge region is created immediately in front of the plate electrode ($n_i > n_e$), called the plasma “*sheath*.” This region appears optically dark due to the lack of excitation of neutral atoms.

2.4.2. Electric Field

The potential difference between the bulk plasma and the electrodes creates an electric field within the sheath. Assuming a time averaged electric field, only dependent on distance to the electrode, z , Poisson’s equation becomes

$$\frac{dE(z)}{dz} = \frac{\rho(z)}{\epsilon_0} = \frac{e}{\epsilon_0}(n_i(z) - n_e(z)), \quad (2.6)$$

where ϵ_0 is the vacuum permittivity. Neglecting electrons and assuming a constant ion density, the electric field can be determined through integration of Eq. (2.6) (Melzer *et al* 1994):

$$E(z) = \frac{en_i}{\epsilon_0}(z - z_s). \quad (2.7)$$

In Eq. (2.7), z_s is the sheath edge where the electric field is assumed to be zero. Until recently, the electric field in the RF sheath has been widely assumed to be linear in nature in experiments (Homann *et al* 1998; Schollmeyer *et al* 1999). Both numerical models (Tomme *et al* 2000) and experimental measurements (Zafiu *et al* 2001; Samarian, James, 2001, 2005) showed the validity of this assumption. However, recent work has determined that the electric field is in fact not linear throughout the entire sheath (Douglass *et al* 2011). In the experiments presented, the particles are located in the approximately linear electric field region. Thus, the nonlinear effect is not considered here. In the sheath, the magnitude of the electric field is found to be on the order of $10^2 - 10^4$ V/m with the thickness of the sheath extending to several Debye lengths.

2.4.3. Bohm Criterion

To determine the exact position of the particles in the sheath, it is first necessary to define the sheath edge. There are several arguments as to this definition (Riemann 1991, 1997; Samarian, James 2001; Pandey, Dutta 2005). One commonly used definition employs is the *Bohm criterion*, which is the position where the ion drift velocity becomes greater than the *Bohm velocity*. Here, a very simple deduction of the Bohm criterion is

introduced under several assumptions (Bohm 1949; Riemann 1991): a) collisionless sheath, b) quasi-neutrality at the sheath edge $n_i = n_e = n_s$, c) a Maxwellian distribution of electrons, $n_e(x) = n_s \exp[eV(x)/kT_e]$, and d) cold ions, $T_i = 0$ K.

Considering no collisions or ionizations, the energy conservation and flux continuity equations for the ions can be expressed as:

$$\frac{1}{2} m_i u^2(x) = \frac{1}{2} m_i u_s^2 - eV(x), \quad (2.8)$$

$$n_i(x)u(x) = n_s u_s. \quad (2.9)$$

Here, $u(x)$ and u_s are the ion drift velocity in the sheath and its value at the sheath edge, respectively. $V(x)$ is the local electrostatic potential. The ion density in the sheath can be solved employing Eqs. (2.8) and (2.9):

$$n_i(x) = n_s \left[1 - \frac{2eV(x)}{m_i u_s^2} \right]^{-1/2}. \quad (2.10)$$

Thus, the Poisson's equation becomes:

$$\frac{d^2 V(x)}{dx^2} = \frac{e}{\epsilon_0} (n_e - n_i) = \frac{en_s}{\epsilon_0} \left[\exp\left(\frac{eV}{kT_e}\right) - \left(1 - \frac{2eV}{m_i u_s^2}\right)^{-1/2} \right]. \quad (2.11)$$

Equation (2.11) has a real solution only if (Bouchoule 1999)

$$u_s \geq v_B = \sqrt{kT_e/m_i}. \quad (2.12)$$

This inequality is called the *Bohm criterion* and v_B is called the *Bohm velocity*. The Bohm criterion implies a minimum velocity for ions entering the plasma sheath.

2.5. Particle Charging Models

The dust particle charge is one of the most important parameters in a dusty plasma. Almost every analysis in dusty plasmas necessarily starts with the charge on the particle

since this determines the particle's interaction with its neighbors, the local electric field, the plasma background, etc. The dust particles are charged by the collection of the plasma particles flowing onto their surfaces. Other charging mechanisms such as secondary electron emission, photoemission, thermionic emission, radioactivity, etc., will not be discussed since they are not needed in this dissertation. In this section, an overview of several commonly used particle charging models is given, and their limitations are discussed.

2.5.1. Orbital Motion Limited (OML) Approximation

Deduction of the OML approximation equations. Dust particles immersed in a plasma will become negatively charged in the absence of strong electron emission. This is because the electrons have higher mobility resulting in an initial flux exceeding that of the ions to the particle surface. The resulting negatively charged dust particle will repel electrons and attract ions due to Coulomb forces. The final balance between the electron and ion fluxes leads to an equilibrium charge on the dust particle. One of the most commonly used approaches to describe the electron and ion fluxes to the dust particle surface is the *Orbital Motion Limited* (OML) approximation (Allen 1992). Considered as a simple model, the OML approach is employed under three major assumptions: a) the dust particle is isolated and does not interact with other particles in its vicinity, b) the plasma is collisionless implying electrons and ions approach the dust particle without collisions, and c) the effective potential has no boundary (Fortov *et al* 2005).

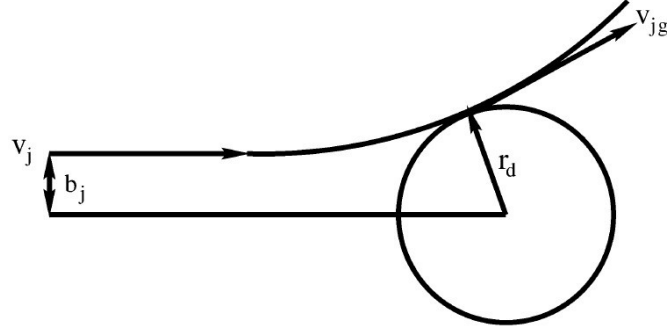


FIG. 2.3. Grazing collisions between a plasma particle j and a charged dust particle with $q_j q_d < 0$ (Shukla, Mamun 2002).

First, a calculation of the charging flux I_j carried by the plasma particle j to the dust particle surface is required. Considering the case of a plasma particle j coming from infinity with a velocity v_j and charge q_j , approaching to the dust particle having radius a and charge q_d , the interaction between them occurs due to the electrostatic force when they come within the impact parameter (see Fig. 2.3). Assuming an impact parameter b_j for a grazing collision, the cross section for a charging collision between the dust particle and plasma particle j can be expressed as $\sigma_j^d = \pi b_j^2$. The conservation laws for momentum and energy give:

$$m_j v_j b_j = m_j v_{gj} a \quad (2.13)$$

and

$$\frac{1}{2} m_j v_j^2 = \frac{1}{2} m_j v_{gj}^2 + \frac{q_j q_d}{4\pi\epsilon_0 a}, \quad (2.14)$$

where v_{gj} is the velocity of plasma particle j after the grazing collision. The particle charge can be related to the particle surface potential through $q_d = 4\pi a \epsilon_0 \phi_s = -Z_d e$. This relation remains valid for particle radii much smaller than the Debye length (Barge 1998);

thus, the velocity dependent plasma particle-dust cross section as determined by Eqs.

(2.13) and (2.14) can be expressed by

$$\sigma_j(v_j) = \pi a^2 \left(1 - \frac{2q_j\phi_s}{m_j v_j^2}\right). \quad (2.15)$$

For an ordinary ion and electron plasma, $j = i, e$, $q_j = \mp e$, and these electron- and ion-dust cross sections are

$$\sigma_e(v) = \pi a^2 \left(1 + \frac{2e\phi_s}{m_e v_e^2}\right), \quad (2.16)$$

$$\sigma_i(v) = \pi a^2 \left(1 - \frac{2e\phi_s}{m_i v_i^2}\right). \quad (2.17)$$

Here, $m_{e,i}$ is the electron/ion mass and $v_{e,i}$ is the velocity relative to the dust particle potential.

Given a velocity distribution function $f_j(v_j)$ for plasma particle j at an infinite distance from the dust particle, the charge flux to the dust surface I_j can be obtained by:

$$I_j = \int_{v_j^{\min}}^{\infty} v_j \sigma_j(v_j) f_j(v_j) d^3 v_j, \quad (2.18)$$

where v_j^{\min} is the minimum velocity of the plasma particle j required to reach the dust particle surface. Two different cases must be treated separately in order to obtain the minimum velocity: $q_j\phi_s < 0$ and $q_j\phi_s > 0$. For $q_j\phi_s < 0$, the interaction between the plasma particle j and the dust particle is attractive; thus, the value of v_j^{\min} is the minimum value for the possible velocity of the plasma particle j (for a Maxwellian distribution, this is zero). On the other hand, when $q_j\phi_s > 0$, the interaction between plasma particle j and the dust particle is repulsive; thus $v_j^{\min} > 0$ is required. This value can be calculated employing energy conservation and expressed as:

$$v_j^{\min} = \left(-\frac{2q_j\phi_s}{m_j}\right)^{1/2}, \quad (2.19)$$

assuming the velocities of plasma particle j can be described by a Maxwellian distribution

$$f_j(v_j) = \frac{1}{(\sqrt{2\pi})^3 v_{T_j}^3} \exp\left(-\frac{v_j^2}{2v_{T_j}^2}\right), \quad (2.20)$$

where $v_{T_j} = \sqrt{k_B T_j / m_j}$ is the plasma particle thermal velocity, and T_j and k_B are the plasma particle temperature and the Boltzmann constant. Substituting Eqs. (2.15), (2.20) and (2.19) into (2.18), and assuming an ordinary ion-electron plasma, by expanding the integration (2.18), the flux of ions and electrons to the dust particle surface can be expressed respectively as

$$I_e = \sqrt{8\pi} a^2 n_e v_{T_e} \exp(-z) \quad (2.21)$$

$$I_i = \sqrt{8\pi} a^2 n_i v_{T_i} (1 + z\tau) \quad (2.22)$$

In equations (2.21) and (2.22), two dimensionless parameters are used,

$$z = \frac{Ze^2}{4\pi\epsilon_0 a T_e}, \text{ and } \tau = T_e / T_i, \quad (2.23)$$

where z is the *dimensionless charge number* and τ is the electron-to-ion temperature ratio.

The charging evolution is found by equating the change in charge to the net current:

$$-\frac{dZ}{dt} = I_i - I_e. \quad (2.24)$$

Thus, the stationary charge can be determined when the time variation becomes zero,

$I_i = I_e$, which yields

$$\exp(-z) = (1 + z\tau) \frac{n_i v_{Ti}}{n_e v_{Te}}. \quad (2.25)$$

When the particle density is small in the bulk of the plasma, quasi-neutrality $n_i \approx n_e$

allows Eq. (2.25) to be simplified to:

$$\sqrt{\tau} \exp(-z) = (1 + z\tau) \sqrt{m_e/m_i}. \quad (2.26)$$

From the above, it can easily be seen that, in the OML approximation, the particle charge depends on two ratios: the electron-to-ion temperature ratio and the electron-to-ion mass ratio. Figure 2.4 shows the dimensionless charge number dependency on the electron-to-ion temperature ratio for various noble gases. As shown in the figure, z decreases with increasing τ but increases with the atomic mass of the gas.

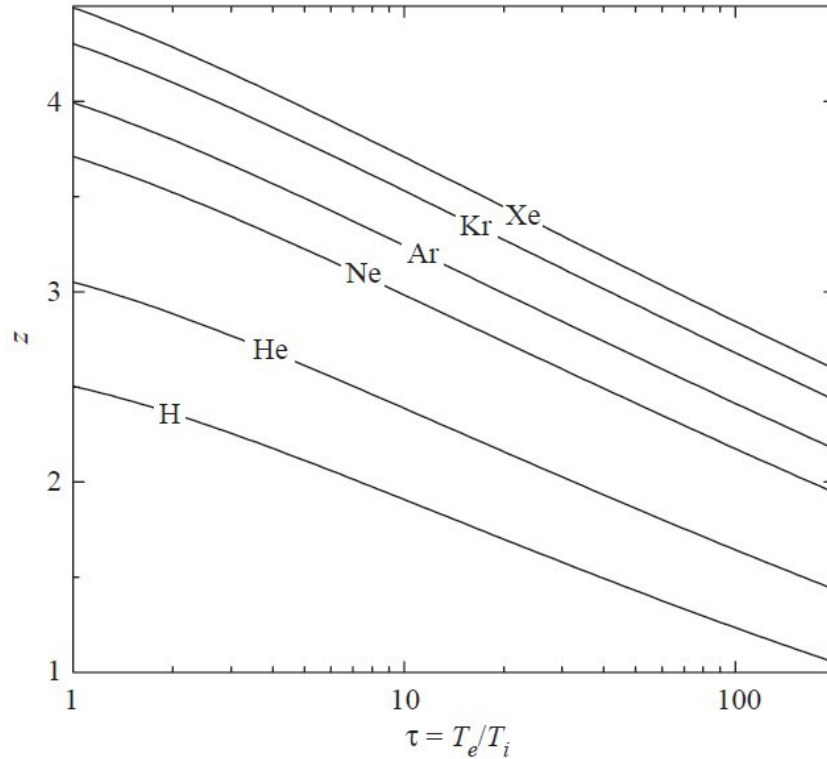


FIG. 2.4. Dimensionless charge number of an isolated spherical particle as a function of the electron-to-ion temperature ratio for isotropic plasmas of different gases (Fortov *et al* 2005).

Accuracy of the OML approximation. The OML approximation provides a simple and fast approach to estimation of the dust particle charge; as such, it is widely used in dusty plasma research. However, in reality, the assumptions underlying the OML model are rarely satisfied. As a result, large deviations from the particle charge obtained by OML can occur when these assumptions are invalid. Three representative examples are given below.

Firstly, the isolated particle assumption will be quickly broken for large particle numbers such as those found in dust crystals, producing what is known as the “closely packed” effect. When the inter-particle spacing is smaller than the plasma Debye length ($\Delta < \lambda_D$), the trajectories of the electrons and ions around a charged particle will be affected by its neighbors, resulting in a change in the overall particle equilibrium charge. At the same time, the net charge on the particles plays an important role in the overall plasma quasi-neutrality due to the large numbers of charged dust particles: $n_i = n_e + n_d Z_d$. Defining the ratio of the charge density on the dust particles to the charge density on the electrons (the “Havnes parameter”) $P = n_d Z_d / n_e$ (Havnes 1990), the quasi-neutrality equation becomes $n_i / n_e = 1 + P$. Thus, equation (2.25) becomes:

$$\sqrt{\tau} \exp(-z) = (1 + z\tau)(1 + P)\sqrt{m_e/m_i} \quad (2.27)$$

It can easily be seen from the above that a significant change will take place when $P \gg 1$. This “closely packed” effect has been proven in experiments where a significant reduction in particle charge was observed under such conditions (Barken *et al* 1994).

Secondly, the collisions occurring between the ions and the neutral atoms during the ions approach to the dust particle surface can result in an overall reduction in charge (Ratynskaia *et al* 2004). These collisions take place when the ion mean free path ℓ_i is

larger than the plasma Debye length λ_D (Lampe *et al* 2001, 2003). A substantial increase in the ion flux to the particle's surface can occur due to ion-neutral charge-exchange collisions, resulting in a decrease in particle charge. Details of this ion-neutral collision effect will be discussed in section 2.4.3.

Finally, the absence of effective potential energy barriers can be invalid when the interaction is attractive (i.e., for the ions). Low energy ions are reflected during their approach to the particle surface by a potential barrier. Thus, fewer ions are collected by the particles, leading to a more negative particle charge (Allen *et al* 2000). It has been shown that the electrostatic potential around a small absorbing grain in a plasma scales as r^{-1} close to the grain, r^{-2} far from it. Thus, low energy ions moving towards the grain encounter a potential barrier around the grain and will be reflected. For a Maxwellian velocity distribution of ions, there are always ions with sufficiently low energy to be reflected from the potential barrier. If the fraction of these low energy ions is small, the deviation of the results from those obtained using OML theory is also small. In the other case, if this fraction is considerable, a correction to OML is required. For a Yukawa potential ($\phi \sim (1/r)\exp(-r/\lambda)$), the criterion for the OML application is theoretically predicted as (Khrapak *et al* 2004):

$$\sqrt{2\tau z}(a/\lambda) \leq \ln[z\tau(a/\lambda)]. \quad (2.28)$$

For typical laboratory dusty plasma parameters with $z \sim 1$, $\tau \sim 100$, this condition is $a/\lambda \leq 0.2$.

2.5.2. Charging in Anisotropic Plasmas (DML approximation)

Deduction of DML approximation. As discussed in Section 2.3, dust particles are usually suspended in the sheath where a strong electric field exists in a laboratory RF discharge plasma. This electric field accelerates both electrons and ions, resulting in drift flow velocities relative to the dust particles, modifying collision cross sections, and making the global charging process much more complicated. In this case, the velocity distributions become Maxwellian distributions with shifted average velocities:

$$f_{e,i}(\vec{v}) = (2\pi v_{T_{e,i}}^2)^{-3/2} \exp\left[\frac{(\vec{v} - \vec{u}_{e,i})^2}{2v_{T_{e,i}}^2}\right] \quad (2.29)$$

where $\vec{u}_{e,i}$ is the electron/ion average drift velocity. To provide an analytical result, OML cross sections are employed here. Integrating the cross section using a shifted Maxwellian velocity distribution, the resulting ion and electron fluxes are:

$$I_i = \sqrt{\pi} \frac{a^2 n_i V_{T_i}^2}{u_i} \left[\sqrt{\pi} (1 + 2\xi^2 + 2z\tau) \operatorname{erf}(\xi) + 2\xi \exp(-\xi^2) \right], \quad (2.30)$$

and

$$I_e = \sqrt{\pi} \frac{a^2 n_e V_{T_e}^2}{u_e} \left\{ \sqrt{\pi} (1/2 - \xi_+ \xi_-) [\operatorname{erf}(\xi_+) - \operatorname{erf}(\xi_-)] \right. \\ \left. + \xi_+ \exp(-\xi_-^2) - \xi_- \exp(-\xi_+^2) \right\}, \quad (2.31)$$

where $\xi = u_i / \sqrt{2} v_{T_i}$, $\xi_{\pm} = \sqrt{z} \pm u_e / \sqrt{2} v_{T_e}$, and $\operatorname{erf}(x) = 2\pi^{-1/2} \int_0^x e^{-t^2} dt$ is the error

function. In the small drift velocity limit $u_{e,i} \ll v_{T_{e,i}}$, expressions (2.30) and (2.31) revert

to (2.22) and (2.21), while in the strong drift velocity limit, they become

$$I_i = \pi a^2 n_i u_i \left[1 + (1 + 2z\tau)(v_{T_i}/u_i)^2 \right], \quad (2.32)$$

$$I_e = \pi a^2 n_e u_e \left[1 + (1 - 2z\tau)(v_{T_e}/u_e)^2 \right]. \quad (2.33)$$

In most cases, electron drift is negligible while the ion drift is significant. By balancing the electron and ion flux to the surface of the particle, the particle's charge can be determined. The model employed here assumes a shifted Maxwellian velocity distribution and is called the *DML approximation*. Figure 2.5 shows the resulting dimensionless charge number as a function of the ion drift velocity at different ion-to-electron density ratios. The charge remains almost constant when $u_i \leq v_{Ti}$, then increases significantly with u_i , reaching a maximum value at $u_i \sim (2 - 4) C_{IA}$ ($C_{IA} = \sqrt{T_e/m_i}$ is the ion acoustic phase velocity) (Fortov *et al* 2005).

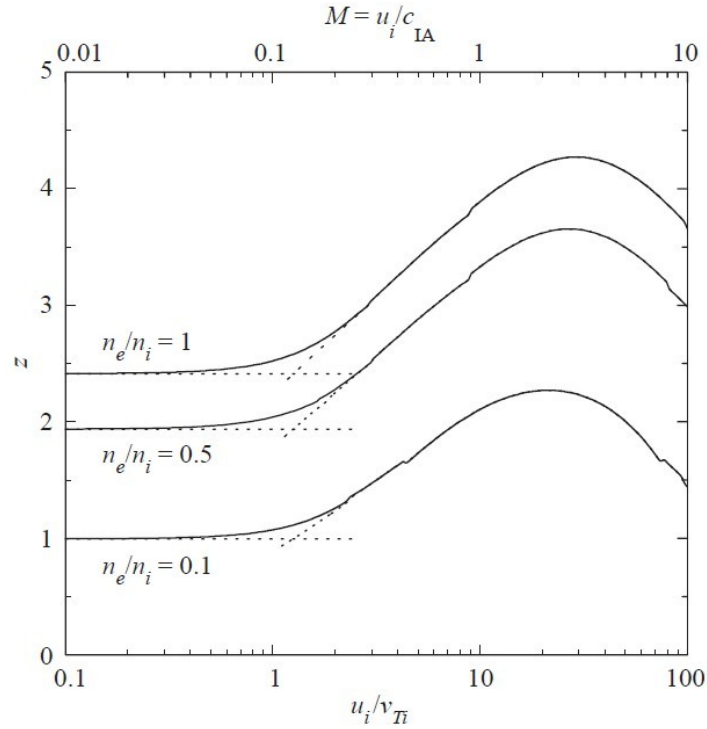


FIG. 2.5. Dimensionless charge number as a function of ion drift velocity or Mach cone number ($M = u_i/C_{IA}$) for an argon plasma with ion flow ($\tau = 100$). Dashed lines indicate the calculated results employing simplified ion current flux Eq. (2.32) (Fortov *et al* 2005).

Accuracy of the DML approximation. The assumption of an OML cross section implies an isotropic potential. However, under the effect of ion and electron flows like the ones described above, the potential becomes highly anisotropic. Through particle-in-cell codes (Lapenta 1999; Hutchinson 2003, 2005), it has been shown that the agreement between theory and simulation is weak, particularly for a dielectric particle with a significant dipole moment. In a strong supersonic plasma flow, the electrostatic potential around a dielectric particle is strongly anisotropic due to significant inhomogeneity of the surface charge, while the potential around a conductive particle is spherically symmetric. The dielectric potential includes two parts: one describes the spherically symmetric charge potential while the other corresponds to the anisotropic dipole potential. The presence of a dipole moment on a dielectric particle contributes to a significant increase in its charge compared to a conductive particle (Ivlev *et al* 1999). Figure 2.6 shows the difference between the charge on a dielectric particle and a conductive particle.

2.5.3. *Charging in Weakly Collisional Plasmas*

In Section 2.4.1, it was mentioned that ion-neutral collisions can significantly suppress particle charging. The details behind this effect and the corresponding modifications they require to OML theory will now be discussed.

Ion-neutral collisions can result in two effects: momentum exchange and charge exchange. Ions can transfer their momentum to neutral atoms during ion-neutral collisions, slowing and allowing them to become trapped in highly negative potentials, i.e., the region close to negatively charged dust particles. The slowest of these ions cannot escape this confinement potential and finally are captured by the charged particles. As a consequence, the ion flux to the dust particle's surface is enhanced and more

electrons residing on it are neutralized by the enhanced ions. Thus, a decrease in particle charge occurs. This is most effective when combined with the charge-exchange effect. In this case, the high velocity ions collide with lower energy neutral atoms, transferring their charge. Low energy neutral atoms substitute for higher velocity ions, leading to more ions being trapped and finally collected by the particle's negative potential. At the same time, high gas pressure enhances the ion-neutral collision probability resulting in decreasing the ion mobility. Thus, the ion-neutral collisions eventually decrease the particle's charge.

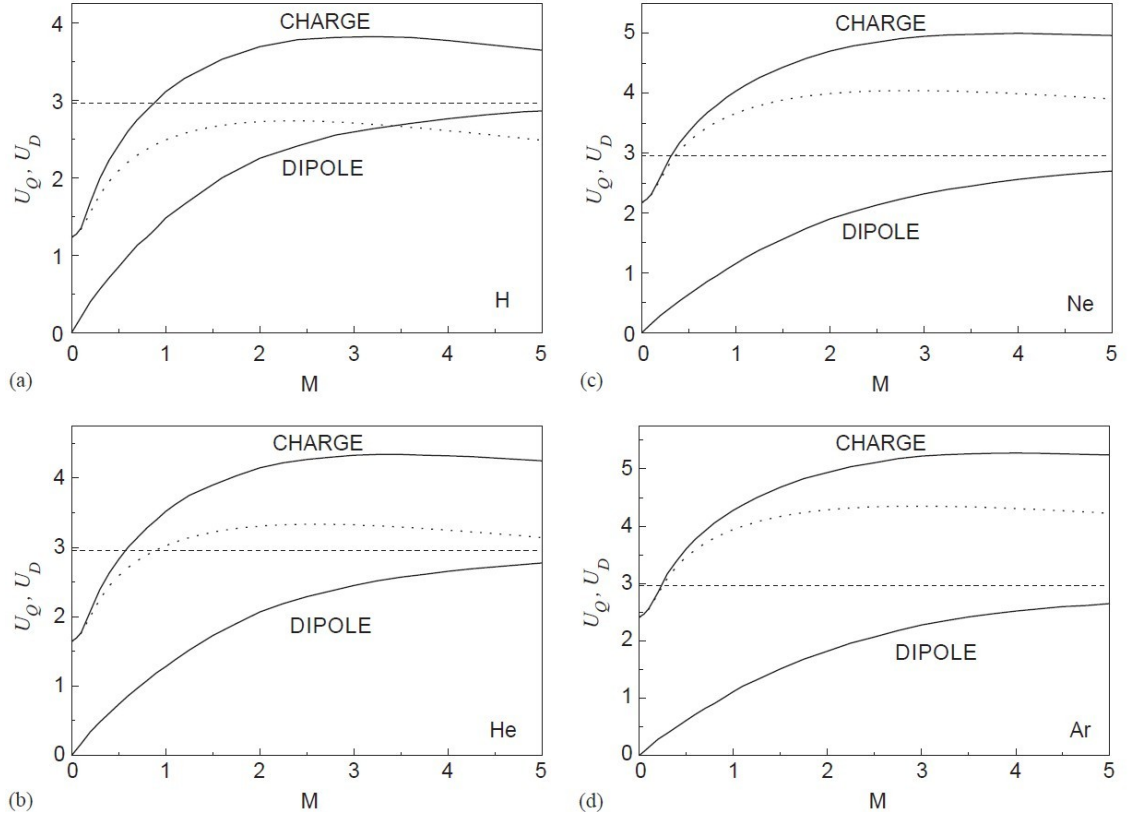


FIG. 2.6. The dimensionless charge, $U_Q = e^2 Z / a T_e$ (same as z in this dissertation), and the dimensionless dipole moment, $U_D = ed / a^2 T_e$ as functions of Mach cone number in a plasma with ion flow. Solid lines denote a dielectric particle while the dotted line corresponds to a metal particle. The dashed line is the asymptote for the dipole curve. The figures are for plasmas with (a) H, (b) He, (c) Ne, and (d) Ar (Ivlev *et al* 1999).

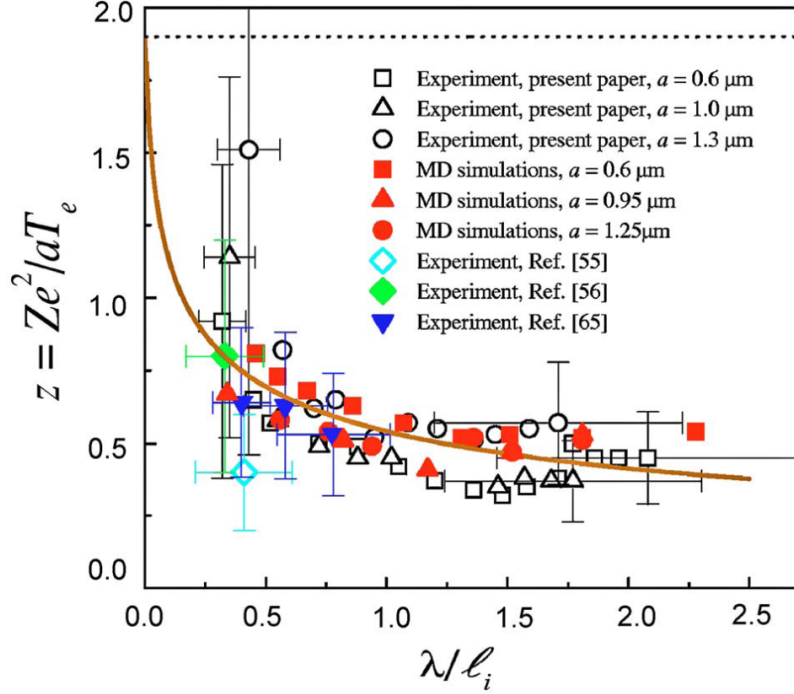


FIG. 2.7. Dimensionless charge number z as a function of the ion collisionality parameter λ/l_i (assuming $\lambda \approx \lambda_D$). The open symbols denote the charges measured for particle radii $a = 0.6 \mu\text{m}$ (squares), $1 \mu\text{m}$ (triangles), $1.3 \mu\text{m}$ (circles). The solid squares, triangles, circles correspond to the charges from MD simulation for particle radii $a = 0.6 \mu\text{m}$ (squares), $0.95 \mu\text{m}$ (triangles), $1.25 \mu\text{m}$ (circles). Open and solid diamonds correspond to the experimental results reported by Khrapak (Khrapak *et al* 2003a) and Yaroshenko (Yaroshenko *et al* 2004). Solid down triangles denote the charges obtained by Fortov (Fortov *et al* 2004a) (The Ref. [55][56][65] in the figure correspond to Khrapak *et al* 2003, Yaroshenko *et al* 2004 and Fortov *et al* 2004a). The dotted line is calculated using the collisionless OML approach for an individual particle. The solid line shows a calculation using an analytical approximation of Eq. (2.34) for the ion flux to the particle in the weakly collisional regime for the ions. The neon plasma with $T_e = 7 \text{ eV}$ and $T_i = 0.03 \text{ eV}$ is used in these analytical calculations (Figure from Khrapak *et al* 2005).

For the weakly collisional regime, where the ion mean free path ℓ_i is larger than the plasma Debye length (Zobnin *et al* 1999), and assuming a Yukawa potential, the net ion flux to the particle can be characterized as (Lampe *et al* 2003; Khrapak *et al* 2005):

$$I_i = \sqrt{8\pi} a^2 n_i v_{Ti} \left[1 + z\tau + 0.1z^2\tau^2(\lambda/l_i) \right]. \quad (2.34)$$

The resulting dimensionless charge number z depends on τ and the “collisionality parameter (index)” λ/l_i (Lampe *et al* 2003). The collisionality parameter corresponds to

the contribution of ion-neutral collisions, becoming dominant when $l_i \leq 0.1 \ z\tau\lambda$ is satisfied.

Available experimental, analytical and numerical results are combined in Fig. 2.12 (Khrapak *et al* 2005). The effective plasma screening length $\lambda \approx \lambda_D \approx \lambda_{Di}$ is assumed for all conditions investigated. Reasonable agreement between the results from different experiments can be seen, even though they were conducted under different conditions. As shown in Fig. 2.7, the particle charge calculated under those conditions is much smaller than results obtained using collisionless OML theory. Additionally, predictions generated by (2.34) give a reasonable fit for the experimental and numerical results presented, taking into account experimental error ($\sim 30\%$). Remarkably, Fig. 2.7 demonstrates that in some situations, ion-neutral collisions can become the dominant effect in determining particle charging in an isotropic plasma.

2.6. Forces on a Single Particle

A proper understanding of the primary forces acting on a dust particle is necessary for determining the dynamic behaviors of the dusty plasma. In this section, the forces impacting the research in this dissertation are discussed: the gravitational, electric, neutral and ion drag forces. In a laboratory RF dusty plasma, every particle is subject to the gravitational force coming from the attraction of the earth. To levitate a charged dust particle in the sheath, an electric force associated with the sheath profile is necessary to compensate this force. At the same time, the relative velocity between the dust particles and the neutral molecules or ions creates a neutral or ion drag force which usually slows moving dust particles. Each of these will be discussed below in greater detail. Other

forces such as the radiation pressure force or the thermophoretic force are not needed for the research in this dissertation and are not considered.

2.6.1. Gravitational Force

Every particle in a laboratory dusty plasma generated on earth is subject to the gravitational force. This force is strongly related to both the composition of the particle and its radius:

$$\bar{F}_G = m_d \bar{g} = \frac{4}{3} \pi a^3 \rho_d \bar{g}, \quad (2.35)$$

where a and ρ_d are the radius and density of the particle, respectively. \bar{g} is the gravitational acceleration which always points to the center of mass of the earth, which in the CASPER GEC RF reference cell, makes the forces perpendicular to the bottom electrode.

2.6.2. Electric Force

As discussed previously, dust particles immersed in a laboratory RF plasma are negatively charged and levitate within the sheath. The electric force acting on these particles and creating this effect is the major force compensating the gravitational force and resulting in particle levitation in the sheath. This electric force was first analytically obtained by Daugherty *et al* (1993) as:

$$F_E = Q_d E_0 \left[1 + \frac{k_D^2 a_d^2}{3(1 + k_D a_d)} \right], \quad (2.36)$$

where Q_d and E_0 are the particle charge and the local electric field, both of which are functions of the distance to the bottom electrode. In Eq.(2.36), $k_D = 1/\lambda_D$ is the inverse of

the plasma Debye length; in most dusty plasmas, the condition $k_D a_d \ll 1$ is met. Thus, the electric force $F_E = Q_d E_0$ can be simply adopted.

2.6.3. Neutral Drag Force

The neutral drag force is defined as the rate of momentum exchange between dust particles and neutral atoms during collision. The relative motion between the dust particles and the neutral atoms can be interpreted in one of two ways: 1) the relatively static dust particles receive momentum transferred from the neutral gas flow; or 2) the moving dust particles transfer their momentum to a roughly static gas background.

To estimate the neutral drag force, two regimes, divided by the Knudsen number K_n ,

$$K_n = \frac{l_n}{a_d}, \quad (2.37)$$

where l_n is the mean free path of the neutral atoms, must be considered. The case of small Knudsen numbers, $K_n \ll 1$ is called the “*hydrodynamic*” regime. For this case, the neutral drag force can be interpreted employing Stokes law as:

$$\vec{F}_{nd} = -6\pi\eta a_d \vec{v}_d, \quad (2.38)$$

where η is the viscosity of the neutral gas and \vec{v}_d is the relative velocity of the particle. The minus sign implies the direction of the neutral drag force to always be opposite the particle’s direction of motion.

A second case, called the “*kinetic*” regime, occurs where the Knudsen number is much larger than unity, $K_n \gg 1$. In low pressure RF plasmas in the kinetic regime, the mean free path of the neutrals (\sim mm) is usually much larger than the particle’s radius (\sim

μm). Only the “*kinetic*” regime will be only considered in this dissertation. When the relative velocity between the particles and the gas flow is very small in comparison to the neutral thermal velocity, i.e., $|\bar{v}_d - \bar{u}_n| \ll v_{T_n}$ where \bar{u}_n is the gas flow velocity and $v_{T_n} = \sqrt{k_B T_n / m_n}$ is the neutral thermal velocity, the neutral drag force can be expressed by (Epstein 1924):

$$\bar{F}_{nd} = -\frac{4}{3} \pi a_d^2 m_n n_n v_{T_n} (\bar{v}_d - \bar{u}_n) \quad (2.39)$$

for the case of specular reflection, and as

$$\bar{F}_{nd} = -\frac{8}{3} \sqrt{2\pi} a_d^2 m_n n_n v_{T_n} (\bar{v}_d - \bar{u}_n) \left(1 + \frac{\pi}{8}\right) \quad (2.40)$$

for the case of perfect diffuse reflection. Here, n_n and m_n are the density and mass of the neutral atoms, respectively.

For relatively high velocities, i.e., $|\bar{v}_d - \bar{u}_n| \gg v_{T_n}$, the neutral drag force can be given by:

$$\bar{F}_{nd} = -\pi a_d^2 m_n n_n v_{T_n} (\bar{v}_d - \bar{u}_n) |\bar{v}_d - \bar{u}_n|, \quad (2.41)$$

which is the same for both specular reflection and perfect diffusion. In most dusty plasmas, the relative velocity between the particles and the gas flow is always much smaller than the neutral thermal velocity $|\bar{v}_d - \bar{u}_n| \ll v_{T_n}$. This implies that the Epstein drag expression is a good approximation for the neutral drag force. In more realistic models of a dusty plasma, the collisions between the neutral atoms and the dust particles are neither specular reflection nor perfection diffusion; thus, a constant coefficient is introduced to express a more realistic collision style by comparing the expressions (2.39) and (2.40):

$$\bar{F}_{dn} = -\beta m_d \bar{v}_d, \quad (2.42)$$

where β is the damping rate coefficient (also called the *Epstein coefficient*):

$$\beta = \delta \frac{4\pi}{3} \sqrt{\frac{8}{\pi}} \frac{n_n m_n v_{T_n}}{m_d} a_d^2, \quad (2.43)$$

In Eq. (2.43), the coefficient δ represents the collision mechanism. When $\delta = 1.0$, specular reflection dominates while $\delta = 1.44$ corresponds to perfect diffusion (Konopka *et al* 2000). The δ value for melamine-formaldehyde (MF) has been experimentally determined by several groups (Konopka *et al* 2000; Liu *et al* 2003), with all measured results demonstrating good agreement with the Epstein expression. The Epstein coefficient was measured in the CASPER GEC RF reference cell to be $\beta = 0.195p$, where p is the discharge gas pressure in units of mTorr for MF particles of diameter $8.9 \mu\text{m}$, implying $\delta = \sqrt{8/\pi}$ (see Chapter Four).

As shown in Chapter Three, the CASPER GEC RF reference cell minimizes gas flow in the discharge chamber, allowing the gas flow effect to be negligible.

2.6.4. Ion Drag Force

The ion drag force is defined as the momentum transferred from the flowing ions to the charged particles immersed in a dusty plasma. The ion drag force plays an important role in affecting or even determining the dust symmetry configuration in either a laboratory or microgravity plasma and can result in “string chains” in the vertical direction (Morfill, Thomas H 1996), “voids” in the center of the discharge (Fortov *et al* 2004b) under microgravity experiments and a host of others. Compared to the neutral drag force, the ion drag force is much more complicated due to the additional interaction resulted from the charge on the particles.

There are basically two approaches for deriving the ion drag force in a dusty plasmas: the “*binary collision approach (BC)*” and the “*linear dielectric response formalism (LR) (kinetic approach)*.” The traditional way to calculate the ion drag force employs a *BC* approach in which the force is obtained by summing the momentum transferred from the ions and averaging over the ion velocity distribution (Barnes *et al* 1992). In the alternative *LR* approach, instead of calculating single ion trajectories, the Poisson equation coupled to the kinetic equation is solved and a self-consistent electrostatic potential around the particle is obtained. The polarization electric field at the origin of the particle then gives the ion drag force (Ivlev *et al* 2004a, 2004b, 2005). These two approaches are complementary rather than competitive. The *BC* approach is more suitable for use in highly nonlinear collisions, when both the ion Coulomb radius (Fortov *et al* 2005) and the mean free path are larger than the screening length, and the ions have subthermal velocity and are strongly coupled to the particles. On the other hand, the *LR* formalism is necessary to account self-consistently for ion-neutral collisions and the effects of potential and ion distribution function anisotropies.

Binary collision approach. There are three ways to transfer the momentum from the flowing ions to a dust particle: 1) collection of ions on the dust surface, 2) electrostatic Coulomb collisions, and 3) ion fluid flow effects which distort the shape of the Debye sheath around the dust particle (Shukla, Mamun 2002). The corresponding ion drag forces due to these three effects are labeled the “*collection drag force*” (\bar{F}_{id}^{coll}), the “*Coulomb drag force*” (\bar{F}_{id}^{coul}) and the “*ion flow drag force*” (\bar{F}_{id}^{flow}), respectively. The total ion drag force can thus be expressed by:

$$\vec{F}_{id} = \vec{F}_{id}^{coll} + \vec{F}_{id}^{coul} + \vec{F}_{id}^{flow} \quad (2.44)$$

Compared to the other two ion drag forces, the ion flow drag force is much more difficult to calculate and will be neglected here due to its minor contribution to the experiments at hand (Northrop and Birmingham 1990). The collection drag force represents the momentum transferred from ions collected by the dust particle, thus this component can be expressed as (Barnes 1991):

$$\vec{F}_{id}^{coll} = n_i v_s m_i \bar{u}_i \pi b_c^2, \quad (2.45)$$

where $v_s = (8k_B T_i / \pi m_i + u_i^2)^{1/2}$ is the total ion speed (combination of thermal and flow speed). Here, a static dust particle and streaming ions are assumed. The collection impact parameter is given by (Chen 1965):

$$b_c = a_d \left(1 - \frac{2e\varphi_d}{m_i u_i^2} \right)^{1/2}. \quad (2.46)$$

The Coulomb drag force is given by (Bittercourt 1986):

$$\vec{F}_{id}^{coul} = n_i v_s m_i \bar{u}_i 4\pi b_{\pi/2}^2 \Gamma, \quad (2.47)$$

where

$$b_{\pi/2} = a_d \frac{e\varphi_d}{m_i u_i^2} \quad (2.48)$$

is the impact parameter assuming a 90° deflection, and

$$\Gamma = \frac{1}{2} \ln \left(\frac{b_{\pi/2}^2 + \lambda_D^2}{b_{\pi/2}^2 + b_c^2} \right) \quad (2.49)$$

is the Coulomb Logarithm.

Linear dielectric response formalism. A charged dust particle immersed in a flowing plasma induces plasma polarization. The magnitude of the polarization field at

the charge origin $r = 0$ determines the force acting on the dust particle due to the flowing ions: $\vec{F}_{id} = -eZ_d \nabla \varphi|_{\vec{r}=0}$ (Lifshitz and Pitaevskii 1981; Vladimirov *et al* 2003). The ion drag force can be found by integration (Ivlev *et al* 2004b, 2005):

$$F_{id} = -\frac{ie^2 Z_d^2}{\pi} \int_0^{k_{\max}} \frac{dk}{k} \int_{-k}^k \frac{k_{//} dk_{//}}{\varepsilon(0, \vec{k})}, \quad (2.50)$$

where $k_{//}$ represents the portion of the wave vector along the ion flow direction,

$\varepsilon(0, \vec{k}) = 1 + \chi_e + \chi_i$ is the plasma permittivity and $\chi_{e,i}$ is the electron/ion susceptibility.

Assuming a Boltzmann distribution, the electrons give $\chi_e = (k\lambda_{De})^{-2}$ while the ion susceptibility is much more complicated. Here, the results of integrating Eq. (2.50) are directly given. The details can be found in several theoretical publications (Ivlev *et al* 2004a, 2004b, 2005) for: 1) the case of subthermal flow, $u = u_i / v_{Ti} \ll 1$,

$$F_{id} \simeq \frac{1}{3} \sqrt{\frac{2}{\pi}} \left(\frac{T_i}{e} \right)^2 \left[\ln \beta_T^{-1} + \frac{1}{\sqrt{2\pi}} K(\lambda_D / l_i) \right] \beta_T^2 u + O(u^3), \quad (2.51)$$

where

$$K(x) = x \arctan x + \left(\sqrt{\frac{\pi}{2}} - 1 \right) \frac{x^2}{1+x^2} - \sqrt{\frac{\pi}{2}} \ln(1+x^2) \quad (2.52)$$

is the collision function, $\beta_T = e^2 Z_d / \lambda T_i$ is the thermal scattering parameter and λ is the effective screening length; and 2) the case of superthermal flow $u \gg 1$,

$$F_{id} \simeq \sqrt{\frac{2}{\pi}} \left(\frac{T_i}{e} \right)^2 \ln \left(4 \frac{l_i}{\lambda_D} \frac{u}{\beta_T} \right) \beta_T^2 u^{-1} + O(u^{-2}). \quad (2.53)$$

Hybrid approach. Khrapak (Khrapak *et al* 2005b) employed both *BC* and *LR* approaches to develop a “*hybrid*” approach to the problem above: in this case, the *BC* approach yields an expression for the ion drag force for weakly nonlinear scattering at

subthermal flow velocities, finite particle size, and a particle charge dependent on the ion flow velocity, whereas the LR formalism is applied to study the effect of potential anisotropy resulting from the ion flow. Employing this “hybrid” approach, assuming a shifted Maxwellian ion velocity distribution and a Yukawa potential interaction, and combining contributions from both scattering (Coulomb drag) and collection (collection drag), the general expression for the ion drag force on a dust particle in an arbitrary ion flow is given by:

$$F_{id} = \sqrt{2\pi} a_d^2 n_i m_i V_{Ti}^2 \left\{ \sqrt{\frac{\pi}{2}} \operatorname{erf} \left(\frac{u}{\sqrt{2}} \right) \left[1 + u^2 + (1 - u^{-2})(1 + 2z\tau) + 4z^2 \tau^2 u^{-2} \ln \Lambda \right] \right. \\ \left. + u^{-1} \left[1 + 2z\tau + u^2 - 4z^2 \tau^2 \ln \Lambda \right] \exp \left(-\frac{u^2}{2} \right) \right\}. \quad (2.54)$$

In this expression, $u = u_i / v_{Ti}$ is the ratio of the ion flow velocity to the ion thermal velocity and the Coulomb logarithm $\ln \Lambda$ is expressed by:

$$\ln \Lambda = \ln \left[\frac{R + \lambda_D}{R + a_d} \right], \quad (2.55)$$

where $R = z\tau a_d / (1 + u^2)$. It should be mentioned that the dimensionless charge z is calculated using the DML approach and is thus a function of the ion flow velocity, u . Additionally, the Debye length is modified as a function of the ion flow velocity due to its anisotropy and can be simply modeled as:

$$\lambda(u) = \left[\lambda_{Di}^{-2} (1 + u^2)^{-1} + \lambda_{De}^{-2} \right]^{-1/2}, \quad (2.56)$$

In this dissertation, the formula (2.54) is employed to calculate the ion drag force.

Figure 2.8 shows the numerical results from Khrapak *et al*'s work which indicated the dependence of the ion drag force on the ion flow velocity and the electric field using

Eq. (2.54). Typical values for the plasma parameters in an RF discharge were used, i.e., ion temperature $T_i \sim 0.03$ eV, electron temperature $T_e \sim 1$ eV, plasma density $n \sim 3 \times 10^9$ cm⁻³ particle radius $a = 1$ μ m and argon gas pressure $p = 75$ mTorr. Using these typical parameters, the ion drag force increases with the ion flow velocity, reaching a maximum value when the ion flow velocity becomes approximately two times the ion thermal velocity. The ratio of the ion drag force to the electric force exceeds unity when the electric field is small ($E < 11$ V/cm) and rapidly decreases with increasing electric field when the electric field is large ($E \geq 4$ V/cm). These results indicate that for the case of presence of a strong electric field, the ion drag force may become negligible in comparison to the electric force.

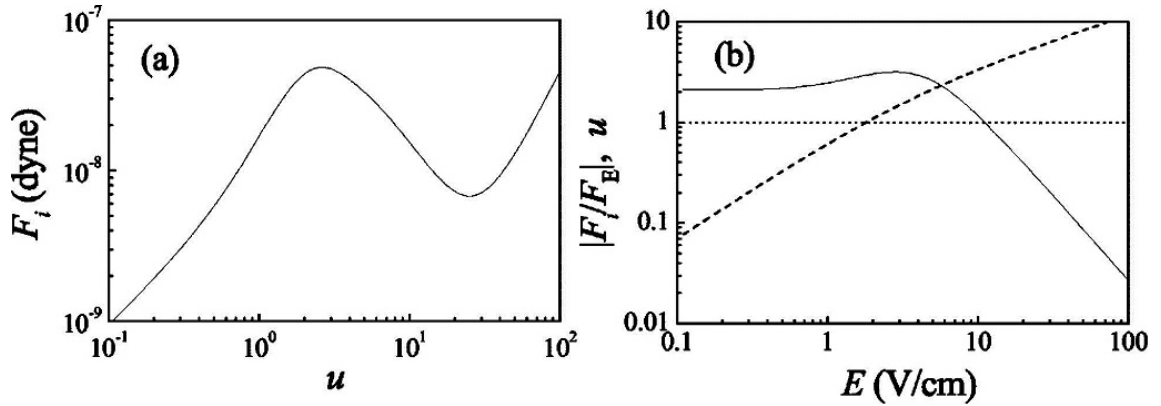


FIG. 2.8. (a) The dependence of the ion drag force F_i on the normalized ion flow velocity $u = u_i / V_{Ti}$. The curve is calculated using the general expression of Eq. (2.54) and a representative set of complex plasma parameters (see text). (b) The ratio of the ion drag force F_i to the electric force F_E as a function of the electric field E (solid line). The dashed line shows the dependence of u on E as found from the Frost approximation (Frost 1957). Points of intersection of these curves with the horizontal dotted line correspond to $|F_i/F_E| = 1$ and $u = 1$. For complex plasma parameters investigated in this paper this occurs at $E \cong 11$ V/cm ($u \cong 3.6$) and $E \cong 1.7$ V/cm, respectively (Khrapak *et al* 2005b).

2.6.5. Particle Interaction

Electrostatic repulsion. The electrostatic potential surrounding a spherical dust particle in a plasma with equilibrium charge Q_d is called the *screened Coulomb potential* or *Yukawa potential*

$$\varphi(r) = \frac{Q_d^*}{4\pi\epsilon_0 r} e^{-r/\lambda_D}, \quad (2.57)$$

where Q_d^* is the effective charge given by (Tsytovich and Angelis 1999)

$$Q_d^* = \frac{Q_d}{1 + a_d/\lambda_D} e^{a_d/\lambda_D}. \quad (2.58)$$

In most dusty plasma research, the radii of the dust particles are always much smaller than the plasma Debye length; thus, the effective charge becomes the equilibrium charge Q_d on the particle. Consequently, the interaction force between two dust particles separated by Δ can be obtained by the multiplication of particle charge and gradient of electrostatic potential:

$$\vec{F}_{\text{int}} = -Q_d \frac{\partial \varphi(\vec{r})}{\partial r} \frac{\vec{r}}{r} \Big|_{r=\Delta}. \quad (2.59)$$

Experimental measurements of the particle interaction potential and forces will be discussed in Chapter Four.

Ion wakefield. As mentioned earlier, when there are multiple dust layers within a dust crystal in a dusty plasma, particles in lower layers always reside immediately below particles in upper layers, resulting in filamentary or vertical chain structure. This alignment structure cannot be adequately explained by a single minimum energy configuration argument alone for a pure repulsive Yukawa interaction. Both simulation

(Schweigert *et al* 1996) and experiment (Melzer *et al* 1999) have shown that the force between two particles levitated at different height in the sheath is a nonreciprocal attractive force: the particle located closest to the lower electrode is attracted by the upper particle, whereas the upper particle only experiences a repulsive force from the lower particle. In others words, when the upstream particle moves, the downstream particle follows, however, when the downstream particle is moved, the upstream particle remains stationary.

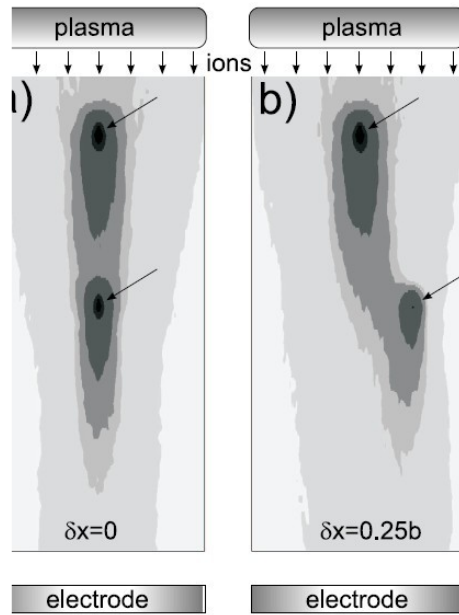


FIG. 2.9. Simulated ion density distribution around dust particles in the plasma sheath when a) the dust particles are vertically aligned ($\delta x = 0$) and b) when they are shifted horizontally by a quarter of the interparticle distance ($\delta x = 0.25b$). (Schweigert *et al* 1996; Melzer and Goree 2005)

This nonreciprocal attraction is primarily due to the ion streaming motion in the sheath region between the bulk plasma and the lower electrode (see Fig. 2.9). The ions enter the sheath with the Bohm velocity and are accelerated by the electric field to become supersonic. Before reaching the lower electrode, they pass through the dust particles levitated in the sheath. The local electric field due to the charge residing on the

upper dust particle attracts positive ions, modifying distorts their trajectories, yielding a region of enhanced positive charge downstream of the upper particle which attracts the lower dust particle. Thus, the shielding of the upper dust particle is distorted downwards by the downwards streaming ions. This is called the “*ion wakefield effect*” and the positive charge region below the upper particle is known as “*wakefield*.” Since the ions move downwards at supersonic speed in the sheath, this attraction can only be applied downwards but not upwards. Thus, only the lower particle feels the attraction but not the upper particle. This nonreciprocal attraction has been demonstrated using dust molecules employing various techniques (Melzer *et al* 1999, 2000; Hebner *et al* 2003a, 2003b). For example, Melzer *et al* employed a laser manipulation technique in a system consisting of two vertically aligned particles with different mass (Fig. 2.10). It was experimentally shown that the lower particle followed the upper particle when pushed by the radiation pressure of a laser beam, while the upper particle remained at equilibrium when the lower particle was pushed (see Fig. 2.11). Calculating the force balance between laser pressure and the attractive force on the lower particle when pushed, the attraction was determined (see Fig. 2.12). Both simulation and experiment have shown that the wakefield residing below the upper particle can be simulated as a single positive point charge with a charge Q_+ located at a position d_+ below the upper particle. In Melzer *et al*’s experiments, the values of $Q_+ = 0.8Q_d$ and $d_+ = 0.29d$ (d is the particle interspacing) showed good agreement with simulation.

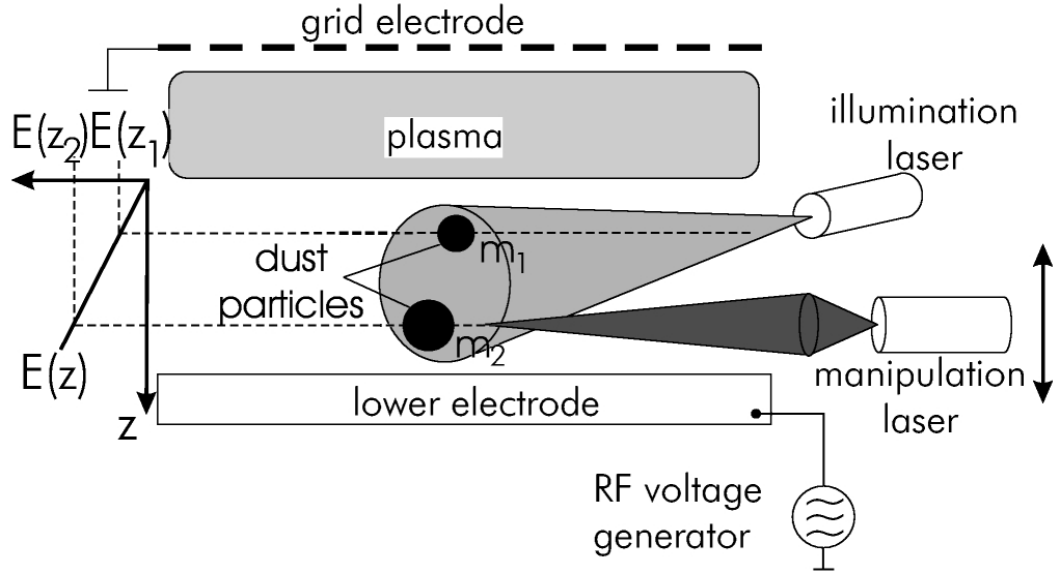


FIG. 2.10. Scheme of particle trapping in the plasma sheath of an RF discharge. Two particles of different mass found their equilibrium position at different heights above the electrode. Each of the particles could be manipulated by a focused laser beam that allowed one to exert a controllable force onto either the upper or the lower particle (Melzer *et al* 1999).

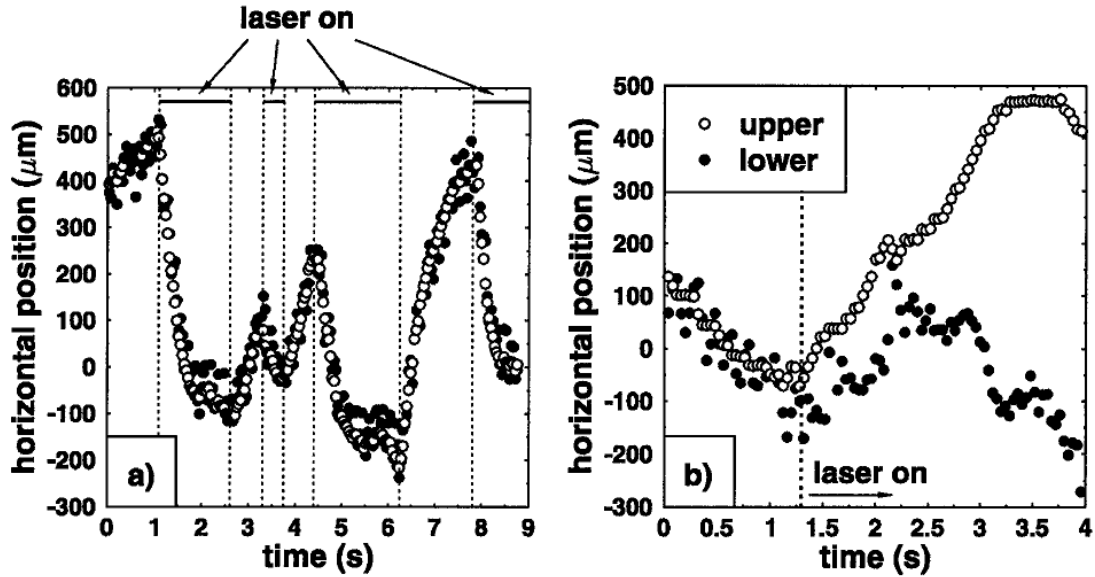


FIG. 2.11. Analysis of the video sequences in the aligned state at 412.5 mTorr when (a) the upper and (b) the lower particle was pushed by the laser beam (Melzer *et al* 1999).

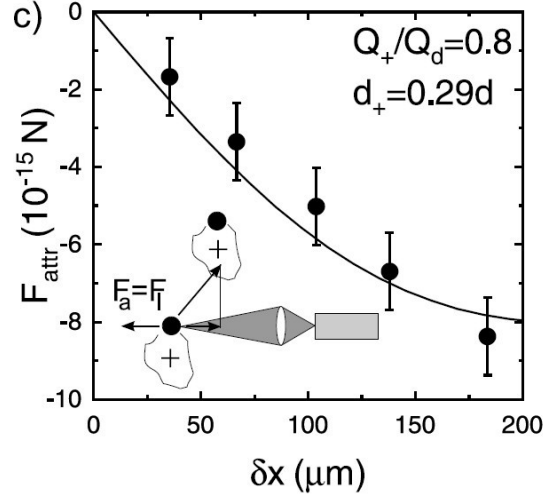


FIG. 2.12. Horizontal component of the attractive force on the lower particle as a function of displacement from the vertically aligned position. The symbols denote experimental values from laser manipulation and the solid line is derived from the simulations. The inset shows a sketch of the experimental setup of the force measurement (Schweigert *et al* 1996; Melzer *et al* 2000).

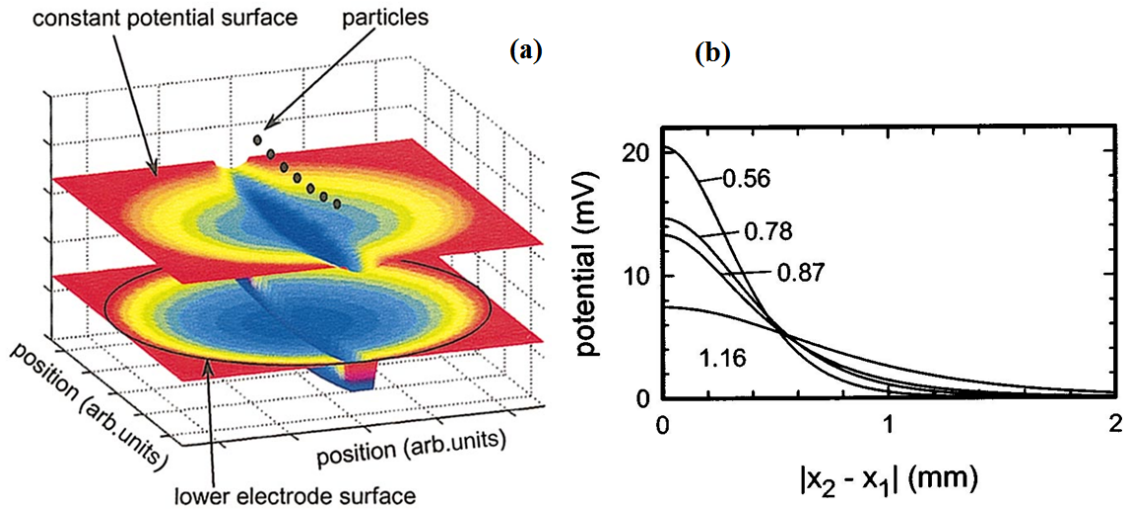


FIG. 2.13. (a) Schematic of a lower RF-driven electrode, a constant potential surface, and the location of the linear particle assembly. The color contours in the lower electrode surface encode height (in arbitrary units) and show the location of the 3-mm-wide by 2-mm deep trench machined into a 0.5 m radius of curvature, 5-cm-diam lower electrode insert (marked by the black circle). An artist rendition of constant potential surfaces is shown above the lower electrode. The particles align themselves on this surface where the gravitational energy is minimized, i.e., above the trench (Hebner *et al* 2003). (b) Potential wells determined from the fits to experimental data of the attractive potentials. The numbers are the distance below (downstream) the upper 6.86 mm diameter particle (Hebner and Riley 2004).

The structure of the wakefield below a dust particle was mapped by Hebner *et al* (Fig. 2.12) employing the head-on collisions between two particles with different masses located at different heights (Hebner *et al* 2003a, 2003b, 2004). A spherically curved lower electrode with a slot cutout was applied to constrain the particles' trajectories within an electrostatic trough (Fig. 2.13 (a)). Analysis of the particles' trajectories and equation of motions yielded the attractive force between these particle pairs. Measurement of the attraction at different positions below the upper particle was achieved using various larger particles as lower particles. Measurements showed the wakefield potential could be modeled as $V(r) = A_w \exp(-\sqrt{r_0^2 + r^2} / \lambda)$ with r the cylindrical coordinate in the radial direction, A_w and r_0 constants depending on plasma and dust parameters and the thermal averaging of ion motion, and λ the screening length of the wakefield potential. The wakefield potential below a $6.86 \mu\text{m}$ diameter particle is shown in Fig. 2.13 (b).

2.7. Waves in Dusty Plasmas

One of the major collective dynamics seen in dusty plasmas is waves. The dust component changes the ordinary plasma composition, affecting conventional plasma wave modes and producing entirely new ones. As shown, a dusty plasma can be in either a weakly coupled (gaseous-like or liquid-like) state, or in a strongly coupled (crystalline) structure. Which of these occurs is determined by the coupling parameter. The properties of waves are different in dusty plasmas in various states. In this section, the coupling parameter which defines the coupling state is introduced. Additionally, the two most common wave modes, the dust lattice wave (DLW) and the dust acoustic wave (DAW), are briefly discussed, and their dispersion relations are derived.

2.7.1. Coupling Parameter

The coupling parameter is defined as the ratio of the particle interaction energy to the particle kinetic energy (Ikezi 1986):

$$\Gamma = \frac{W_{\text{int}}}{E_d}, \quad (2.60)$$

where the interaction energy W_{int} of two particles having the same charge Q_d can be extracted from expression (2.57) assuming a screened Coulomb potential:

$$W_{\text{int}} = \frac{Q_d^2}{4\pi\epsilon_0\Delta} \exp\left(-\frac{\Delta}{\lambda_D}\right). \quad (2.61)$$

The kinetic energy of the dust is easily obtained using:

$$E_d = k_B T_d = \frac{1}{2} m_d \langle v_d^2 \rangle, \quad (2.62)$$

where $\langle v_d^2 \rangle$ denotes the average velocity square over time. Thus, the coupling parameter can be expressed by:

$$\Gamma = \frac{Q_d^2}{4\pi\epsilon_0\Delta k_B T_d} \exp\left(-\frac{\Delta}{\lambda_D}\right). \quad (2.63)$$

A dusty plasma is defined as weakly coupled when $\Gamma < 1$, and as strongly coupled in the opposite limit $\Gamma \geq 1$. Dust particles form crystalline structures when $\Gamma \geq 170$ (Farouki and Hamaguchi 1993). For simplicity, $\Gamma = Q_d^2 / 4\pi\epsilon_0\Delta k_B T_d$ is often used; this is close to the values obtained from (2.63) as long as the inter-particle distance is smaller than the Debye length. If Γ increases while the lattice parameter, defined as the ratio of the inter-particle distance to the Debye length ($\kappa = \Delta / \lambda_D$), remains constant, the dusty plasma can transit from the fluid state to the solid state. For a Yukawa system, the static properties of the system are determined by the coupling parameter Γ and the lattice parameter κ .

This is best illustrated using a phase diagram in the (Γ, κ) plane (see Fig. 2.14) in which the phase transition regions have been marked. For very strong coupling, $\Gamma > \Gamma_{cr}$, where Γ_{cr} corresponds to the values of Γ on the solid-liquid melting curve, there are solid fcc and bcc states while a liquid state exists for $\Gamma < \Gamma_{cr}$. The melting curve can be well fitted by the expression (Vaulina and Khrapak 2000)

$$\Gamma_{cr} = 106 \exp(\kappa) / (1 + \kappa + \kappa^2/2). \quad (2.64)$$

The triple point - the interaction of the fluid-solid and solid-solid phase boundaries - is shown to be at $\kappa = 4.28$ and $\Gamma = 5.6 \times 10^3$ (Hamaguchi *et al* 1997).

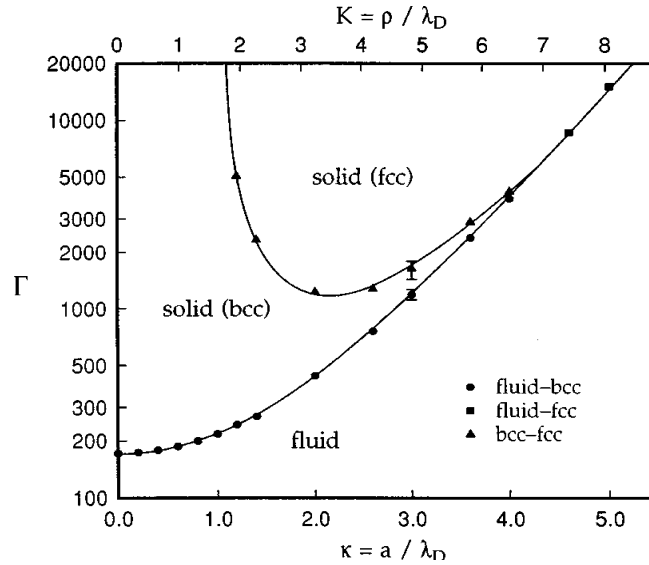


FIG. 2.14. Phase diagram of Yukawa systems in the (Γ, κ) plane. The filled circles and triangles denote fluid-bcc and bcc-fcc boundary points (Hamaguchi *et al* 1997).

2.7.2. Dust Lattice Wave (DLW)

Both longitudinal and transverse dust lattice waves (Wang *et al* 2001) exist in a strongly coupled dusty plasma, analogous to those seen in solid state physics. In dusty plasmas, dust particles interact with one another (primarily with their nearest neighbor)

through a Yukawa potential, which is dependent on the particle charge, inter-particle distance and the screening length. For the purpose of this dissertation, only the longitudinal lattice wave will be considered. Its dispersion relation is derived here.

To simplify the problem, a one-dimensional horizontal particle chain is assumed, with the displacement of each particle denoted as δx_i . The interaction between particles is assumed to be driven by a Yukawa potential and is expressed by:

$$U_{ij} = \frac{q_i q_j}{4\pi\epsilon_0 |r_i - r_j|} \exp\left(-\frac{|r_i - r_j|}{\lambda_D}\right), \quad (2.65)$$

where $q_{i,j}$ and $r_{i,j}$ represent the particle's charge and position, respectively. To further simplify the problem, it is assumed all particles have the same charge and that the interparticle distance is constant $|r_i - r_j| = a$. In this case, the particle's dynamic equation can be obtained using Newton's law:

$$m_d \left(\frac{\partial^2 x_j}{\partial t^2} + \nu_{dn} \frac{\partial x_j}{\partial t} \right) = - \sum_i \frac{\partial U_{ij}}{\partial x}, \quad (2.66)$$

where, ν_{dn} is the neutral drag coefficient (Epstein coefficient). If only nearest neighbor interactions are considered, i.e., $i = j \pm 1$, the right hand side of Eq. (2.66) can be expanded as (Shukla and Mamun 2002)

$$\frac{E(a)q_d}{4\pi\epsilon_0 a} (2\delta x_j - \delta x_{j-1} - \delta x_{j+1}) \quad (2.67)$$

where $E(a)$ is the electric field of any one particle at the inter-particle distance.

Assuming the displacement has time and space dependency $\delta x_j \sim \exp[-i(\omega t - jka)]$, the dispersion relation of the longitudinal lattice wave is obtained through Eq. (2.66):

$$\omega^2 + i\omega v_{dn} = \frac{2q_d^2}{4\pi\epsilon_0 m_d a^3} \left(1 + \frac{a}{\lambda_D} + \frac{a^2}{2\lambda_D^2}\right) \exp\left(-\frac{a}{\lambda_D}\right) \sin^2\left(\frac{ka}{2}\right), \quad (2.68)$$

where ω and k denote the wave frequency and wave number, respectively.

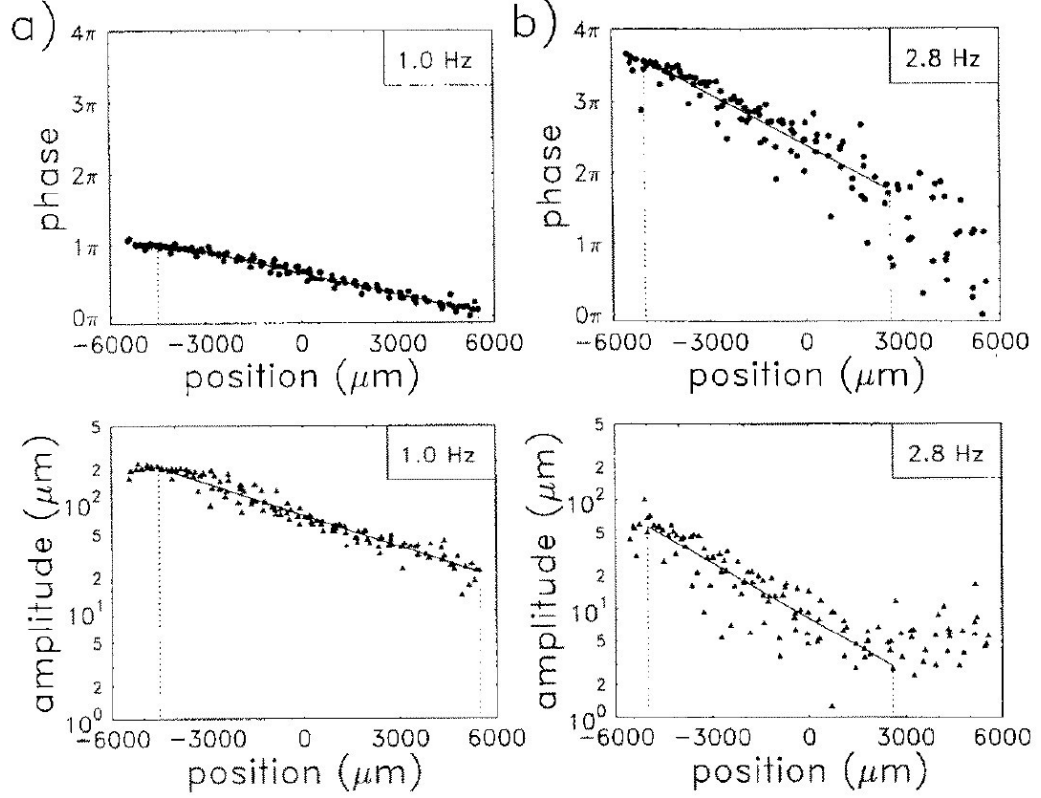


FIG. 2. 15. Phases and amplitudes of the particle oscillations in the direction of wave propagation for two frequencies at 202.5 mTorr: (a) 1 Hz and (b) 2.8 Hz. The dashed vertical lines show the region taken for analyzing the waves (Homann *et al* 1996).

Laser excited longitudinal DLWs were observed by Homann *et al* in 1998. In their experiments, a rectangular barrier of $z = 4$ mm height and an inner spacing of $x = 60$ mm \times $y = 35$ mm was placed on the lower electrode powered at 2 to 3 W to provide rectangular boundaries. The discharge pressure was held at 120 mTorr to 270 mTorr to reduce frictional damping. A single layer dust crystal composed of monodisperse spherical plastic particles of $d_D = (9.5 \pm 0.3) \mu\text{m}$ diameter and a mass density of $\rho = 1514$

kg/m^3 was formed in the sheath above the lower electrode. To excite lattice waves in the crystal, an Ar-Ion-laser of 5 to 8 W output power was used. The laser beam was expanded using a cylindrical lens to a flat, rectangular cross section of approximately 15 mm width and 1 mm height with the laser power fixed during the experiments. The laser beam was inclined to the crystalline layer at a small angle ($\sim 10^\circ$) in order to affect only a few rows of the crystal. A mechanical chopper was employed to modulate the frequency of the laser beam to be between 0.5 Hz and 8 Hz. The amplitude and phase for each particle were obtained by analyzing the particle oscillations. In Fig. 2.15, these quantities are shown for 1.0 Hz and 2.8 Hz at 202.5 mTorr as a function of the particles' x -position. Nonlinear effects were avoided by constraining the particles' amplitude at one third of the inter-particle distance.

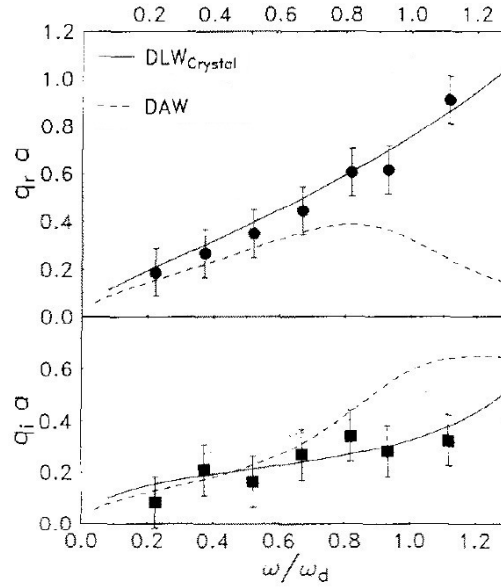


FIG. 2. 16. Theoretical dispersion relation of a DLW and a DAW are shown along with the experimental data for 202.5 mTorr. The DLW dispersion relation (solid line) is plotted for the parameters $Q = 11000e$, $\beta = 11 \text{ s}^{-1}$, $\lambda = 0.8$. $q = q_r + iq_i$, where ω_d is the dust plasma frequency and a is the average inter-particle distance. The curve for the DAW (dashed line) is the best fit for λ . In (a) the real part, and (b) the imaginary part is shown. The DLW is in good agreement with the measured data (Homann *et al* 1996).

The dispersion relation was achieved from the obtained data of frequency and wave number. As shown in Fig. 2.16, the dispersion relation experimentally obtained agrees well with the theoretical DLW model but not with the theoretical DAW model (discussed in next section). Since the dispersion relation depends on both the particle charge and screening length, comparing the experimental dispersion relation to the theoretical dispersion model can be used to determine the charge and screening length.

2.7.3. Dust Acoustic Wave (DAW)

The DAW was first theoretically predicted in a weakly coupled collisionless dusty plasma in 1990 (Rao *et al* 1990). The first experimental observation of spontaneously excited dust waves at a frequency about 12 Hz was reported in 1994 in an RF magnetron discharge (Chu *et al* 1994). After that, numerous experiments were conducted to investigate the properties of DAWs. Figure 2.17 shows a DAW observed in Barkan *et al*'s experiment in a Q-machine (Barkan *et al* 1995). The bright region represents the dust cloud which reflected the illumination from the lasers.

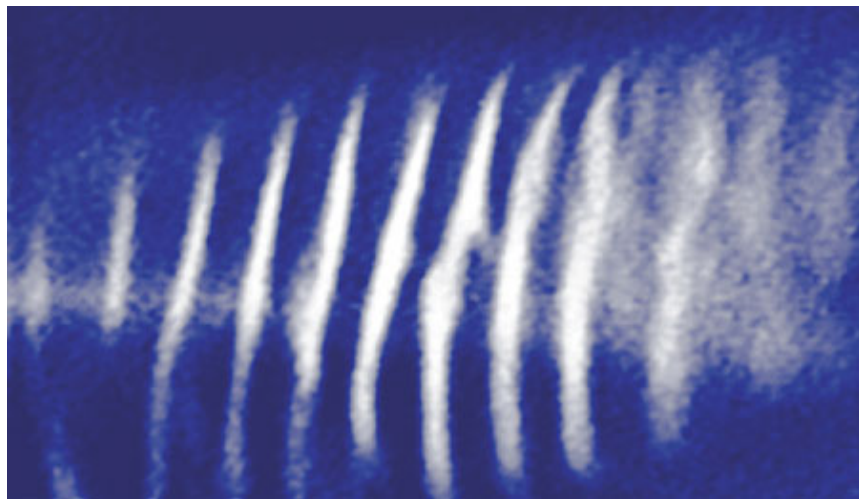


FIG. 2.17. A typical single-frame image of a dust acoustic wave pattern on a video camera (Barkan *et al* 1995).

The dispersion relation for DAWs can be derived from the dust continuity and momentum equations:

$$\frac{\partial n_d}{\partial t} + \nabla \cdot (n_d \bar{u}_d) = 0, \quad (2.69)$$

$$\frac{\partial \bar{u}_d}{\partial t} + \bar{u}_d \cdot \nabla u_d = -\frac{Q_d}{m_d} \nabla \phi - \frac{\gamma k_B T_d}{n_d m_d} \nabla n_d. \quad (2.70)$$

Here, γ is the polytropic index ($\gamma = 1$ for isothermal and $\gamma = 3$ for adiabatic process). ϕ is the local potential which satisfies Poisson equation:

$$-\varepsilon_0 \nabla^2 \phi = en_e - Q_d n_d - en_i. \quad (2.71)$$

The Eqs. (2.69), (2.70), and (2.71) are closed by the quasi-neutrality condition:

$$en_{e0} = en_{i0} + Q_{d0} n_{d0}, \quad (2.72)$$

where the subscript “0” denotes the values at equilibrium state. To simplify the calculation and obtain the dispersion relation, several assumptions must first be made: a) parallel propagation $\vec{k} \cdot \vec{x} = kx$, b) constant particle charge $Q_d = Q_{d0}$, c) linear approximation $n_{e,i} = n_{e0,i0} + n_{e1,i1}$, d) time-space dependency $n_{e1,i1} \sim \exp(-i\omega t + ikx)$, and e) electrons and ions obeying the Boltzmann distribution $n_{e1,i1} \approx \pm n_{e0,i0} (e\phi_1 / k_B T_{e,i})$. Thus, neglecting second order perturbations, Eqs. (2.69), (2.70) and (2.71) become:

$$-\omega n_{d1} + n_{d0} k u_{d1} = 0, \quad (2.73)$$

$$\omega u_{d1} = \frac{Q_d}{m_d} k \phi_1 + \frac{\gamma k_B T_d}{n_d m_d} k n_{d1}, \quad (2.74)$$

$$(k^2 \lambda_D^2 + 1) \phi_1 = \lambda_D^2 Q_{d0} n_{d1} / \varepsilon_0. \quad (2.75)$$

Here, subscript “1” designates a first order perturbation. Substituting (2.73) and (2.74) into (2.75), and cancelling second and higher order perturbations, the dispersion relation can now be written as:

$$\omega^2 = \gamma v_{T_d}^2 k^2 + \frac{k^2 C_{DA}^2}{1 + k^2 \lambda_D^2}, \quad (2.76)$$

where $C_{DA} = \lambda_D \sqrt{Q_{d0}^2 n_{d0} / \epsilon_0} = \omega_{pd} \lambda_D$ is the phase velocity of DAW and ω_{pd} is the dust plasma frequency. In the case of $\omega \gg k v_{T_d}$, the dispersion relation becomes even simpler:

$$\omega = \frac{k C_{DA}}{(1 + k^2 \lambda_D^2)^{1/2}}, \quad (2.77)$$

which in the long wavelength limit, $k \lambda_D \ll 1$, evolves to become the linear dispersion relation $\omega = k C_{DA}$.

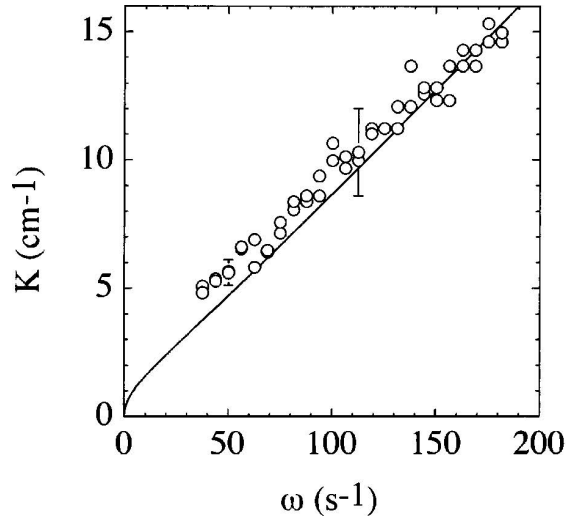


FIG. 2.18. Measured (open circles) dust acoustic wave dispersion relation (wave number K vs angular frequency ω). The solid curve was computed from the fluid dispersion relation (Merlino *et al* 1998).

DAWs have been observed in weakly coupled dusty plasma (Thompson *et al* 1997; Merlino *et al* 1998). There, a glow discharge was generated by applying a positive

potential difference between an anode disk and grounded chamber wall. Dust particles from a tray located beneath the anode were attracted into the glow discharge and trapped. Under certain conditions, DAWs appeared spontaneously in the plasma with a certain wavelength and frequency (see Fig. 2.17). To investigate the dispersion relation of the DAWs, a sinusoidal voltage was applied to the anode to generate waves having different frequencies. By measuring the corresponding wave numbers, a dispersion relation could be then obtained. Figure 2.18 shows an experimentally obtained dispersion relation in comparison with a theoretical DAW model taking into account the neutral drag damping effect. Agreement between experimental measurements and theoretical model is observed.

In summary, in this chapter, the fundamental theory of dusty plasma, which is required for a prior understanding of the experimental and theoretical investigation presented in the following chapters, is briefly described. Two main types of dusty plasmas, plasma sheath in front of electrodes, various particle charging mechanisms, major forces acting on dust particles and collective behaviors (dust acoustic / lattice waves) are presented with short discussions.

CHAPTER THREE

Experimental Setup

3.1. Introduction

The experiments presented in this dissertation were conducted in a modified GEC RF reference cell within the HIDPL at CASPER located at Baylor University. The initial design of the GEC RF reference cell was developed at the 1988 Gaseous Electronics Conference and finalized in March 1989 with the purpose of developing an experimental environment allowing replication and comparison of plasma experiments across different laboratories (Hargis *et al* 1994). The standard GEC RF reference cell within HIDPL was modified to make it suitable for dusty plasma research (Smith 2005). In this Chapter, a brief description of the initial GEC RF reference cell will be given, followed by a summary of the modifications made to the cell within the HIDPL. The vacuum system, vibration minimization techniques, discharge electrodes, RF setup and DC bias will also be briefly introduced. For the purpose of the experiments presented in this dissertation, specific confining configurations will also be described as well as the illumination and detection of the dust particles.

3.2. GEC RF Reference Cell

The initial design for the GEC RF reference cell was established by an *ad hoc* committee formed at the 1988 Gaseous Electronics Conference. The design was based on four guidelines (Hargis *et al* 1994): 1) it could be easily replicated; 2) it would be able

to accommodate a variety of diagnostics; 3) it would be compatible with the reactive gases used in plasma processing, and 4) it would employ discharge geometries relevant to those used in the manufacture of semiconductor devices. The initial GEC design was finalized in March 1989 and six chambers were built and installed in different laboratories to test.

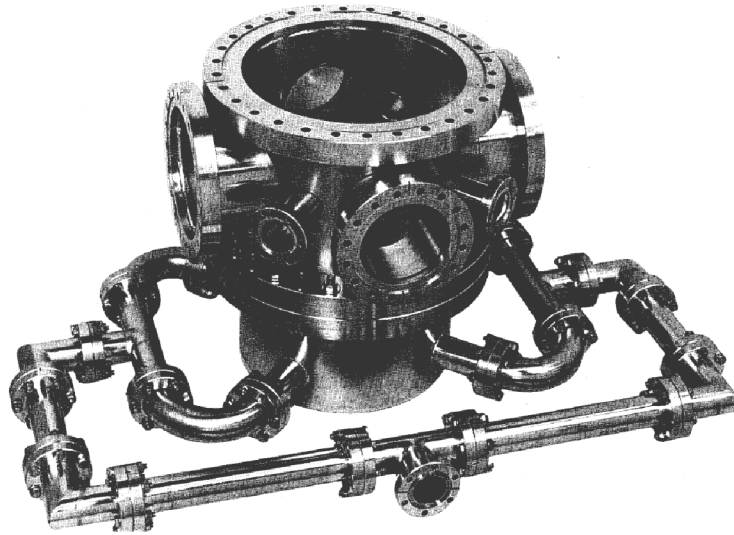


FIG. 3.1. Photograph of the main vacuum chamber of a GEC RF reference cell (Olthoff and Greenberg 1995).

A photograph of the main chamber of a GEC RF reference cell is given in Fig. 3.1 (Olthoff and Greenberg 1995). Conventional stainless-steel ultrahigh vacuum (UHV) sealing technology is employed for all ports and flanges on the chamber and O-rings are used to seal the electrode insulators. The top and bottom flanges of the chamber are 34.29 cm ($13\frac{1}{2}$ in.) in diameter and the chamber internal diameter is 25.1 cm. The distance between the inner surfaces of the flanges is 22.2 cm which is identified as the height of the chamber. As shown, eight ports with 19.5 cm from the face of their flanges to the center of the chamber are located around the main chamber, providing convenient access to the discharge region for diagnostics and observations. Four $2\frac{3}{4}$ in. ports are

utilized for pressure gauges, Langmuir probes, etc., while two 8 in. ports provide optical access to the entire discharge region. Two 6 in. ports are provided, with one being used to connect a turbo-molecular pump to achieve the desired base pressure. As shown in Fig. 3.2 and Fig. 3.3, a “standard configuration” GEC RF reference cell contains two parallel plate electrodes each having a diameter of 10.2 cm (4 in.) with an interspacing fixed at 2.54 cm (1 in.). These electrodes are insulated from the chamber employing electrical insulators which provide access to power, ground or bias for each electrode independently. Ground shields surround the insulators and spread from the electrode mounting flange to the plane of the electrodes. This ground shield minimizes sputtering of the insulator material, helping enhance the uniformity of the electric field between the parallel electrodes.

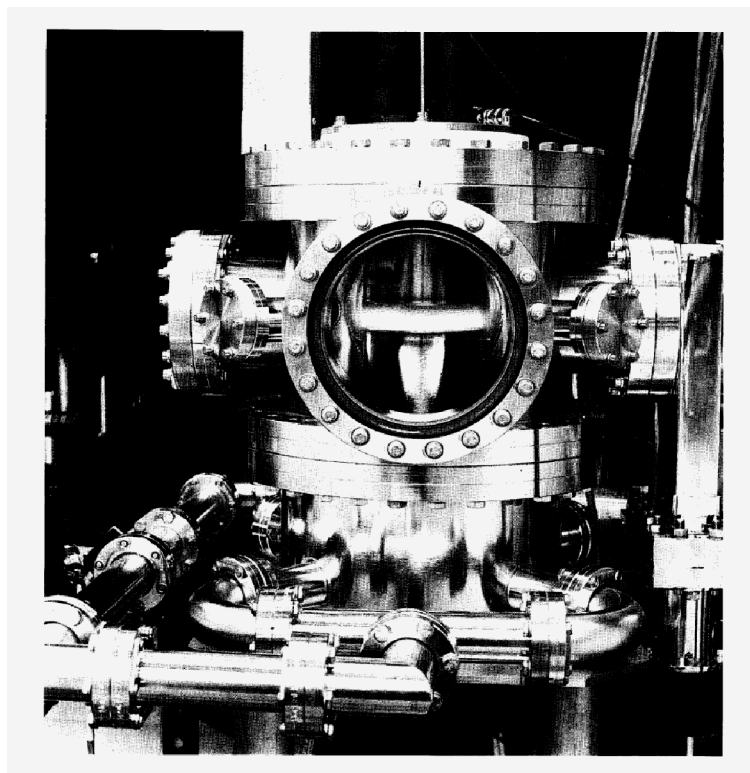


FIG. 3.2. Photograph of a “standard – configuration” GEC RF reference cell sustaining a 200 V, 1 Torr argon plasma (Olthoff and Greenberg 1995).

The GEC reference cell was designed to achieve a base pressure in the range of 10^{-4} mTorr with a 300 l/s turbo-molecular pump and to operate at a maximum pressure of approximate 10 Torr (Hargis *et al* 1994). Gas is supplied to the discharge region through a “showerhead” type upper electrode which has 169 equally spaced holes (0.3 mm in diameter) and pumped out via the symmetric pumping manifold located near the bottom of the cell as shown in Figs. 3.1 and 3.2. This pumping configuration was designed to minimize azimuthal variations in the gas flow at pressures above 100 mTorr since relatively large azimuthal variation takes place when only one pump-out port is used with this reduced to 10% when four symmetric pump-out ports being used (Hargis *et al* 1994).

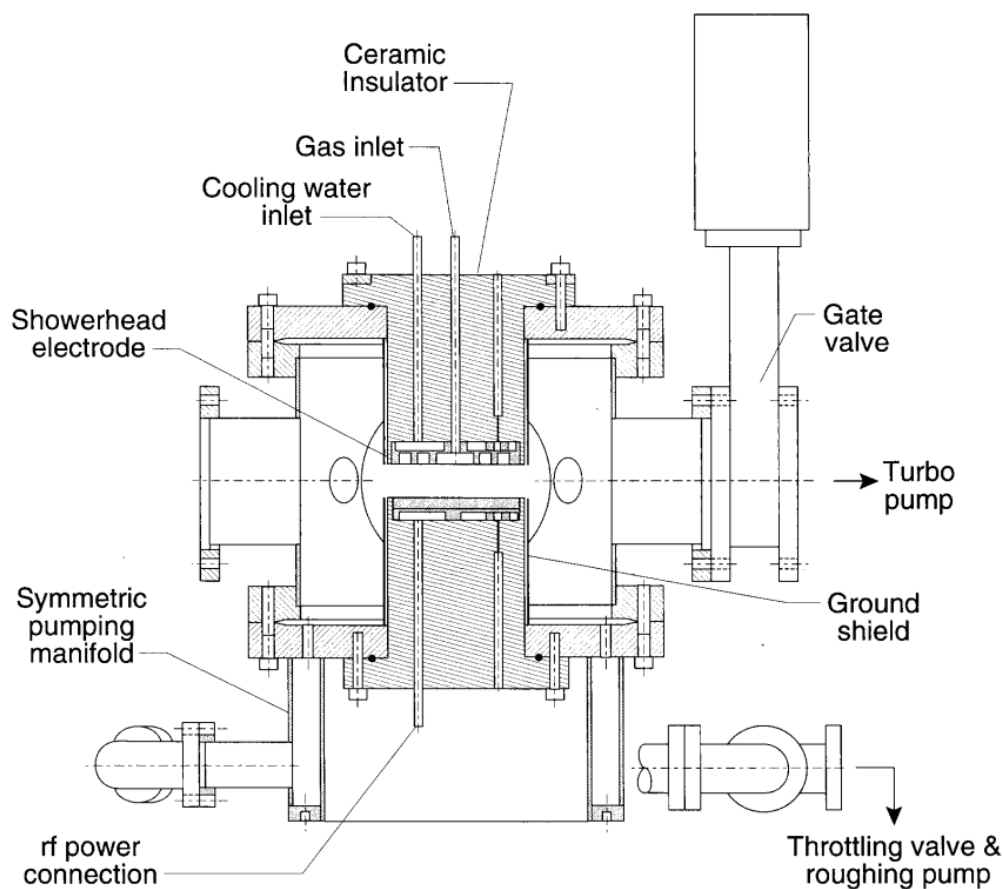


FIG. 3.3. Schematic cross section diagram of a standard-configuration GEC RF reference cell (Olthoff and Greenberg 1995).

3.3. CASPER GEC RF Reference Cell

The reference cell located within the HIDPL at CASPER has been extensively modified in order to be made suitable for dusty plasma research. The details of these modifications have been fully described in the dissertation of Smith (Smith 2005). However, a brief introduction will be presented here.

3.3.1. Vacuum System

The pumping system for the CASPER GEC RF reference cell consists of three pumps: a turbo vacuum pump (Alcatel 5401CP), a roots vacuum pump (RUVAC WS 151) and a rotary vane vacuum pump (TRIVAC D 25 BCS). This combination is able to provide a background pressure of 10^{-4} mTorr (10^{-5} Pa). The roots vacuum pump is backed by the rotary vane vacuum pump, allowing for a high volume of gas to be processed while reducing back-streaming into the pump-out manifold. These two pumps are constrained in a stack (Fig. 3.4 (b)) which is connected to the pump-out manifold through a flexible PVC tube. The turbo vacuum pump (Fig. 3.4 (a)) is only applied when the pressure in the chamber is lower than 10^{-5} Torr (1.33×10^{-3} Pa). A gate valve connects the turbo vacuum pump to an 8 in. chamber port of the chamber to separate the turbo vacuum pump from the chamber when the pressure is above 10^{-5} Torr.

In order to control low vacuum pressure, a butterfly valve is installed between the pump-out manifold and the foreline of the PVC tube. An exhaust valve controller (MKS 252) is employed to open and close the butterfly valve to maintain the desired pressure with the exhaust valve controller reading the pressure from a power supply readout (MKS PDR-C-1C). Finally, the gas flow rate into the chamber is controlled by a mass flow meter (FATHOM GR 112-1-A-PV) and a needle valve (Fig. 3.4 (c)), which for these

experiments was set to 5~20 sccm (standard cubic centimeters per minute). The gas used for generating the plasma examined here was ultra pure argon (99.999%). Nitrogen gas was employed to prevent the chamber from contamination whenever the internal chamber is opened to atmosphere. A schematic of the entire vacuum system for the CASPER GEC RF reference cell is given in Fig. 3.5.

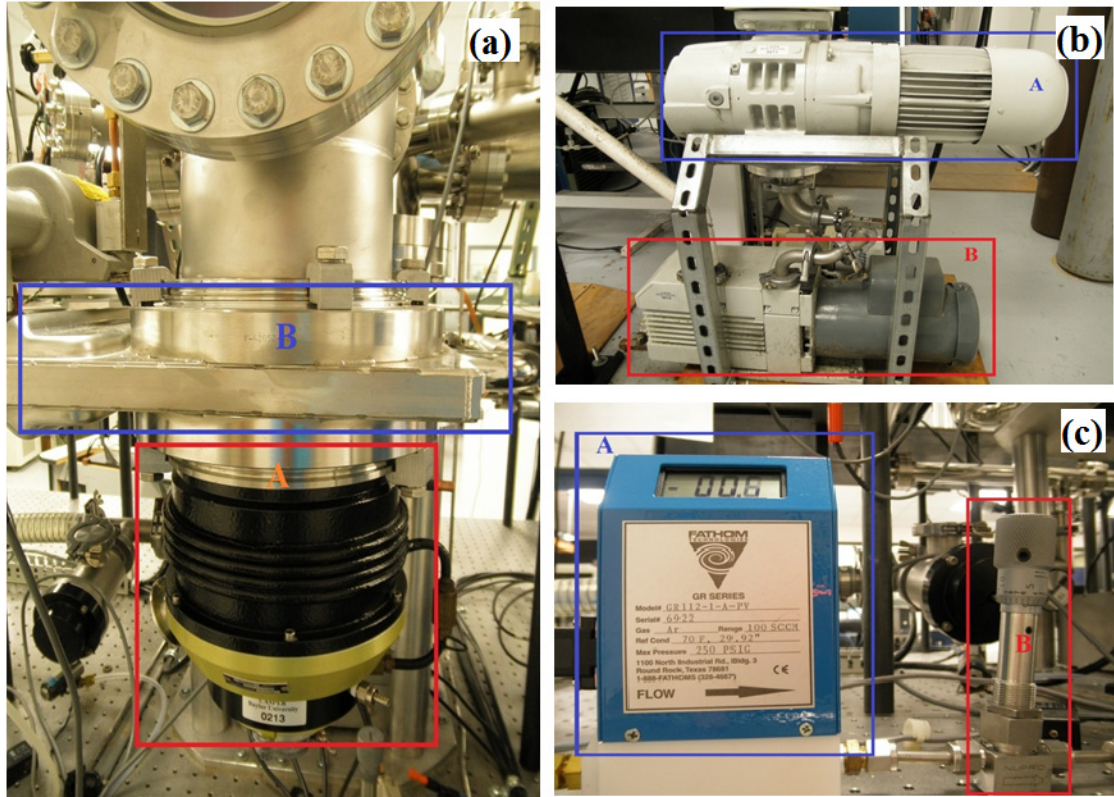


FIG. 3.4. (a) The turbo vacuum pump (A) and gate valve (B). (b) The roots (A) and rotary vane (B) vacuum pumps. (c) The mass-flow control unit (A) and needle valve (B)

3.3.2. Vibration Minimization

The equilibrium location and dynamic motion of dust particles within a dusty plasma are very sensitive to external perturbations. Perturbations can be created intentionally, for example, using lasers (Homann *et al* 1998b), or a modulated DC bias

(Schollmeyer *et al* 1999), or be introduced unintentionally producing unexpected variables which may render the experiment meaningless.

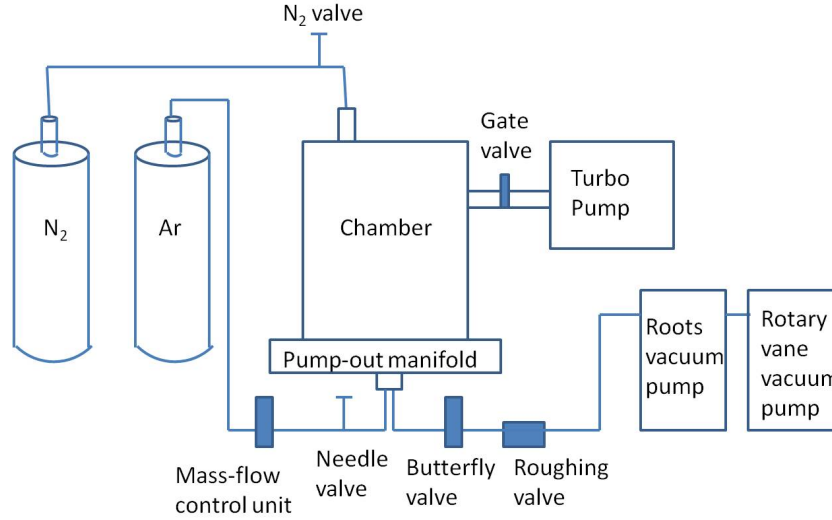


FIG. 3.5. Schematic of the vacuum system for the CASPER GEC RF reference cell.

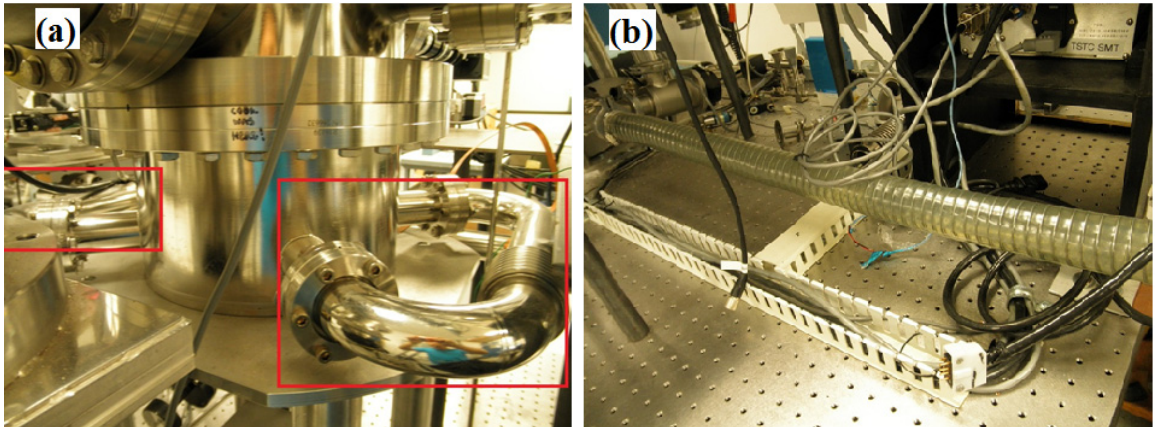


FIG. 3.6. (a) Photograph of the pump-out manifold of CASPER GEC RF reference cell. (b) Photograph of the PVC tube connecting the pump-out manifold and the mechanical pumps.

In the CASPER GEC RF reference cell, special attention is focused on minimizing the external perturbations arising from gas flow in the chamber and vibrations from connected mechanical pumps. To reduce the effect of the gas flow in the

chamber, four symmetric pump-out manifolds are employed as described in the standard GEC RF reference cell (See Fig. 3.6 (a), Fig. 3.1 and Fig. 3.2). To minimize vibrations to the cell from these pumps, a flexible PVC tube is used to connect them to the pump-out manifold (Fig. 3.6 (b)). To insure the system as a whole is level and to minimize external vibrations, the entire CASPER GEC RF reference cell sits on an isolated optical table. This table is suspended by four air bags (Goodyear 1B6-2) which are placed on each leg of the optical table (Fig. 3.7) with the amount of air in each air bag is controlled by pressure regulators.

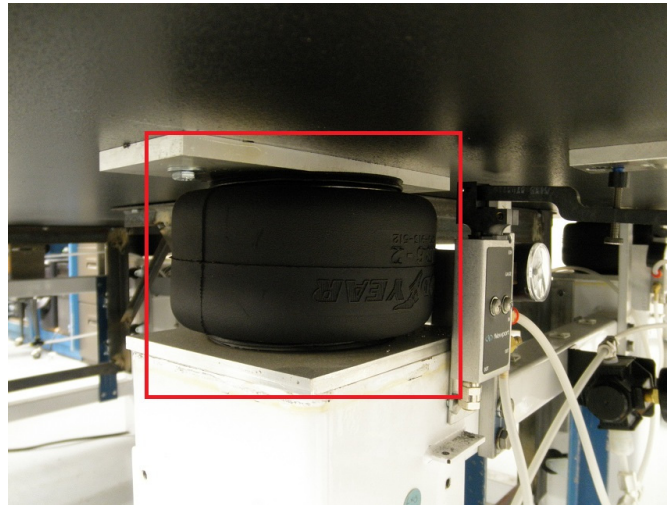


FIG. 3.7. Photograph of one of the air bags underneath the optical table.

3.3.3. Discharge Electrodes

Upper electrode. As described in section 3.1, the main section of the GEC RF reference cell is constructed of a stainless-steel chamber containing two parallel plate electrodes. A capacitively coupled discharge occurs between these two electrodes when the proper power is supplied. In the original GEC reference cell design, the upper electrode consisted of a disk with holes in it in a “showerhead” pattern allowing gas to be

introduced into the system. For the purpose of observation and access to the discharge region between the two electrodes from the top flange, the GEC cell used here has the showerhead upper electrode replaced by a cylindrical ring electrode. This electrode is insulated from the chamber by a Teflon disk, allowing it to be powered, grounded or biased separately from the main chamber. In the experiments in this dissertation, the upper electrode is always grounded through connection to the main chamber via a ground strap. The diameters of the two electrodes are 8 cm and the electrode interspacing is fixed at 1.90 cm.

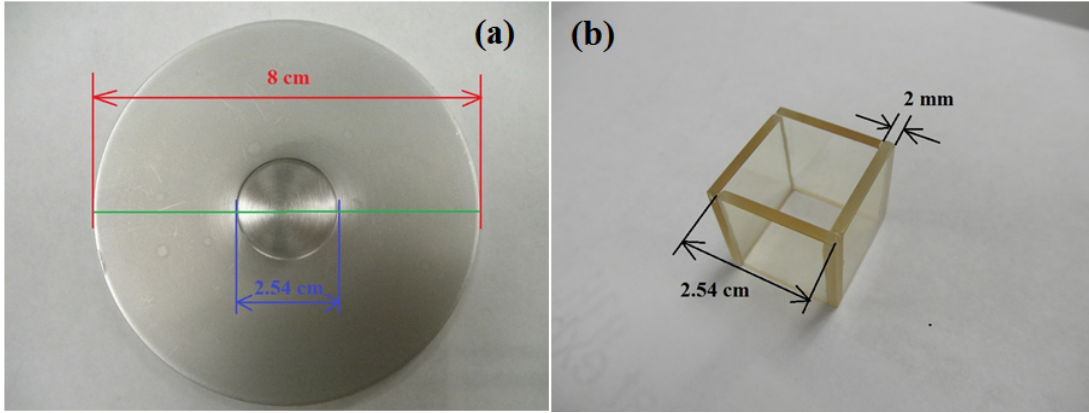


FIG. 3.8. (a) Photograph of the plate which is placed on top of the lower electrode. The milled circular cutout shown is 1 mm deep and helps constrain the dust cloud above the electrode. (b) Photograph of one of two glass boxes used in this work. The boxes are open on top and bottom. When used experimentally, each is located on top of the lower electrode.

Lower electrode and confinement configurations. As mentioned above, the lower electrode in the standard GEC RF reference cell is a flat stainless-steel air-cooled disk, powered by a radio frequency generator at 13.56 MHz through a matching network. Dust particles levitating over the lower electrode move at thermal velocity or are repelled by other charged particles through Coulomb forces. Over a period of time, these particles

move away from the lower electrode and are lost. To constrain the particles within the discharge region, a horizontal force is required. For this purpose, various diameter plates having a central cutout (Chu 1994; Hebner *et al* 2003) or a glass box (Arp *et al* 2004) are placed on the lower electrode in order to provide a horizontal confining force.

In the experiments which will be discussed in Chapters Four and Five, a circular plate having a milled circular cutout (Fig. 3.8 (a)) and two different glass boxes (Fig. 3.8 (b)) were employed. The plate is 2 mm thick and 8 cm (3.15 in.) in diameter with a milled cutout 1 mm deep and 2.54 cm (1 in.) in diameter. The smaller / larger glass box is constructed of four square pieces of glass 1.27 cm / 2.54 cm (0.5 in. / 1 in.) in length and 2 mm thick. As shown in Fig. 3.12, this results in the internal dimensions of the smaller / bigger glass box being $(1.07 \text{ cm})^2 \times 1.27 \text{ cm} / (2.34 \text{ cm})^2 \times 2.54 \text{ cm}$. A capacitively coupled discharge within the CASPER GEC RF reference cell with a glass box on the lower electrode is shown in Fig. 3.9 (a).

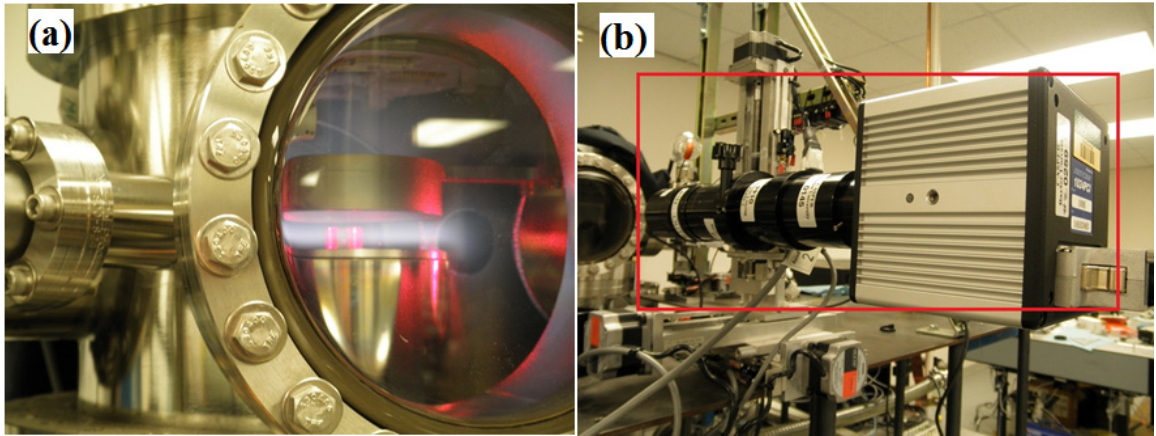


FIG. 3.9. (a) Capacitively coupled RF discharge in the CASPER GEC RF reference cell. The red illumination which can be seen comes from the reflection of the diode lasers on the electrodes and glass box. The glass box is located at the center of the lower electrode with dust particles inside illuminated by a vertical laser sheet. (b) Photograph of the 1024 PC Photron High Speed Camera mounted for side view in the CASPER GEC RF reference cell.

3.3.4. *Illumination and Detection*

Laser setups. The CASPER GEC RF reference cell offers several windows for observation and illumination. Two diode laser setups are designed to illuminate dust particles with minimal radiation pressure perturbation: the horizontal laser sheet and the vertical laser sheet. The horizontal laser is a LASIRISTM SNF Laser with wavelength 685 nm and a power of 50 mW and the vertical laser is a LASIRISTM SNF Laser with wavelength 635 nm and a power of 10 mW. Cylindrical lenses are used to expand the laser produced beam into a laser sheet. The horizontal laser uses a LASIRISTM SNF 5° fan angle, line generating lens and the vertical laser uses a LASIRISTM SNF 1° fan angle, line generating lens. The maximum radiation pressure force for either of these is estimated to be on the order of 10^{-14} N, which is at least two orders of magnitude smaller than the gravitational force (10^{-12} N). Thus, the radiation force can be safely neglected. For accurate control in moving the laser sheets, stepper motors allow the lasers sheets to be moved in the (x, y, z) direction (Fig. 3.10). Both the laser and camera systems have stepper motors attached to screw drive actuators (Velmex UniSlide P40) which provide movement of each stage by a specific distance per step; for the P40 model, this distance is approximate $1.59 \mu\text{m}$ per step. The motors used for the laser and camera systems are different according to their required moving space. The laser systems use Velmex PK245 stepper motors while the camera systems use Velmex MO62 stepper motors.

Camera systems. To record the motion of the dust particles, several camera systems are used. In the CASPER GEC RF reference cell, two CCD (charge coupled device) cameras with microscope lenses are located at the top and side ports of the cell.

Under normal conditions, the cameras used are Sony XC-HR50s which can reach 120 fps (frame per second). The top camera employs a Navitar Zoom 7000 lens, while the lens used on the side camera is an Infinity K2. When higher frame rates are required, a Photron camera (1024 PC Photron High Speed Camera) which can reach a maximum of 10^5 fps is employed (Fig. 3.9 (b)). In the experiments presented in this dissertation, both the XC-HR50 camera running at 120 fps and the Photron camera running at 250 to 1000 fps were used. All data collected by the cameras is immediately stored to a dedicated workstation and is ready for analysis. All cameras are mounted to stepper motors (Velmex MO62) and are free to move in (x, y, z) direction, allowing them to be properly focused (Fig. 3.10).

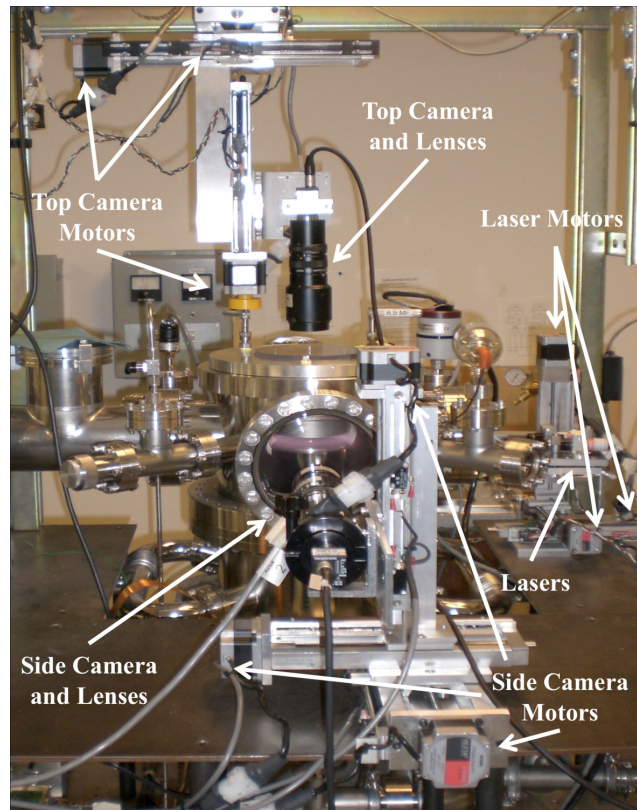


FIG. 3.10. CASPER GEC RF reference cell setup with locations of cameras, lasers and motors marked. The purple glow in the center indicates the main gas discharge region in the chamber (Creel 2010).

3.4. RF Power Setup

In the CASPER GEC RF reference cell, power is delivered to the lower electrode by a power system as shown in Fig. 3.11. To generate a low amplitude RF signal ($\leq 1 V_{\text{rms}}$), a signal generator (Hewlett-Packard 8657A) is employed with the frequency held at 13.56 MHz. Post signal generator, the signal is sent to a VPA (variable passive attenuator) where the signal is increased by 11-31 dBm at a maximum of $1 V_{\text{rms}}$ as controlled by a variable resistor knob. An RF power amplifier (EIN (Electronic Navigation Industries) 420 L) having a 50Ω load is used to amplify the signal from the VPA by approximately 48 dB. Next, the signal is transferred to a tuning network which is necessary to prevent damage to in-line devices (for example, the signal generator and power amplifier) due to reflection of the signal resulting from possible impedance mismatch between the components of the RF system. In such a case, as the impedance mismatch increases, the amplitude of the reflected signal increases. Thus, the tuning network must be used when running a high voltage signal ($> 1 V_{\text{rms}}$). In the case of low voltage signal application, the RF power amplifier and tuning network can be bypassed. The tuning network used here is constructed of two variable capacitors on the powered side of the circuit with one variable capacitor and a constant inductor from power to ground; this results in the tuner capacitively connecting the RF power amplifier to the shunt network, preventing DC current from passing between the amplifier and the shunt. Once a plasma is generated and becomes stable, the tuning network is adjusted to minimize power reflection; this is always set to be less than 10% in the CASPER GEC RF reference cell. Detailed information concerning the entire RF setup can be found in Smith 2005.

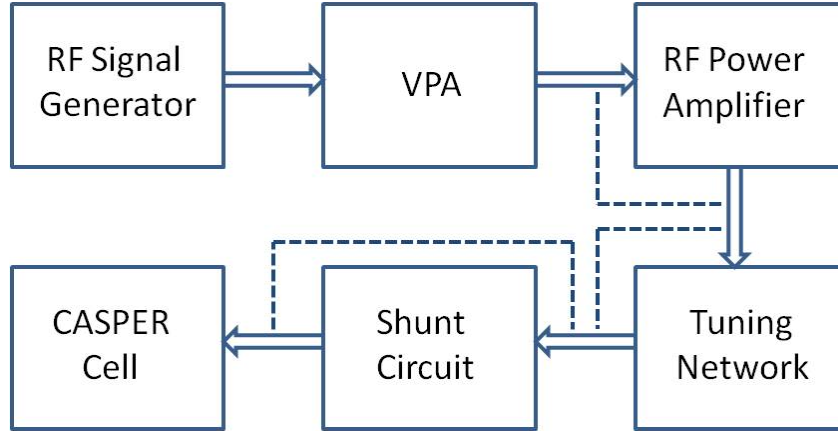


FIG. 3.11. Schematic of the RF power setup used in the CASPER GEC RF reference cell. The dashed lines indicate devices which can be bypassed if needed.

3.5. DC Bias

3.5.1. Self Bias

As discussed in the previous section, there is no DC current passing between the discharge system and its RF power source since they are capacitively coupled. However, in the discharge system itself, under proper conditions, a DC bias can be self-developed, creating a “*self bias*” in the system.

The creation of this self bias is due to the difference between the ion and electron current fluxes to the surface of the electrodes. In an RF discharge plasma, due to their high mobility, the electrons are able to follow the RF sinusoidal circle signal almost instantaneously. This means, in the positive half circle of the RF signal, the electrons are attracted toward the electrodes, while in the negative half circle the electrons are repelled from the electrodes. The ions are too massive to react to the high frequency RF signal (13.56 MHz), and feel only the effective RF signal. The imbalance between the electron and ion current fluxes to the electrodes results in the creation of a DC bias. In the CASPER GEC RF reference cell, this DC self bias is always negative.

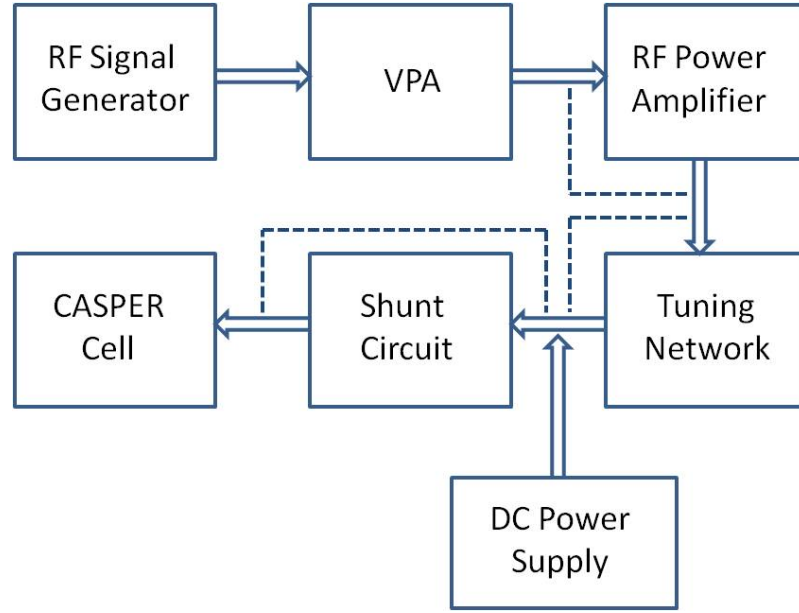


FIG. 3.12. Schematic of the RF power setup of CASPER GEC RF reference cell with a DC power supply. The current from the DC power supply is stabilized and limited by a 15 k Ω resistor.

3.5.2. Variable DC Bias

Since the dust particles are located above the lower electrode in a laboratory RF discharge plasma, the application of a variable DC bias on the lower electrode can be used as an effective tool of experimental investigation in dusty plasma research (Schollmeyer *et al* 1999). To fully employ this advantage, a DC power supply is inserted in the RF power system, allowing the DC bias on the lower electrode to be modulated in a controlled manner. The setup of the DC power supply (KEPCO BOP 500M) used in the CASPER's system is shown in Fig. 3.12. To minimize power dissipation and current flow in the DC power supply, a network with a 15 k Ω resistor is placed in series with the DC power supply. The location of the DC power supply must always be on the cell side of the tuning network, since this has a blocking capacitor protecting the RF power source and RF power amplifier from possible damage which can be caused by the DC bias.

All of the experiments presented in the following chapters were conducted in one of the experimental setups described above. Any small modifications necessary are discussed in Chapters Four and Five.

CHAPTER FOUR

Particle Interaction Measurements

Parts of this chapter have been published as: “Simple method to measure the interaction potential of dielectric grains in a dusty plasma”, Zhuanhao Zhang, Ke Qiao, Jie Kong, Lorin Matthews, and Truell Hyde, *Phys. Rev. E* 82, 036401 (2010)

4.1. Introduction

Dust particle charge and screening length, which together determine the particle-particle and particle-plasma interaction, have long been considered as one of the most fundamental parameters in dusty plasmas. In the short range, the particle interaction potential can be best described as a repulsive screened Coulomb potential (Konopka *et al* 1997). Several experiments (Melzer *et al* 1999; Konopka *et al* 2000; Hebner *et al* 2003; Fortov *et al* 2004a) employing various techniques have demonstrated this screened interaction over the range of several Debye lengths. More recently, theoretical calculations have showed that this interaction potential may have an attractive component at large distances which can overcome the long-range electrostatic repulsion. This attraction can be due to the wakefield (Ignatov 2003), the ion shadowing force (Lampe *et al* 2000; Khrapak *et al* 2001), or the neutral shadowing force (Tsytovich *et al* 1998). Before this work, no experiment had been conducted that could prove this attractive interaction for particles on the same horizontal level. In this chapter, such an experiment, performed in a CASPER GEC RF reference cell, will be described measuring the particle’s interaction potential, particle charge and screening length. The experimental setup employed has already been described in Chapter Three. In section 4.2, previous work contributing to the investigation of the particle interaction potential will be

discussed briefly. Specific single particle techniques and an uncertainty reduction approach will be introduced in section 4.4. Experimental results will be presented in sections 4.5 and 4.6, and comparison with theoretical models will be described in section 4.7.

4.2. Previous Contributions

Considering the importance of the particle-particle interaction to the experimental phenomenon observed in dusty plasmas, enormous efforts have been employed to investigate this interaction, in particularly the particle charge and screening length. Due to the delicate experimental problems which arise and the high level of uncertainty in the analysis, only a few such experiments have been successful. In this section, the major experimental techniques employed to date are briefly described, and their measurement results presented.

4.2.1. Elastic Collision

A succinct approach based on an elastic collision between two particles has been widely employed. To realize this collision, several techniques were employed: probe perturbation (Konopka *et al* 1997; 2000), laser manipulation (Melzer *et al* 1999), slot cutout (Hebner and Riley 2003) and gravity-driven (Fortov *et al* 2004a). During any collision, particle trajectories are determined by the confining potential and the particle-particle interaction, which is a function of the particle charge, screening length and interparticle distance. An analysis of the particle trajectories then yields the velocity and acceleration during the collision. This allows the particle interaction potential to be reconstructed through the integration of the equations of motion, and the particle charge

and screening length can then be extracted employing an interaction potential model, as presented in section 4.4.

Probe perturbation. In Konopka *et al*'s experiments (Konopka *et al* 2000), two melamine-formaldehyde microspheres with diameters $8.9 \pm 0.1 \mu\text{m}$ and densities 1.514 kg/m^3 were located in the sheath by the balance between the gravitational and the electric forces. The discharge gas pressure was fixed at 20 mTorr, and experiments employing different discharge powers were conducted. To provide horizontal confinement, a copper ring with an inner diameter of 40 mm and a height of 2 mm was placed on the lower electrode. A bent tip of a Langmuir probe adjusted about 2 mm below the levitation height of the particles was used to manipulate the particles. The experimental setup is illustrated in Fig. 4.1 (a).

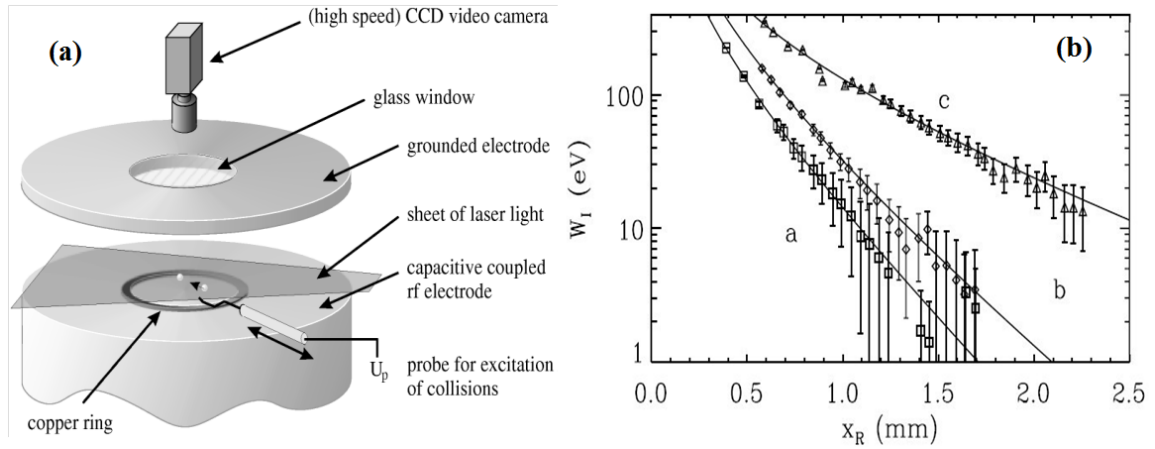


FIG. 4.1. (a) Experimental setup. (b) Potential energy of a single particle during a collision. Measurements were taken at a pressure of 20 mTorr (Ar) and different RF peak-to-peak voltages, U_{pp} . A fit to a screened Coloumb potential is also shown (solid lines) leading to the following effective particle charge Q_{eff} and a screening length λ : (a) $|Q_{eff}| = 13900 e$, $\lambda = 0.34 \text{ mm}$, $T_e = 2.0 \text{ eV}$, $U_{pp} = 233 \text{ V}$; (b) $|Q_{eff}| = 16500 e$, $\lambda = 0.40 \text{ mm}$, $T_e = 2.2 \text{ eV}$, $U_{pp} = 145 \text{ V}$; (c) $|Q_{eff}| = 17100 e$, $\lambda = 0.78 \text{ mm}$, $T_e = 2.8 \text{ eV}$, $U_{pp} = 64 \text{ V}$ (Konopka *et al* 2000).

Initially, a positive voltage was applied to the probe, attracting the particle and drawn near the edge of the confinement (8 mm from the center). The voltage was then removed and the freed particle accelerated back towards the center of the electrode, allowing mapping of the confining potential or a collision with another particle. Measurement results showed the confining potential to be parabolic and that the particle-particle interaction potential (Fig. 4.1. (b)) agreed with that which could be provided by a screened Coulomb potential within experimental uncertainty (10-20%).

Laser manipulation. Melzer *et al* employed a laser to manipulate two particles with different masses in a vertical chain. The top particle had a mass of 3.3×10^{-14} kg and the bottom particle had a mass of 6.6×10^{-14} kg. An expanded laser beam was used to illuminate the particles while a second diode laser (690 nm, 40 mW) with focus diameter of approximate 200 μm was adopted to manipulate the particles through radiation pressure, which was estimated to be of the order of 10^{-15} N. The experimental setup is displayed in Fig. 2.10.

It was found that the interaction between two particles in a vertical chain is nonreciprocal. This means that when the upper particle is pushed, the lower particle follows its motion; whereas, when the lower particle is pushed, the upper particle remains stationary. This phenomenon was explained as a polarization due to the surrounding ion flow.

Slot cutout. In order to examine head-on collisions without introducing either laser or probe perturbation, Hebner *et al* (Hebner *et al* 2003) adopted a slot trough cutout, resulting in collision dynamics constrained to motion in the coordinate axis parallel to the

slot. For this case, the lower electrode was 51mm in diameter and had a shallow 0.5 m radius of curvature cut into its top surface. A slot cut along the diameter, 3 mm wide and 2 mm deep, followed the 0.5 m curvature. Two particle shakers were located at either end of the trench and were used to drop single particles into the electrostatic trough formed by the plasma above the slot (see Fig. 2.13 (a)). A top view of the configuration of the slot trough is shown in Fig. 4.2 (a). Resulting measurements showed the repulsive potential could be well fit by screened Coulomb potential (Fig.4.2 (b)).

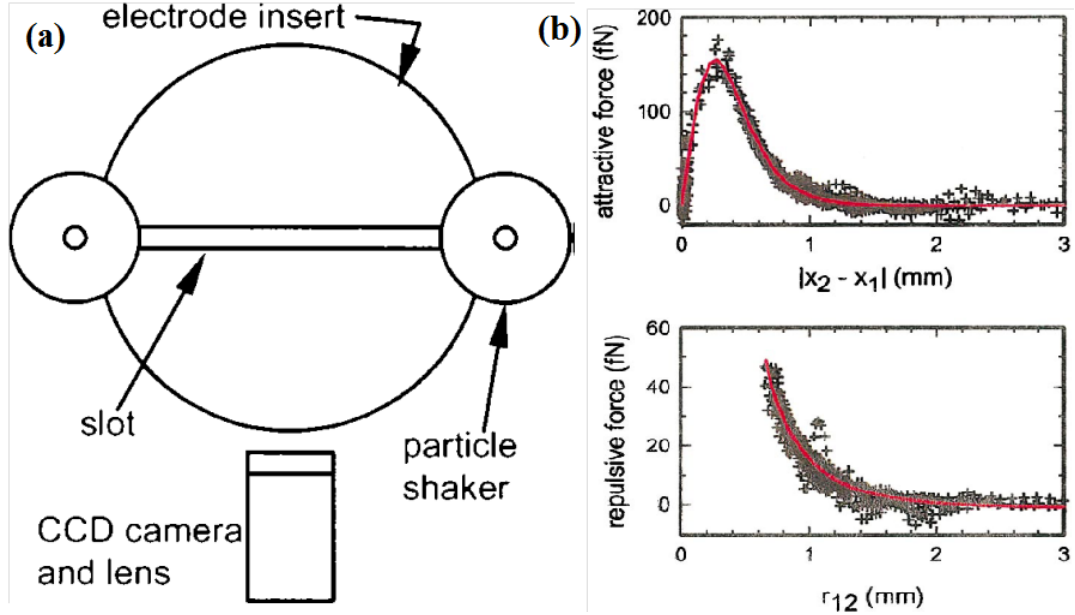


FIG. 4.2. (a) Top view of the experimental configuration. (b) The attractive and repulsive forces derived from analysis of eight collisions. The solid red lines are fits to the attractive potential and repulsive screened-Coulomb form (Hebner *et al* 2003).

Since the dust particles interact with each other in dusty plasmas electrostatically, instead of planting two particles in a dust plasma, it is possible to detect the particle-particle interaction employing a large number of dust particles themselves which either construct a stable crystalline structure or perform collective wave motions as a diagnostic system.

4.2.2. *Crystal Probe*

In 2001, Hebner *et al* (Hebner *et al* 2001) developed an approach employing two-dimensional dust crystals to determine the particle-particle interaction potential. As explained earlier, the size of the dust crystal (total number of particles) is a function of the particle separation at the center of the dust crystal. Hebner *et al* formed different size crystals under the same conditions in order to experimentally determine these relationships. Employing an equation of state for the crystal, the particle charge and screening length were directly determined through fit to a model of a screened Coulomb potential. In these experiments, no evidence of attractive binding was observed. More recently, a similar method was employed by Land *et al* (Land *et al* 2010) to determine the particle charge and screening length using crystals as probes.

A primary advantage of this approach is that it does not require direct measurement of the plasma parameters or an analytical model of the plasma sheath. However, it is important to note that the large number of dust particles present in the sheath creates the “closely packed” effect discussed in Chapter Two. The resulting quasi-neutrality equation is thus modified by the dust charge density, and the surrounding ions and electrons trajectories are distorted by neighboring particles. These effects will affect, and at times dominate particle charging, as shown by Barkan *et al* who found a significant reduction of particle charge due to the large particle number (Barkan *et al* 1994).

4.2.3. *Dispersion Relation Fitting*

Rather than fitting experimental particle interaction data to an analytical model, an alternate method has been developed which measures the particle charge and effective

screening length under the assumption of a Yukawa potential (Peters *et al* 1996; Homann *et al* 1997; Nunomura *et al* 2000). As described in Section 2.6, the dispersion relationship for a dust lattice wave (DLW) can be derived assuming a given particle-particle interaction potential (usually a Yukawa potential) where the main parameters in the resulting dispersion relationship are the particle charge and the effective screening length. Other parameters, such as the particle mass and the interparticle distance, are either known in advance or determined during the experiment. The linear dispersion relationship for a dust acoustic wave (DAW) can also be employed to determine the particle charge, if the screening length can be determined from probe measurement results (Khrapak *et al* 2005a). Unfortunately, as in the crystal probe approach, this method suffers from the “closely packed” effect, and usually must assume a linear approximation during the deduction of the dispersion relationship.

In summary in each of the above, the particles were manipulated by external perturbations applied to the dust plasma. Such perturbations disturb the plasma, resulting deviations of the plasma parameters, the particle charging and screening length. In the crystal probe and wave motion techniques, the “closely packed” effect is always an issue. The currently available particle-particle interaction potential measurements always involve an external perturbation to the plasma and/or assumptions such as a finite dust density, i.e., no “closely packed” effect, linear approximation, etc. Thus, in order to properly describe the physics involved, and achieve more reliable measurement and convenient way to detect the particle interaction, a non-perturbative and no priori assumptions required approach is needed to develop.

4.3. Dependence on Gas Pressure

In addition to the issues raised above, the particle charge and screening length also depend on the discharge pressure. This can easily be concluded from the charging models in Chapter Two. For example, in both the OML and DML models, the ion and electron densities are determined by the discharge pressure, and in weakly collisional DC discharges, the ion mean free path which is strongly related to the discharge pressure. Ratynskaia *et al* (Ratynskaia *et al* 2004) and Khrapak *et al* (Khrapak *et al* 2005a) investigated both computationally and experimentally the pressure effect on the particle charge in a DC bulk plasma employing small grain particles (0.6, 1.0, and 1.3 μm in radii), as shown in Fig. 2.7. Their work showed that both the particle charge and the screening length decreased with increasing pressure. The application of these results to particles levitated in the sheath of the RF plasma, however, has been uncertain as there are significant differences between the RF sheath region and the DC bulk plasma (see Section 2.2.).

4.4. Single Particle Technique

In this dissertation, a simple, minimally perturbative method is employed to simultaneously investigate both the radial confining potential and the particle interaction potential. This is accomplished by introducing a single particle into the system which then collides with a second particle already residing at the equilibrium point within the sheath region. The damped motion of the resulting head-on collision is analyzed to determine the radial confining potential and the particle interaction potential. In contrast to previous work, this technique introduces no external perturbation of the system, allowing the plasma parameters to be reliably assumed as constant throughout the

experimental period. This approach also allows the first experimental determination of the effect of pressure on the charge of a particle levitated in the sheath of an RF plasma under gravity.

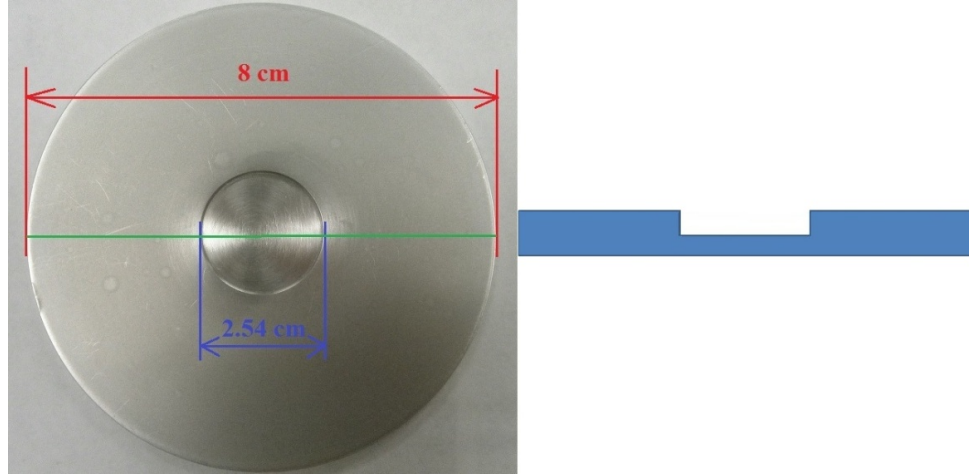


FIG. 4.3. The plate placed on top of the lower electrode. Right picture is top-view photograph, while the right one is side-view structure. The milled circular cutout shown is 1 mm deep and helps constrain the dust cloud above the electrode.

In the experiments presented, an aluminum plate with a milled circular cutout 1 mm deep and 25.4 mm in diameter was employed to provide horizontal confinement for the dust (Fig. 4.3). MF dust particles were used having a mass density of 1.514 g/cm^3 and a diameter of $8.89 \pm 0.09 \text{ }\mu\text{m}$ as provided by the manufacturer. These particles were illuminated by a vertical sheet of laser light and their trajectories were recorded using a CCD camera running at 120 frames per second and having a resolution of 640×240 pixels. The plasma power was held constant at 1 W (13.56 MHz) throughout the experiment.

A dust dropper was used to drop single dust particles into the plasma sheath region where the falling dust particle collides with a second particle already located at the equilibrium point of the system. As part of the process of the newly formed two-particle

system reaching an equilibrium state, the falling dust particle exhibits underdamped oscillations in the vertical direction and damped motion in the horizontal direction. Examination of the vertical oscillations of the falling particle allows calculation of the drag coefficient due to dust-neutral gas collisions employing a standard resonance frequency method (Homann *et al* 1999) where, given the homogeneity of the system, it is assumed there is no significant difference between vertical and horizontal drag coefficients. The interaction between the two dust particles is measured directly, where the horizontal confining potential is quantitatively determined from the center of mass equations. Additionally, analysis of the direct particle-particle interaction allows determination of the interaction potential, providing both the charge and screening distance to be derived assuming a screened Coulomb potential structure. All of these are discussed in detail below.

4.5. Particle Motion in the Vertical Direction

As mentioned above upon introduction into the plasma, the falling dust particle initially undergoes damped oscillations in the vertical direction. These oscillations can be described as damped harmonic oscillations,

$$\ddot{z} + \beta\dot{z} + \omega_0^2 z = 0, \quad (4.1)$$

where β is the Epstein drag coefficient (Epstein 1924) due to the neutral drag force, ω_0 is the natural frequency of the vertical potential well, and z is the displacement of the particle's position from its equilibrium point. The amplitude of oscillation is given by the response function

$$R(\omega) = \frac{F_0}{\sqrt{(\omega_0^2 - \omega^2)^2 + \beta^2 \omega^2}}, \quad (4.2)$$

where F_0 is a constant and ω is the frequency of motion. Using the measured resonance curves, the Epstein drag coefficient can easily be determined by fitting the amplitude.

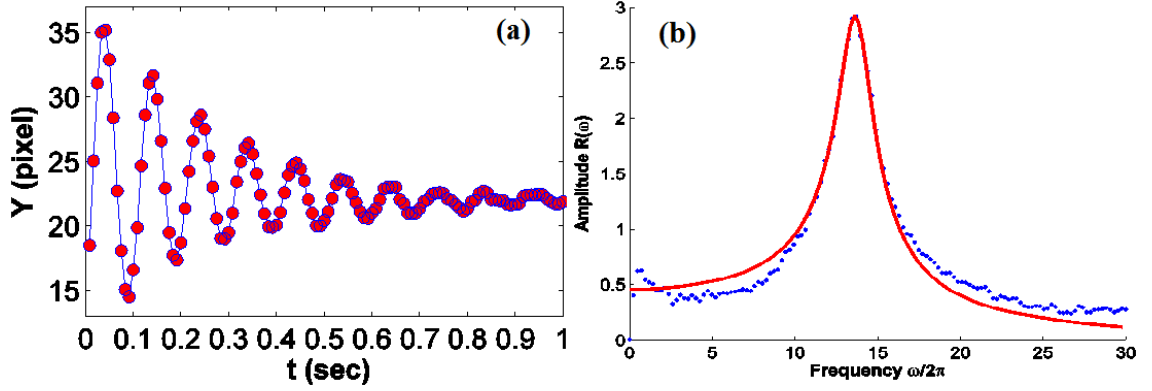


Fig. 4.4. (a) Representative data showing damped oscillations in the vertical direction for a single dust particle introduced into the plasma as described in the text ($P = 66$ mTorr). (b) Vertical resonance curves for the data shown in (a). As shown, the measured resonance frequency is 13.2 Hz where the dots denote the direct Fourier Transform of the experimental data with the solid line showing a fit to the amplitude using Eq. (4.2). This fit provides a drag coefficient $\beta = 13.4 \text{ s}^{-1}$. ($P = 66$ mTorr.)

Fig. 4.4 (a) shows a representative damped oscillation with Fig. 4.4 (b) showing the corresponding resonance curve and amplitude fit. As can be seen in Figs. 4.5 (a) and (b), the measured value for β increases linearly with increasing gas pressure, in good agreement with theoretical values obtained using the Epstein drag formula

$$\beta = \frac{8}{\pi} \frac{P}{\rho a v_{th,n}}, \quad (4.3)$$

where P is the gas pressure, ρ and a are the mass density and radius of the dust particle, and $v_{th,n}$ is the thermal velocity of the neutral gas. At higher pressures (> 80 mTorr), vertical oscillations are already complete before the particle enters the camera frame; this

results in the particle slowly approaching its equilibrium point from a horizontal direction without oscillation in either the vertical or horizontal direction. In this case, the drag coefficient is measured by first dropping a particle into the cell prior to ignition of the plasma. Once analysis of the particle's trajectory showed its velocity to be constant for a given pressure, the drag coefficient was calculated using the balance equation $G = m\beta v$, where m and v are the mass and velocity of the dust particle, respectively.

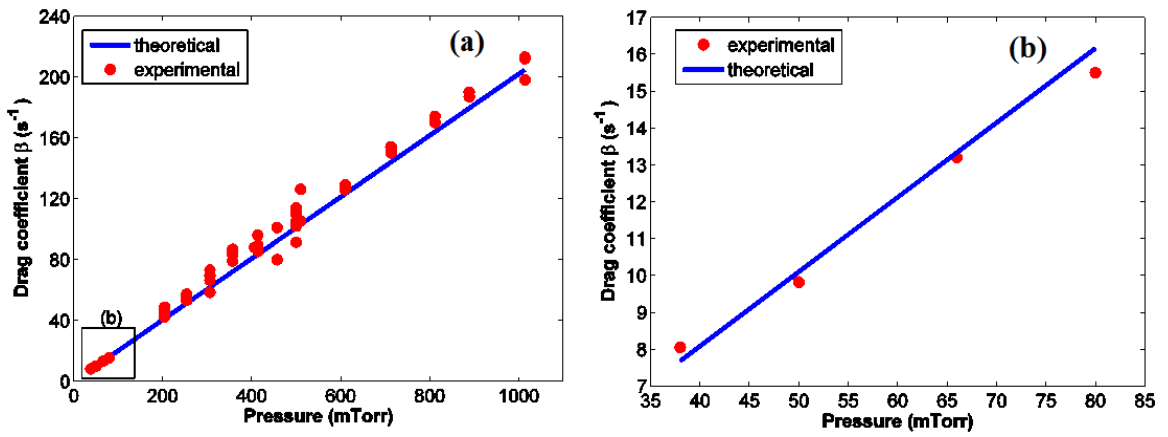


Fig. 4.5. (a) Representative data showing the measured drag coefficient for various gas pressures for a dust particle in a plasma. Dots represent experimental data, while solid lines denote theoretical values as obtained from Eq. (4.3). The data acquired across all pressure ranges examined is shown in (a) while data collected for pressures below 85 mTorr is shown in expanded form in (b).

4.6. Particle Motion in the Horizontal Direction

Particles within the CASPER GEC reference cell are confined horizontally by the horizontal component of the electric field created by the cutout in the plate placed on top of the powered bottom electrode. As mentioned earlier, a falling dust particle will undergo damped motion in the horizontal direction when interacting with the second particle via a screened Coulomb potential. Assuming the horizontal motion of the particle is along a straight line, and neglecting forces small compared to the electrostatic

forces involved (for example, the thermophoretic force or the radiation pressure force (Liu *et al* 2003)) the equation of motion in the horizontal direction for the i^{th} particle ($i = 1$ or 2) is given by

$$\ddot{X}_i + \beta \dot{X}_i + \frac{1}{m_i} \frac{dW_{conf}}{dX} \Big|_{X_i} = \frac{(-1)^{i+1}}{m_i} \frac{dW_{Inter}}{dX} \Big|_{|X_r|}, \quad (4.4)$$

where X_i is the distance from the equilibrium point for particle i , m_i is its mass, β is the Epstein drag coefficient, W_{conf} is the potential energy of the particle while in the confining region, W_{Inter} is the interaction potential energy between the two particles, and the separation distance between the particles is given by $X_r = X_i - X_j$. Assuming identical particles, their drag coefficients and masses will be the same. Summing over particles 1 and 2 yields a center of mass, $X_c = (X_1 + X_2)/2$, with corresponding equation of motion

$$\ddot{X}_c + \beta \dot{X}_c + \frac{1}{m} \frac{dW_{conf}}{dX} \Big|_{X_c} = 0. \quad (4.5)$$

The difference between these yields an equation for the relative motion of the two particles

$$\ddot{X}_r + \beta \dot{X}_r + \frac{2}{m} \frac{dW_{conf}}{dX} \Big|_{X_r} = \frac{2}{m} \frac{dW_{Inter}}{dX} \Big|_{|X_r|}, \quad (4.6)$$

where the confining potential is obtained through integration of Eq. (4.5)

$$W_{conf}(X_c(t_n)) = W_0 - \frac{m}{2} \dot{X}_c^2(t_n) - m\beta \int_{t_0}^{t_n} \dot{X}_c^2(t) dt. \quad (4.7)$$

Substituting the confining potential (4.7) into the equation of relative motion (4.6) and integrating, the particle interaction potential can be expressed as

$$W_{Inter}(X_r(t_n)) = W_{I0} - \frac{m}{4} \dot{X}_r^2(t_n) - W_{conf}(X_r(t_n)) - \frac{m\beta}{2} \int_{t_0}^{t_n} \dot{X}_r^2(t) dt. \quad (4.8)$$

In the above, W_0 and W_{10} are both offsets. Defining the confining potential energy to be zero at the equilibrium point and assuming the interaction potential vanishes at infinite separation distance, W_0 and W_{10} can be determined, yielding both the confining potential and the interaction potential.

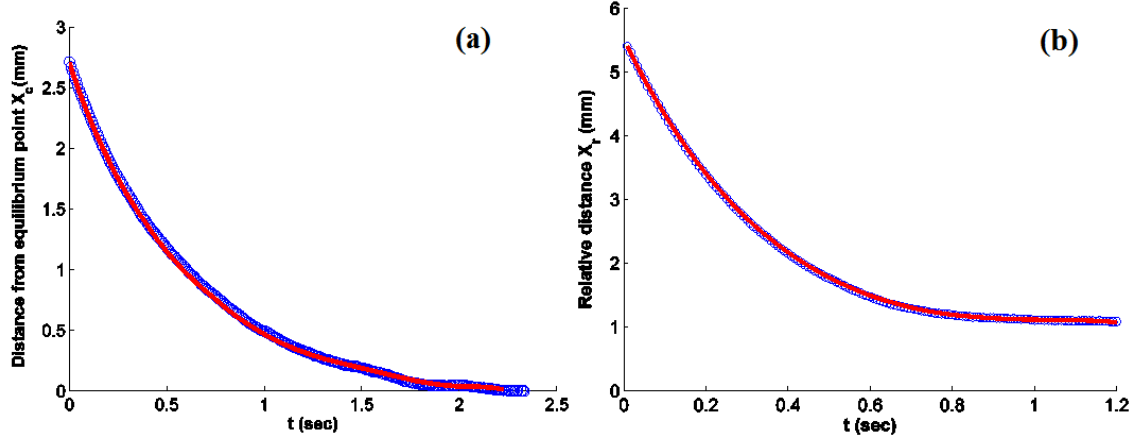


Fig. 4.6. (a) Center of mass distance from the equilibrium point as a function of time. The blue circles denote experimental data, while the red solid line shows a polynomial fit to $X_c(t)$. (b) Relative distance between particles as a function of time. Circles denote experimental data, while the sold line shows a polynomial fit to $X_r(t)$. ($P = 66$ mTorr)

In Eqs. (4.7) and (4.8), the majority of the uncertainty is associated with the measurement of the velocity (the first time derivative of position) and its associated time integral. To reduce this uncertainty, the time step was minimized using a camera frame rate of 120 Hz while the uncertainty in the velocity was minimized by fitting the center of mass equation (Fig. 4.6(a)) and the relative motion equation (Fig. 4.6 (b)) by polynomials in t

$$X(t) = a_0 + a_1t + a_2t^2 + a_3t^3 + a_4t^4 + \dots \quad (4.9)$$

Fig. 4.7 shows the calculated horizontal potential energy corresponding to the data shown above. As can be seen, the potential is well-described by a polynomial fit

using a parabolic function ($W_{conf}(X) = kX^2$) and these results are in good agreement with experimental data. Once the confining potential is determined, the interaction potential between the two particles can be easily found using Eq. (4.8) (Fig. 4.8). As seen, this interaction potential is well described by a screened Coulomb potential as expected. The particle charge and screening distance calculated from the experimental data and the polynomial fit are in good agreement, within the uncertainties described previously.

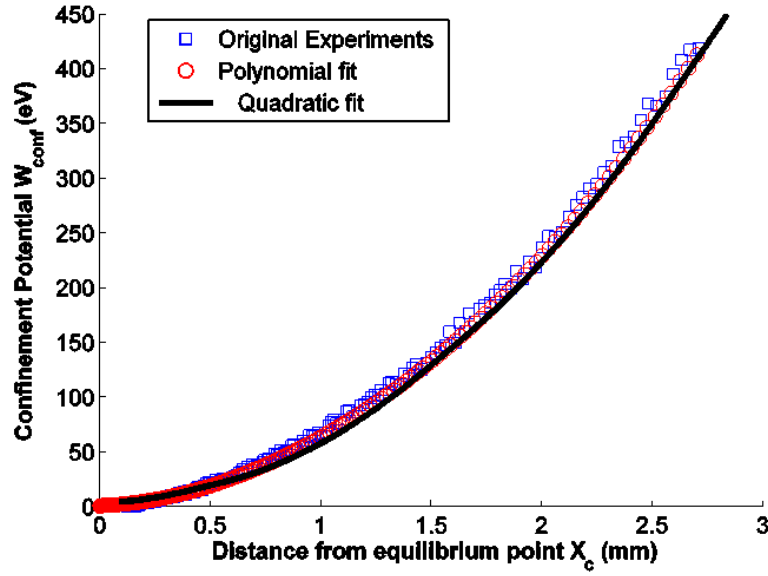


Fig. 4.7. Measured horizontal potential energy. Squares denote values calculated from experimental data, while the circles represent values calculated using a polynomial fit for $X_c(t)$. The solid (black) line shows a quadratic fit to the potential energy $W_{conf} = [52(X + 0.1)^2 - 0.4]$ eV where the resulting spring constant is $k = (8.33 \pm 0.18) \times 10^{-12}$ kg/s².

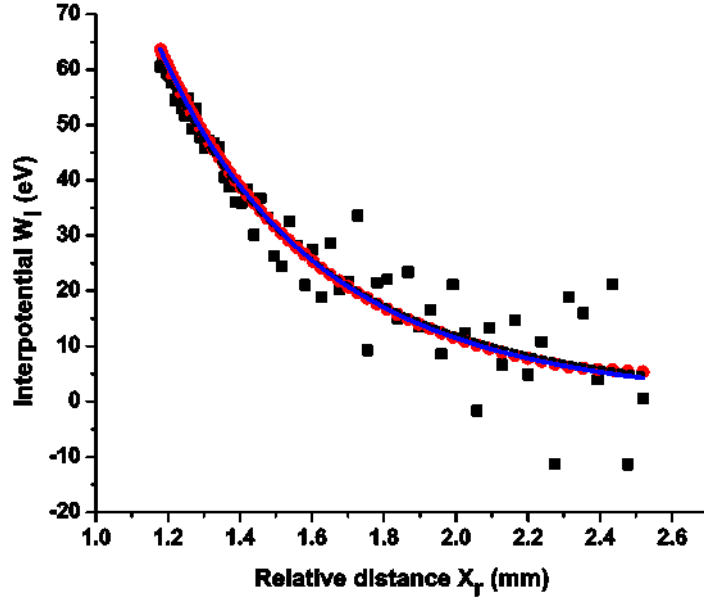


Fig. 4.8. Measured interaction potential energy as a function of particle separation. Squares represent values derived from the original experimental data while the dashed line shows the corresponding fit assuming a screened Coulomb potential. Using this fit, the calculated particle charge is $Q = (1.59 \pm 0.31) \times 10^4 e$ and calculated screening distance is $\lambda_{scr} = (729 \pm 192) \mu\text{m}$. The dots (red) denote results derived using a polynomial fit $X_r(t)$. The solid line shows the corresponding screened Coulomb potential fit, with $Q = (1.69 \pm 0.06) \times 10^4 e$ and $\lambda_{scr} = (692 \pm 17) \mu\text{m}$. ($P = 66$ mTorr)

4.7. Interaction Potential Relationship to Neutral Gas Pressure

The relationship between the interaction potential and the neutral gas pressure was also examined. As shown in Fig. 4.5, as the neutral gas pressure increases the drag force becomes stronger. This results in the center of mass motion changing from underdamped motion ($P \leq 38$ mTorr) to critically damped motion ($P \approx 50$ mTorr) and finally to overdamped motion ($P \geq 66$ mTorr). The corresponding spring constants for the potential well are shown in Fig. 4.9 (a). As shown, the spring constant is large across the under-damped regime, decreases sharply as the pressure increases to a critical point ($P \approx 50$ mTorr) where the motion becomes critically damped, and then increases to a maximum ($\approx 8.88 \times 10^{-12} \text{ kg/s}^2$) at a pressure of 80 mTorr. Beyond 80 mTorr, k

decreases in a uniform manner. Once the confining potential is determined, the interaction potential between the two particles can be calculated using Eq. (4.8). The data shown in Fig. 4.9 (b) denotes these results, employing polynomial fits to the measured data. As shown, the interaction potential decreases with increasing pressure. The resulting screening distance and particle charge calculated from the interaction potential at various pressures are shown in Figs. 4.10 (a) and (b) respectively. As can be seen, both decrease with increasing pressure.

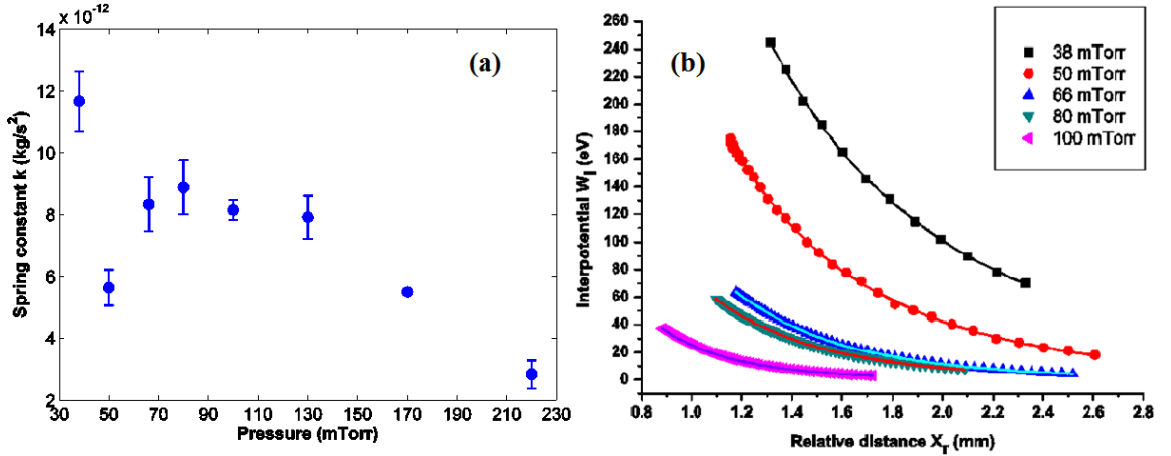


Fig. 4.9. (a) Spring constants for the potential well at various pressures. A maximum value of k occurs at around 80 mTorr, with a minimum occurring between 38 mTorr and 50 mTorr. (b) The interaction potential between two particles at various separations and pressures. Symbols represent results from a polynomial fit as described in the text, while solid lines show a screened Coulomb potential fit.

Assuming a weakly collisional regime, the net electron and ion current to the dust particle's surface can be expressed by

$$I_e = \sqrt{8\pi} a^2 n_e v_{Te} \exp(-z), \quad (4.10)$$

and,

$$I_i = \sqrt{8\pi} a^2 n_i v_{Ti} \left[1 + z\tau + 0.1z^2\tau^2(\lambda/l_i) \right], \quad (4.11)$$

respectively (see Section 2.5). For an equilibrium state and assuming the ion and neutral gas temperatures are approximately $T_i \approx T_n \approx 0.03$ eV at room temperature, the particle charge can be calculated by equating the ion and electron current $I_e = I_i$. These results are shown in Fig. 4.10 (a). Fig. 4.11 shows the relationship between the normalized particle charge number and the ion collisionality index, both theoretically and experimentally.

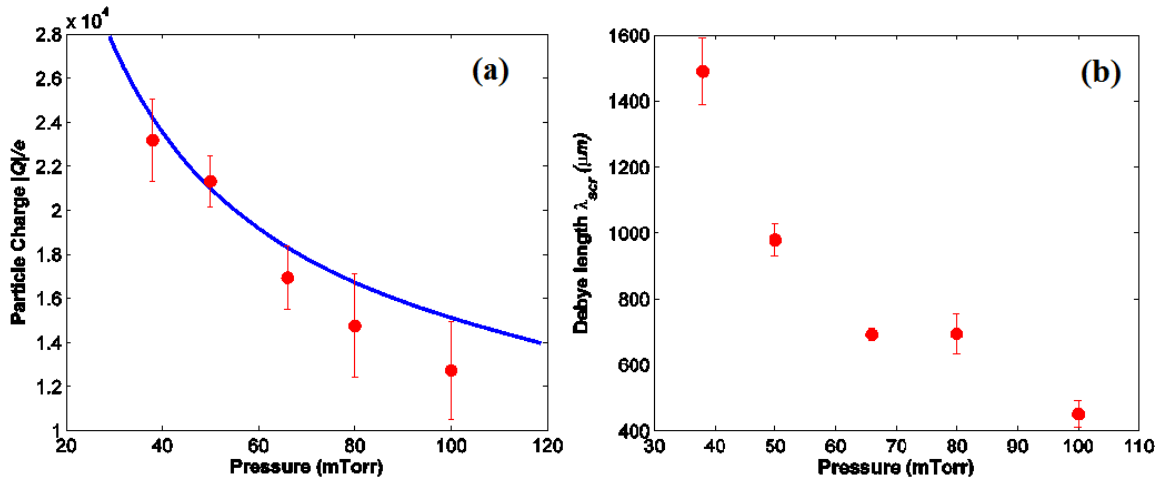


Fig. 4.10. (a) Dust particle charge as a function of pressure. Dots denote experimental data while the solid line is generated theoretically as described in the text. (b) Dust screening distance as a function of pressure. The dust screening length decreases with increasing pressure as explained in the text.

The above results can be explained by considering the increased ion-neutral collision rate as the pressure increases. Ratynskaia *et al* (Ratynskaia *et al* 2004) concluded that, as this collision rate increases, the momentum of the ions is more easily transferred to the neutral gas resulting in slower moving ions. This results in more ions being captured by the negative dust grains. At the same time, the increasing pressure lowers the overall electron temperature resulting in a decreasing probability of electron-dust collisions. When combined, these reduce the overall negative charge on the dust.

Additionally, the increased ion-neutral collision rate and the lessened negative charge on the dust particle increases the local ion density in the vicinity of the dust particle, in turn increasing the shielding strength (Khrapak *et al* 2005). Thus, the screening distance is also reduced (Fig. 4.10 (b)). Where these trends have been predicted theoretically, the results are in good agreement with the experimental measurements shown in Fig. 4.10 (a) and Fig. 4.11.

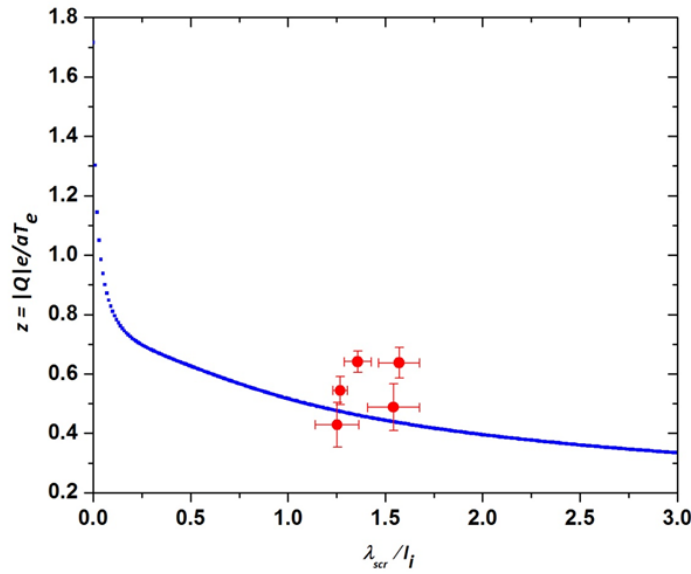


Fig. 4.11. The normalized particle charge number $z = |Q|e/aT_e$ as a function of the ion collisionality index λ_{scr} / l_i . The smaller dots correspond to the data produced by theoretical calculation using Eqs. (4.10) and (4.11), while the bigger dots (red) come from these experimental results. The ion temperature, T_i , is assumed to be 0.03 eV while the electron temperature is, $T_e = 9.48 + 14.69 \times \exp(-P/20.39)$ (eV) over the considered pressure range, where p is the gas pressure in unit of mTorr. The uncertainty of the probe measurements is not included here.

The results in this paper are also close to recent data from Vaulina and Lisin (Vaulina *et al* 2009; Vaulina and Lisin 2009). They determined interaction forces between the particles in non-ideal dissipative systems with isotropic pair potentials. Their technique was based on the solving of the inverse Langevin problem and allowed

taking into account the friction factors and the parameters of external retaining forces. The inverse problem was solved by the best fitting between the solution of a direct problem on movement of particles and the information on coordinates and displacement of these particles. Their theory was tested numerically in a wide range of the parameters typical for dusty plasma experiments. The compatibility of results presented in this dissertation and those from Vaulina and Lisin's theory is important, since both techniques do not need any prior assumptions or to perturb the analyzed systems.

Additionally, it must be noticed that the previous work (Ratynskaia *et al* 2004; Khrapak *et al* 2005) investigating relationship between dust particle charge and discharge gas pressure were done in DC discharge. As far as the authors know, this is the first experimental verification of this effect in an RF plasma under gravity. The reasonable fits in Fig. 4.10 (a) and Fig. 4.11 suggest that, as what have been found in DC discharge, the charge on a particle in the sheath of an RF plasma also decreases with increasing pressure, in agreement with theoretical predictions.

4.8. Conclusions

In this Chapter, a simple method has been developed and described which allows simultaneous measurement of the confining potential well and the interaction potential for two particles in a dusty plasma. In contrast with previous work, no external perturbation (laser, probes, slot, etc.) to the system is required. This method also is advantageous in that it does not require any *a priori* assumptions for the analysis. For example, this method involves only a two-particle system; thus it doesn't rely on the assumption of a finite dust density and is not impacted by closely packed grains (Hebner *et al* 2001; Quinn and Goree 2002). Other experiments have used a wave method in

particle flow to detect the particle charge, which requires an assumption of a linear dispersion relation (Ratynskaia *et al* 2004; Nunomura *et al* 2002).

Employing the technique described in Section 4.4, the confining potential well was confirmed to be parabolic (Figs. 4.7 and 4.9 (a)) and the interaction potential was shown to be a screened Coulomb potential over a wide range of pressures and separation distances from equilibrium (Figs. 4.8 and 4.9 (b)). It was also shown that both the particle charge and the screening distance are dependent upon the neutral gas pressure, where both decrease with increasing pressure (Figs. 4.10 (a) and 4.(b)) as predicted by theory. The increasing neutral gas pressure enhances the neutral-ion collision rate draining momentum from the ions; this results in ions with lower momentum(s) which are more easily captured by negatively charged dust grains. This has been shown experimentally within a DC plasma under microgravity conditions using the Plasma Kristall-4 (PK-4) facility on the international space station (Ratynskaia *et al* 2004; Khrapak *et al* 2005a; Lampe *et al* 2003) but this is the first time it has been shown experimentally within RF plasma under gravity. At the same time, the average electron temperature is lowered by increasing the pressure, leading to a reduced chance of electron-dust collisions. Both of these two effects reduce the net charge on the dust grains. At the same time, the density of ions are in the vicinity of the dust grains increases due to the smaller charge on the grains and increased ion-neutral collisions, resulting in the decrease of the screening distance (Khrapak *et al* 2005a). In deriving Eq. (4.11), Khrapak *et al* (Khrapak *et al* 2005a) and Lampe *et al* (Lampe *et al* 2003) assumed no plasma species flow, i.e., dust grains immersed in the bulk plasma which usually occurs in DC discharge or under microgravity. However, the experimental results

above show that the expression for ion current to the grain surface (Eq. (4.11)) can be extended to the case including ion flow in the sheath region under gravity.

With the knowledge of particle-particle interaction of two single particles, it is natural to think that what will happen if there is a large number of dust particles in the system. Previous investigators have found the dust crystalline structures (Thomas H *et al* 1994) in RF discharge and dust waves in DC and RF discharges (Barkan *et al* 1995; Thompson *et al* 1997; Khrapak *et al* 2005a) when dense particles present in the discharge region. In particular, in RF discharge just like the ones in the experiments discussed in this Chapter, the horizontal confinement provided by the cutout on the low electrode was always much smaller than the vertical confinement generated by the gravitational and electric forces. Then, how about increasing the horizontal confinement to be the same order of the one in vertical direction? Next Chapter will present experiments in which a glass box creating strong horizontal confinement is placed on top of lower electrode instead of milled cutout and a large number of dust particles reside inside the glass box.

CHAPTER FIVE

Oscillation and Instability in Glass Box Confinement

Parts of this chapter have been published as: “One-dimensional vertical dust strings in a glass box”, J. Kong, T. Hyde, L. Matthews, K. Qiao, Z. Zhang and A. Douglass, *Phys. Rev. E* 84, 016411 (2011).

5.1. Introduction

In order to constrain dust particles in the sheath above the lower electrode, horizontal confinement is required in order to provide a radially-directed inward force on the particles that balances the dust particle repulsive interaction. Usually, this horizontal confinement is much smaller than the gravitational or electric force acting on the particles, allowing nearly flat two dimensional (2-D) crystals to be formed (Melzer *et al* 1994; Trottenberg *et al* 1995). To increase the horizontal confinement, in this work, glass boxes were employed to constrain the dust particles. In this Chapter, an investigation into dust behavior inside varying size glass boxes will be presented and an examination of the resulting transition between 1-D dust strings and 3-D dust clusters discussed. The oscillation spectrum of a 1-D vertical dust string in a small glass box will also be shown, followed by several 3-D dust acoustic wave instabilities that were observed in a larger glass box. A simple diagnostic for determining the electric field inside the glass box, employing only a single dust particle will also be introduced.

5.2. Applications of Glass Boxes in Dusty Plasmas

One of the earliest applications of a glass box in a dusty plasma involved the creation of a homogenous 3-D dust “Coulomb ball” (Arp *et al* 2004). To study the properties of an isotropic 3-D dusty plasma, experiments must either be conducted undermicrogravity conditions (Morfill *et al* 1999) or employ thermophoretic levitation (Rothermel *et al* 2002) to compensate for the gravitational force. Both of these methods have recently been used to examine extended 3-D dusty plasma systems. Unfortunately, the majority of investigations into such 3-D compact dust crystals using these methods has been hampered by the formation of dust-free regions, called “voids”, at the center of the discharge. Thus, all observations to date show a significant influence of the trapping mechanism (i.e., confinement potential) on the structure of the confined dust cloud.

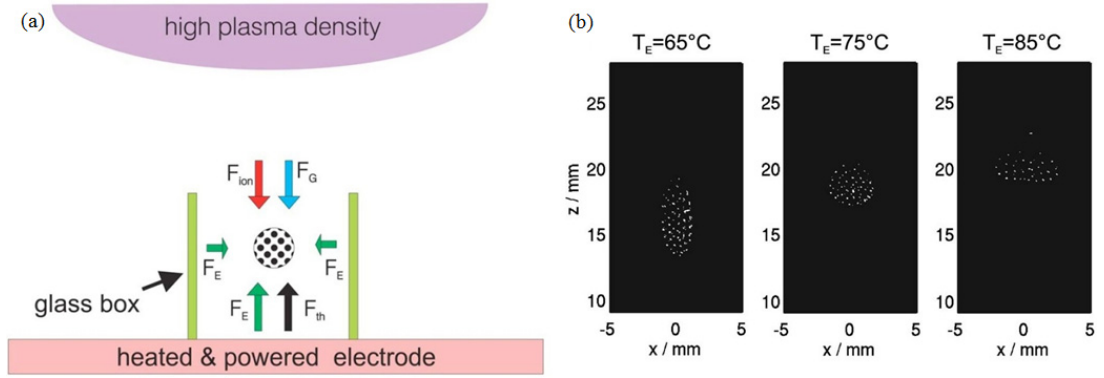


FIG. 5.1. (a) The superposition of the gravitational \vec{F}_g , thermophoretic \vec{F}_g , electric \vec{F}_g , and ion drag forces \vec{F}_g yield a stable confinement of the Coulomb ball inside the glass box. (b) Vertical sections through the center of a trapped Coulomb ball at different electrode temperature T_{el} (Arp *et al* 2005.)

The introduction of a glass box and thermophoresis to dusty plasma experimental systems allowed, for the first time, large Coulomb balls containing up to a few thousand particles to be observed without voids or particle chains in a ground-based laboratory RF

discharge environment (Arp *et al* 2004, 2005). A cubical glass box, with a side length of 30 mm and an open top and bottom, was placed at the center of the powered electrode, which was also designed in such a manner that it could be heated or cooled in order to create a temperature gradient between the electrodes, producing a thermophoretic force on the dust particles. Figure 5.1 (a) shows the experimental setup involved and the forces acting on the dust cloud that produced the crystal structures shown in Fig. 5.1 (b). It was observed that the shape of the trapped Coulomb balls changed from prolate to oblate with increasing electrode temperature.

Glass boxes are now widely employed as a trapping mechanism in dusty plasma research. The variety of glass boxes provides an easy opportunity to examine the properties of dust structures.

5.3. 1-D Vertical Dust Strings in a Glass Box

One-dimensional systems are of great interest in both theoretical physics and applied engineering research (Hone *et al* 1999; Lepria *et al* 2005). In engineering research, much of nanoscale technology (for example, the production of quantum wires and/or carbon nanotubes), can be related to a one-dimensional system. Dusty plasmas provide a controllable environment that can easily be used to simulate such systems. For example, low dimensional transport and transition phenomena (e.g., thermal conductivity, wave propagation, and phase transitions) are all easily produced and controlled within a dusty plasma environment due to its rapid response time as compared to a colloidal system and the fact that a dusty plasma can be easily imaged, unlike atomic systems.

Theoretically, one-dimensional dust strings have been investigated by several authors (Sato *et al* 2001; Liu and Goree 2005; Sheridan 2009). However, to date,

controllable one-dimensional dust strings have not been extensively examined experimentally due to the difficulty of forming them in a complex plasma, especially in the vertical direction (Homann *et al* 1997). In this section, a technique is provided for generating a one-dimensional vertical dust string at the center of a glass box placed on the lower electrode of a CASPER GEC RF reference cell. Once in place, this one-dimensional string is levitated above the lower electrode but still inside the glass box and its oscillation spectra examined through modulation of an external DC bias applied to the lower electrode.

5.3.1. Formation of a Single Vertical Dust String

In the experiments presented here, MF dust particles of $8.89 \pm 0.09 \mu\text{m}$ diameter were used. A glass box 1.27 cm in height, 1.07 cm in internal side length and 2 mm in thickness was employed to provide the horizontal confinement. The top and bottom of the glass box was left open, as described in Section 3.3. In order to form a single vertical dust string, the RF power was initially established at 5 W, at a gas pressure of 172 mTorr. Under the parameters described, dust particles introduced into the system form a turbulent cloud located near the upper edge of the box. Slowly lowering the RF power to approximately 1.35 W cause this turbulent dust cloud to pass through a filamentary state (Fortov *et al* 2000a) before forming a single long vertical string located at the center of the glass box (see Fig. 5.2). The total number of particles within this 1-D string has to date been always observed to be between 10 and 20. Upon examination, it was determined that the transition from a turbulent state to a 1-D vertical string was reversible; returning the RF power to its original value caused the 1-D string to transition back through the filamentary state to the turbulent state. Finally, continually lowering the RF

power caused the dust particles to fall to the lower electrode, starting with the particles closest to the electrode.

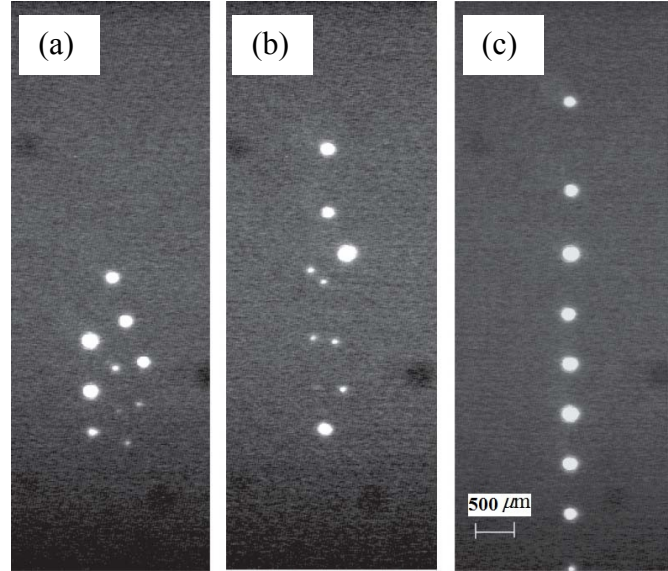


FIG. 5.2. Transition from filamentary state to a single vertical string by varying the RF power. In the figure above, the RF power decreases from (a) to (c).

5.3.2. Interaction of the Glass Box with 1-D Dust String

As mentioned above, lowering the RF power creates a structural transition in the dust particle system from 3-D to 1-D, but only when the particles are confined within a glass box, indicating that the horizontal confinement increases as the RF power decreases. This can best be explained by the fact that lowering the RF power decreases the ionization rate, increasing the screening length. Since, in this case, horizontal confinement is due to the surface charge on the glass box (Basner *et al* 2009), the Yukawa force exerted on the dust particles by each of the glass panes increases as the screening length increases, increasing the overall horizontal confinement. Due to symmetry, this results in the overall horizontal confinement canceling at the center of the box, creating an ideal environment for one-dimensional vertical string formation.

5.3.3. Oscillation of a 1-D Dust String

Using the technique described above, a 1-D vertical dust string consisting of sixteen particles was assembled within the box. Once stable, it was perturbed employing a low frequency (1–20 Hz) sine wave produced by a modulated DC bias applied to the lower electrode (see Section 3.5). All input modulation amplitudes were attenuated in order to avoid the possibility of nonlinear dust-particle oscillations. The particles were illuminated using a vertically fanned laser sheet and system data were captured employing a side-mounted CCD camera running at 60 fps. The total camera field of view is 512×512 pixels with a pixel size corresponding to $22.99 \pm 0.21 \mu\text{m}$. The average interparticle spacing is around $418 \mu\text{m}$. The resulting resonance spectra including oscillation amplitude, resonance frequency and wave number were examined.

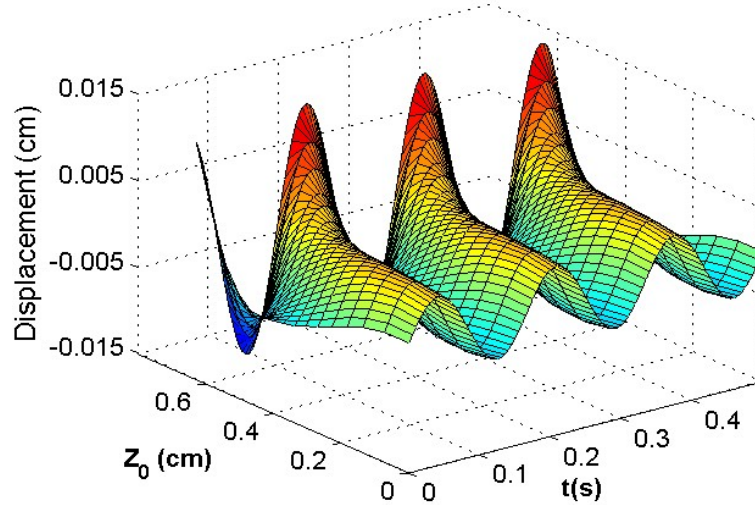


FIG. 5.3. Construction of propagating waves traveling within a dust string consisting of 16 particles, generated by driving frequencies of 6 Hz. Z_0 represents the equilibrium position of each particle in the string, where the particle farthest from the lower electrode (P1) is defined as zero.

Figure 5.3 shows 3-D constructions of the propagating wave fronts traveling within a vertical dust string consisting of 16 particles inside a glass box in a dusty plasma,

resulting from driving frequencies of 6 Hz. In this figure, the z -direction is defined as the vertical direction, with the origin starting at the top edge of the camera field of view and pointing downwards. Throughout the following discussion, particles are numbered P1 through P16, with P1 being the particle farthest away from lower electrode, i.e., the particle at the top of the string.

5.3.4. Motion of Individual Particles

Under external perturbation and considering only the vertical direction, the motion of the particles described is given by Newton's law

$$m \partial^2 z / \partial t^2 + m \beta \partial z / \partial t + EQ - mg = F_0 \sin(\omega t + \phi). \quad (5.1)$$

Assuming only small perturbations and employing a Fourier transformation, the oscillation amplitude and phase for each particle are obtained as

$$A(\omega) = \frac{A_0}{\sqrt{(\omega^2 - \omega_0^2)^2 + \beta^2 \omega^2}}, \quad (5.2)$$

and

$$\tan(\phi) = \frac{\beta \omega}{\omega_0^2 - \omega^2}, \quad (5.3)$$

where A_0 is a constant determined by the amplitude of the external perturbation, ϕ represents the particle's oscillation phase angle, and ω_0 is the natural frequency.

Figure 5.4 (a) shows representative oscillation spectra for the string. A series of resonance peaks for each particle can be seen. Additional data (0.5 Hz frequency step) was collected around each oscillation peak, in order to reduce the overall experimental uncertainty. By fitting the experimental oscillation amplitude using Eq. (5.2), the parameters A_0 , ω_0 , and β can be easily extracted. As a representative example, the

experimental oscillation spectrum for a single particle (P6) along with a corresponding theoretical curve fit is shown in Fig. 5.4 (b). The fit shown yields an amplitude $A_0 = 2073 \pm 289$, a resonance frequency $\omega_0/2\pi = (6.69 \pm 0.26)$ Hz, and a damping coefficient $\beta = 34.19 \pm 4.24 \text{ s}^{-1}$.

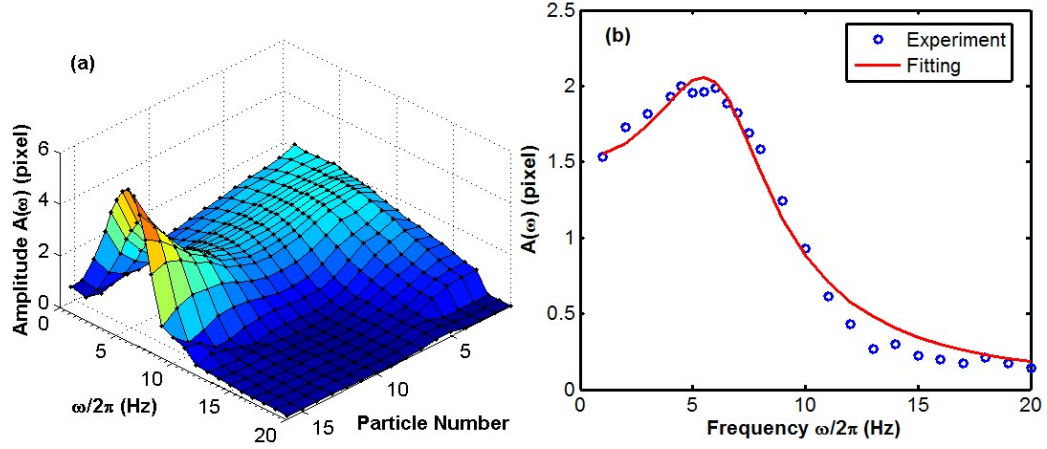


FIG. 5.4. (a) Representative oscillation spectra for a vertical dust string consisting of sixteen particles. (b) Oscillation spectrum for a single particle (P6) and a theoretical fit (see Eq. (5.2)) resulting in values for the amplitude of $A_0 = 2073 \pm 289$, resonance frequency $\omega_0/2\pi = (6.69 \pm 0.26)$ Hz, and damping coefficient $\beta = 34.19 \pm 4.24 \text{ s}^{-1}$.

5.3.5. Fitting Parameters Distribution

The parameters, i.e., A_0 , ω_0 , and β , are different for each particle in the string, as shown respectively in Fig. 5.5. It can be easily seen that the oscillation amplitude A_0 , resonance frequency ω_0 , and drag coefficient β decrease linearly as the particle number increases, i.e., for particles approaching the lower electrode, P1 to P5. At the same time, the parameters for particles P6-P16 in the string remain relatively constant with only small deviations across the ranges considered ($A_0 \approx 2200$, $\beta \sim 18\text{-}35 \text{ s}^{-1}$, $\omega_0/2\pi \sim 6\text{-}7$ Hz). It should be mentioned that particles P1-P5 comprise a separate group and as such, are not included in the current analysis. The principles governing the special behavior of these five particles will be discussed in Section 5.3.7.

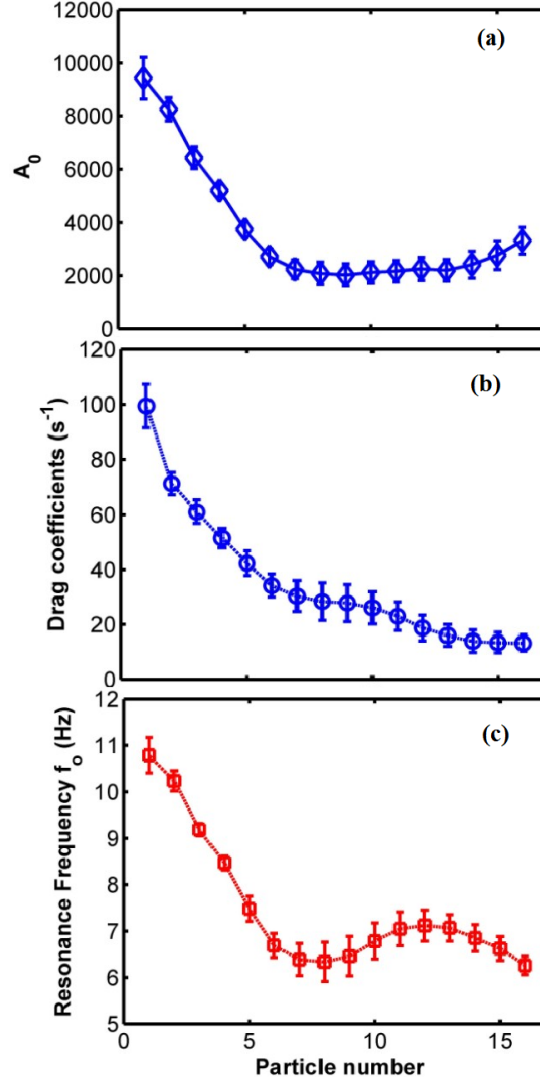


FIG. 5.5. Distribution of the oscillation parameters discussed in the text for each particle in the string: (a) amplitude A_0 , (b) drag coefficient β , and (c) resonance frequency $f_0 = \omega_0 / 2\pi$.

Once the drag coefficient and the resonance frequency have been determined, the oscillation phase for each particle in the string can be obtained using Eq. (5.3). (Note that the phase is measured with respect to the phase of the particle P1.) Figure 5.6 shows a plot of the relative oscillation phase distribution for each particle in the string at varying driving frequencies. As the driving frequency increases, the phase distribution becomes more linear within the particle string especially for P6-P16.

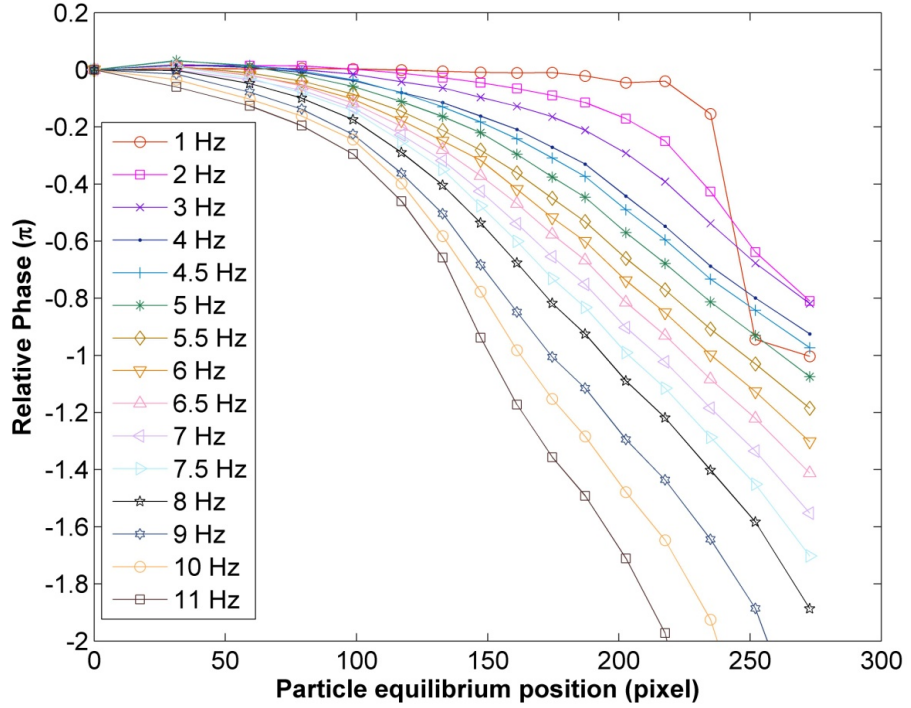


FIG. 5.6. The relative oscillation phase distribution within a string for different driving frequencies. The position of P1 is set to be origin, and the direction of downward to the lower electrode is positive.

5.3.6. Dispersion Relation

In order to obtain a linear dispersion relationship for the vertical oscillations of the particles in the string, we first analyzed the bottom particles P6-P16. As shown in section 5.3.5, particles P6-P16 construct a group in which particles have relatively uniform oscillation amplitudes, resonance frequencies and drag coefficients; thus it is reasonable to believe that these particles should have similar fundamental properties, such as charge and screening length. In Fig. 5.7 (a), a plot showing representative experimental data for the phase distribution within the string oscillated at $\omega/2\pi = 7.5$ Hz is shown and a linear fit is extrapolated to obtain the wave number k . The measured dispersion relation for this case is displayed in Fig. 5.7 (b).

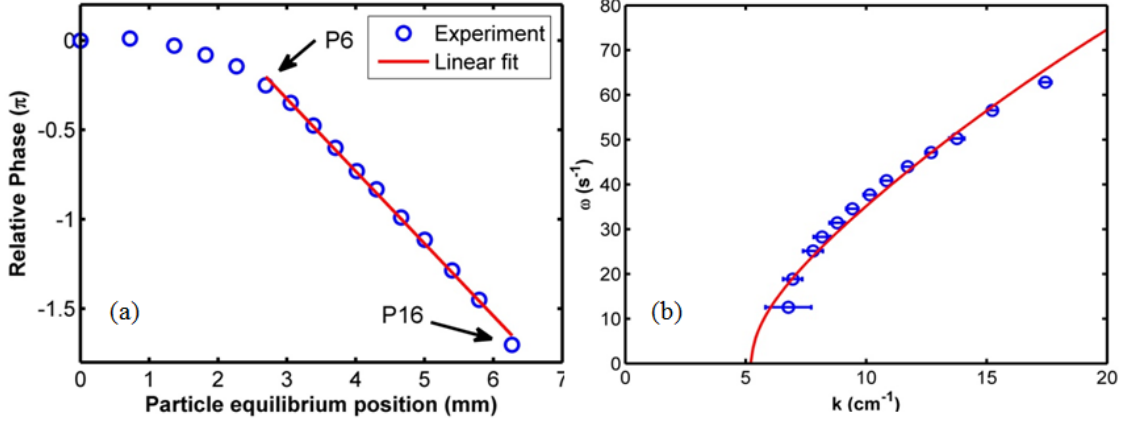


FIG. 5.7. (a) Linear fit to obtain the wave number for the dust string oscillated at $\omega/2\pi = 7.5$ Hz. (b) Dispersion relationship for dust particles P6-P16. Circles denote experimental data while the red solid line represents a theoretical fit to that data. The resulting cutoff wave number ($\omega = 0$) is $k_{cutoff} = 5.2 \pm 1.7 \text{ cm}^{-1}$.

The approach presented in Chapter Two for a DLW is employed here in order to obtain a simple theoretical prediction for the wave propagating within the dust string. In this case, the equation of motion in the vertical direction for each particle can be rewritten as

$$m_d \left(\frac{\partial^2 z_i}{\partial t^2} + \nu_{dn} \frac{\partial z_i}{\partial t} \right) = mg - E(z_i)q(z_i) - \sum_i \frac{\partial U_{ij}}{\partial z}. \quad (5.4)$$

Assuming only small perturbations, a Yukawa interaction, and neglecting any ion wakefield effect, and by only considering nearest neighbor particles, Eq. (5.4) becomes

$$\omega^2 + i\omega\nu_{dn} = -\frac{\gamma}{m_d} + \frac{2q_d^2}{4\pi\epsilon_0 m_d a^3} \left(1 + \frac{a}{\lambda_D} + \frac{a^2}{2\lambda_D^2} \right) \exp\left(-\frac{a}{\lambda_D}\right) \sin^2\left(\frac{ka}{2}\right), \quad (5.5)$$

where $\gamma = q dE/dz + E dq/dz$, which can be determined by the particle's charge and the local electric field. The electric field E includes contributions from both the glass walls and the lower electrode. Using Eq. (5.5), the theoretical dispersion relationship can be calculated with these results shown in Fig. 5.7 (b). In this case, the cutoff wave number

is $k_{cutoff} = 5.2 \pm 1.7 \text{ cm}^{-1}$ ($\omega = 0$) and is a consequence of the confining boundaries γ where $\gamma / m_d = 407 \pm 190$ (Nosenko *et al* 2009). Substituting the values for $k_{cutoff}(\omega = 0)$ and $\gamma / m_d(\omega = 0)$ into Eq. (5.5), using the average particle interspacing $a = 357 \mu\text{m}$ measured, estimating $\lambda_D \sim a$ (typical value in experiments) gives an approximate particle charge of $q_d = 3.4 \times 10^4 e$.

5.3.7. Discussion

Based on the measured oscillation spectrum shown in Fig. 5.5, it is easily seen that particles P1-P5 (the particles located closest to the top edge of the glass box) form a group (the “upper group”) separated from the group consisting of the lower particles P6-P16 in the string (the “lower group”). As shown, the particle oscillation amplitudes, resonance frequencies and drag coefficients decrease as P1-P5 get closer to the lower electrode but remain almost constant (within small fluctuations) for particles within the lower group (P6-P16). This phenomenon may be a consequence of one of several factors or some combinations of them. One possibility is the ion wakefield effect, which will be discussed here.

Due to symmetry, it is reasonable to assume the ion flow in the region close to the top of the glass box is directly downwards along the dust chain axis. Thus, particles located closest to the top edge of the glass box will be subject to the ion streaming, and positive charge regions should form below them. This positive charge region will contribute an equivalent electric field E_{ion} , reducing the total electric field, and lowering the resonance frequency. Since the ion wakefield only affects downstream particles, the resonance frequency for a lower particle will be smaller than that of the particle above. Thus, lower particles in the string will exhibit smaller resonance frequencies (P1-P5) (Fig.

5.5c). However, deeper into the glass box, the ion flow becomes less according to simulations done by Arp *et al* (Arp *et al* 2005). As a consequence, in this region the contribution from ion streaming becomes negligible compared to that of the lower electrode and the walls of glass box. In this case, particles located deeper in the glass box are negligibly affected by the ion flow and exhibit the same oscillation spectra (P6-P16). In the dust string observed in our experiments, this critical transition region appears to occur between P5 and P6.

5.3.8. Section 5.3 Summary

In this section, a mechanism for forming vertical, one-dimensional dust particle strings inside a glass box placed on the lower powered electrode of a plasma discharge device has been described. The dynamic properties of the vertical string have been studied by examining the oscillation spectra produced through modulation of the lower electrode DC bias for one-dimensional strings of various lengths. The resulting particle oscillation amplitudes, resonance frequencies, damping coefficients and oscillation phase differences were compared. The wave properties of these vertical strings have also been examined. Results show that these oscillation parameters are different for particles located at different positions. Although this effect is not yet completely understood, it may be related to the interaction between the ion wakefield and the contribution from the glass box.

5.4. Dust Acoustic Waves and Instabilities inside a Glass Box

In the section above, particles extended chain structures were produced inside a small glass box located on top of a powered electrode and the resulting oscillation

spectra and waves properties investigated. In this section, a larger number of dust particles will be introduced into a larger glass box having dimensions $(2.34 \text{ cm})^2 \times 2.54 \text{ cm}$ placed on top of the lower powered electrode and examined.

Table 5.1. Experimental observations of DAWs

Reporters	Discharge	Frequency (Hz)	Phase velocity (cm/s)
Barkan <i>et al</i> 1995	Q-machine	15	9
Thompson <i>et al</i> 1997; Merlino <i>et al</i> 1998	DC	6–30	12
Molotkov <i>et al</i> 1999; Fortov <i>et al</i> 2000b	DC	60	1
Pramanik <i>et al</i> 2003	DC	10	4.5
Williams <i>et al</i> 2008	DC	8-27	10
Thomas E <i>et al</i> 2007	DC	47	2
Chu <i>et al</i> 1994	RF magnetron	12	-
Zobnin <i>et al</i> 2002 Fortov <i>et al</i> 2003	Inductive RF	25-60	-
Trottenberg <i>et al</i> 2006	Capacitive and Magnetized RF	19-29	6-13
Schwabe <i>et al</i> 2007	Capacitive RF microgravity	3.3	5.6
Piel <i>et al</i> 2006	Capacitive RF microgravity	10	1.6
Khrapak <i>et al</i> 2003a	Capacitive RF microgravity	21-63	0.8
Yaroshenko <i>et al</i> 2004	Capacitive RF microgravity	8-40	-

5.4.1. Laboratory Observations of Dust Acoustic Waves

The DAW was first theoretically predicted for a weakly coupled collisionless dusty plasma in 1990 (Rao *et al* 1990). The first experimental observation of a DAW was reported by Chu *et al* (Chu *et al* 1994) in an RF magnetron discharge at a frequency $\cong 12$ Hz. Since then, numerous experiments have been conducted studying the properties of DAWs under various conditions. Representative experimental observations of DAWs are provided in Table 5.1. As shown, the frequency of a DAW is generally in the range of tens of Hz producing phase velocities on the order of cm/s.

One convenient way to investigate the properties of such DAWs in more detail is to apply a sinusoidal voltage modulation to either the anode or electrode. Synchronization between the applied voltage modulation and the DAW yields a wider frequency range of a DAW. A typical dispersion relationship obtained by employing such a signal synchronization approach is displayed in Fig. 2.18.

More recently, attention has been directed toward the formation of DAWs in capacitively coupled RF plasmas under gravity. To date, only a few experimental observations have been reported (Liao *et al* 2008; Teng *et al* 2009; Flanagan and Goree 2010; 2011). In Liao *et al* and Teng *et al*'s experiments, a hollow coaxial cylindrical trap with a 3-cm inner diameter and 14-mm in height was placed on the bottom electrode to confine a dusty plasma composed of $5\text{ }\mu\text{m}$ diameter polystyrene particles. Self-excited waves were observed at a background pressure of 170 mTorr when the discharge RF power increased from 2 W to 2.4 W at a frequency of 14 MHz. In Flanagan and Goree's experiments (Flanagan and Goree 2010; 2011), dust particles

were trapped in the plasma within a glass box having dimensions of $3\text{ cm} \times 3\text{ cm} \times 3\text{ cm}$ with both top and bottom open and placed on the lower electrode. Growth of the DAW was observed in the dust cloud as the gas pressure was slowly decreased from 420 mTorr to 404 mTorr.

In the CASPER GEC RF reference cells, a capacitively coupled RF plasma is generated in the space between the two electrodes as described in Chapter Three. An open glass box having dimensions of $(2.34\text{ cm})^2 \times 2.54\text{ cm}$ is placed on top of the lower electrode. A large number of dust particles ($10^4 - 10^5$) are then dropped into the glass box. Under these conditions, self-excited DAWs can be created by either decreasing the gas pressure or increasing the discharge power. In general, particles are more sensitive to changes in the discharge power than they are to changes in the gas pressure; thus, changing the discharge power is employed here to generate the DAWs. Fig. 5.8 shows the generation of self-excited DAWs inside the glass box described by increasing the discharge power at a gas pressure of 350 mTorr. During the initial stage of this process, the dust cloud remains stable due to strong neutral gas damping and weak ion flow (at 2W). As the discharge power increases, the ion flow instability becomes stronger, eventually overcoming the effect of the gas damping, resulting in the generation of DAWs ($> 3.10\text{ W}$). The threshold power for creating such DAWs at various pressures is shown in Fig. 5.9. The region to the right side of the blue line represents power and pressure conditions under which DAWs are generated, while the region to the left of the blue line denotes conditions under which the dust cloud remains stable.

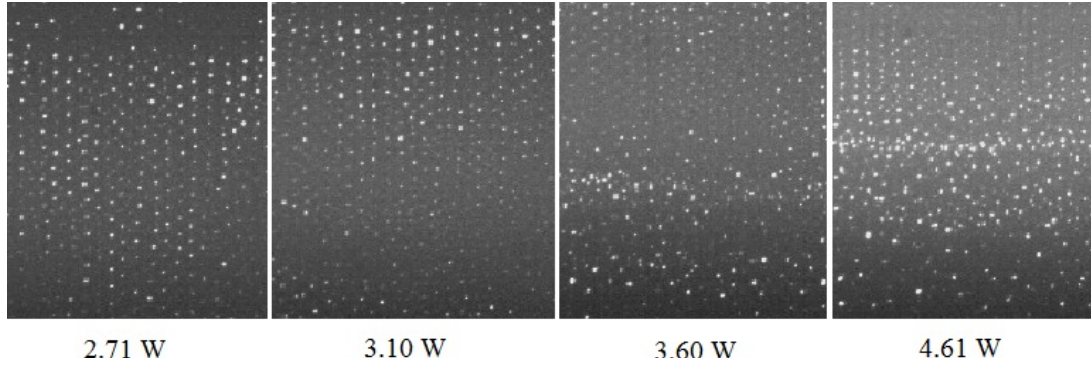


Fig. 5.8. Side-view images of the dust cloud's central region (produced within the CASPER GEC RF reference cell). At lower discharge powers, the particles' motion is inhibited by neutral gas damping (2.71 W – 3.10 W). As the discharge power increases (> 3.10 W), the ion flow becomes stronger, overcoming the effect of gas damping and resulting in the propagation of DAWs as indicated by the enhanced glow reflection of the wave fronts. (Gas pressure 350 mTorr.)

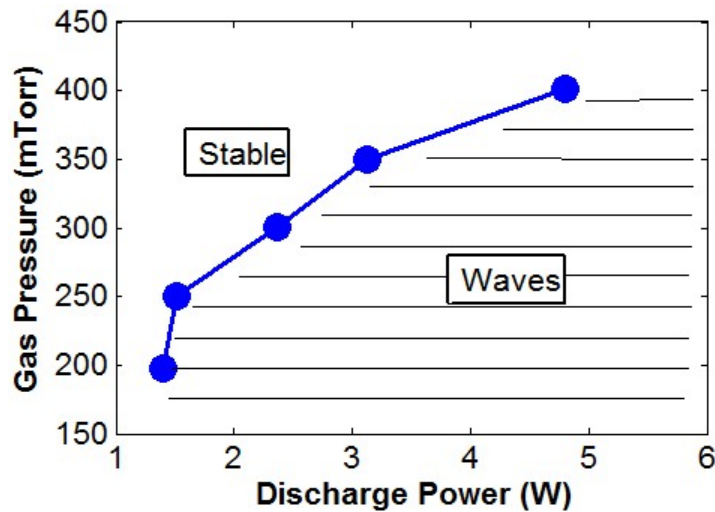


Fig. 5.9. The threshold power for creating DAWs at different pressures. The blue dots denote the experimentally observed thresholds. The shadow regime on the right side of the blue line represents conditions under which DAWs can occur, while the left, unshaded region shows stable conditions for the dust cloud.

5.4.2. Space-Time Diagrams

A common analysis technique applied to images such as those recorded in the experiments described above employs a method which produces a “*space-time diagram*,” a two-dimensional gray scale plot of light intensity (Schwabe *et al* 2007). A space-time

diagram can be constructed from a series of recorded images as follows. First, a spatial region located at the center of the dust cloud having dimensions 148×324 pixels is cropped from each image, as indicated in Fig. 5.10. The light intensities $I(x, z, t)$ in the cropped region are averaged over the horizontal direction (x -direction), yielding a vertical profile of light intensities $I(z, t)$, i.e., as a function of z , where the vertical direction z points downward in the following analysis. Finally, profiles for each image are plotted next to one another, resulting in a space-time diagram. A representative example of a space-time diagram for the DAW produced inside the glass box described above (Fig. 5.10) is shown in Fig. 5.11. Since the brightness indicates the density of the particle cloud, the space-time diagram provides a visual representation of the propagating wave with wave fronts appearing as a sequence of bright and dark stripes, as shown in Fig. 5.11.

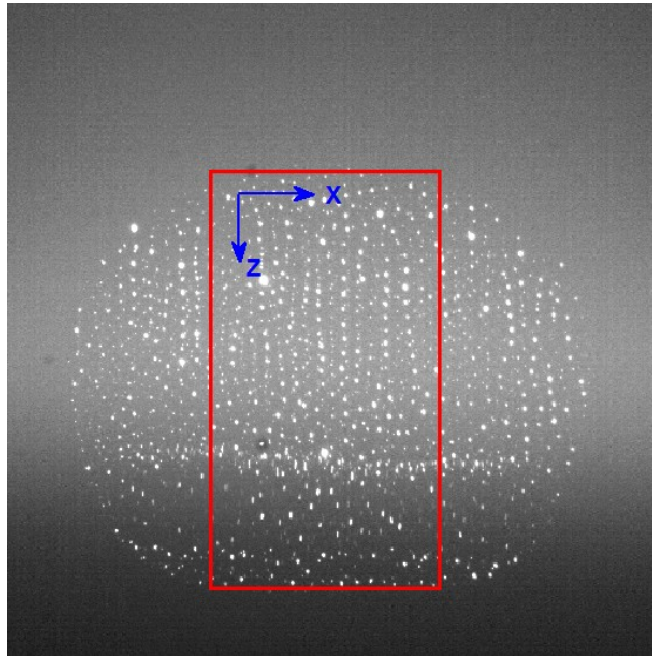


Fig. 5.10. Image of a dust cloud inside a glass box. The rectangular region bounded in red is the cropped region for analysis. The entire image is 512×512 pixels, while the cropped region is 148×324 pixels ($20 \mu\text{m}$ per pixel.)

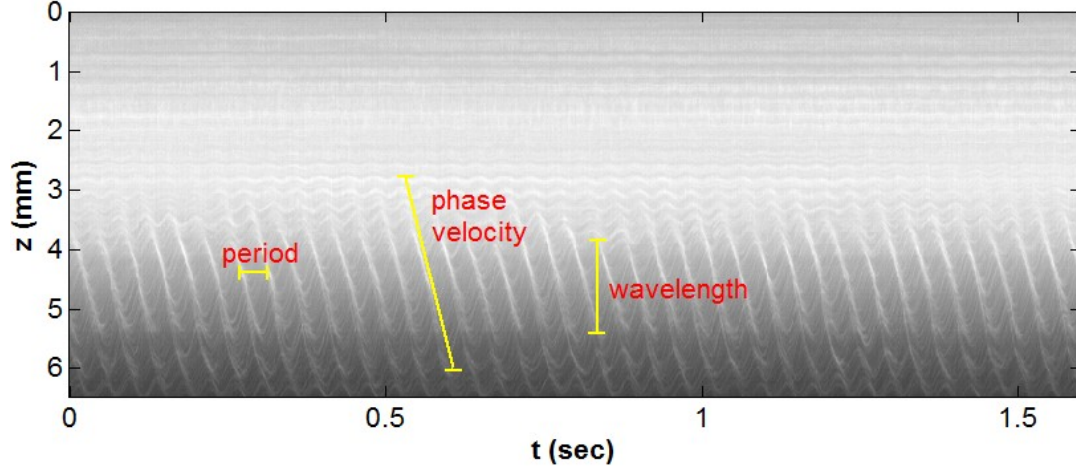


Fig. 5.11. Space-time diagram for the dust cloud region shown in Fig. 5.11. The figure represents 800 frames of collected data at a recording rate of 500 frames per second. The yellow lines indicate the wave period, phase velocity and wavelength, respectively.

A space-time diagram allows for rapid measurement of the wave period, phase velocity, and wavelength. The wave period can be obtained using the time interval between any two stripes in the horizontal direction, while the wavelength can be obtained using the distance between the wave ridges in the vertical direction. The slope of the stripe corresponds to the phase velocity of the wave. Unfortunately, the higher harmonics of the waves cannot be determined using a space-time diagram. Thus, an alternate analysis method is required. This will be discussed in the next section.

5.4.3. Power Spectrum

The power spectrum analysis method is widely used to determine the properties of higher wave harmonics. This method has the advantage that multiple frequencies and amplitudes can be distinguished and compared in a single diagram.

The data described in the previous section is now analyzed to illustrate the steps in creating a power spectrum. First, a fast Fourier transform in the temporal domain of the light intensities data $I(t, z)$ for all images recorded is applied, resulting in the

spectrum $|I(\omega, z)|$, shown in Fig. 5.12 (a) where several harmonics with a fundamental frequency of 24.2 Hz. Choosing the position ($z_0 = 4.2$ mm) where six harmonics are visible, their amplitudes for the harmonics can be determined as shown in Fig. 5.12 (b).

The phase is given by the phase angle, $\phi(z) = \arctan[I_{Im}(\omega, z) / I_{Re}(\omega, z)]$. The relative phase for the fundamental is shown in Fig. 5.13. Plotting the phase difference and choosing a region where the wave is visible, the slope of a linear fit gives the value of the wave number, in this case $k = 34.2 \text{ cm}^{-1}$, resulting in a phase velocity $v_{ph} = \omega/k = 4.46 \text{ cm/s}$.

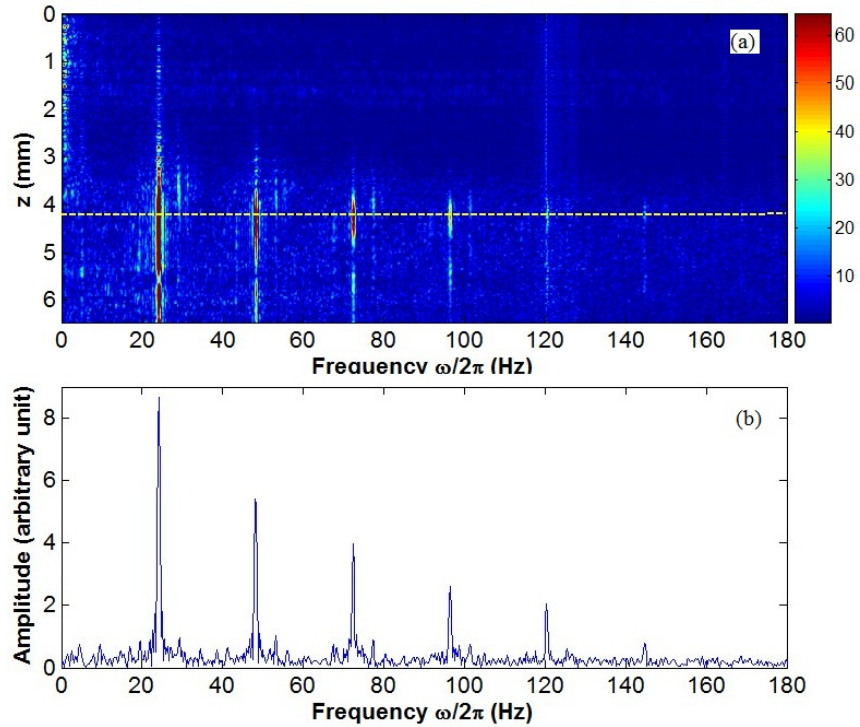


Fig. 5.12. (a) Spectrum $|I(\omega, z)|$ in the frequency domain. Several harmonics can be distinguished and a fundamental frequency is established at 24.2 Hz. (b) Spectrum $|I(\omega, z_0)|$ in the frequency domain at the position $z_0 = 4.2$ mm as indicated by the dashed line in (a).

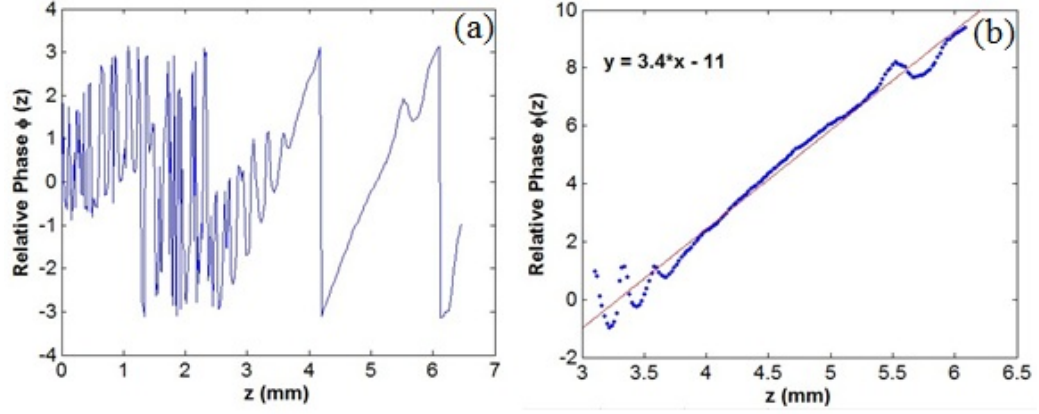


Fig. 5.13. (a) Relative phase distribution for the fundamental wave shown in the cropped region in Fig. 5.10. (b) Linear fit of relative phase in the region where the wave is visible ($3.1 \text{ mm} < z < 6.1 \text{ mm}$). The slope gives the wave number $k \cong 34.2 \text{ cm}^{-1}$.

Then, a fast Fourier transform in the spatial domain is applied to the frequency spectrum $\mathbb{I}(\omega, z)$, resulting in the power spectrum $|\mathbb{I}(\omega, k)|$ which represents the DAW energy in the (ω, k) space shown in Fig. 5.14. This power spectrum clearly shows that the waves' energy is mainly distributed in the fundamental wave and its higher harmonics.

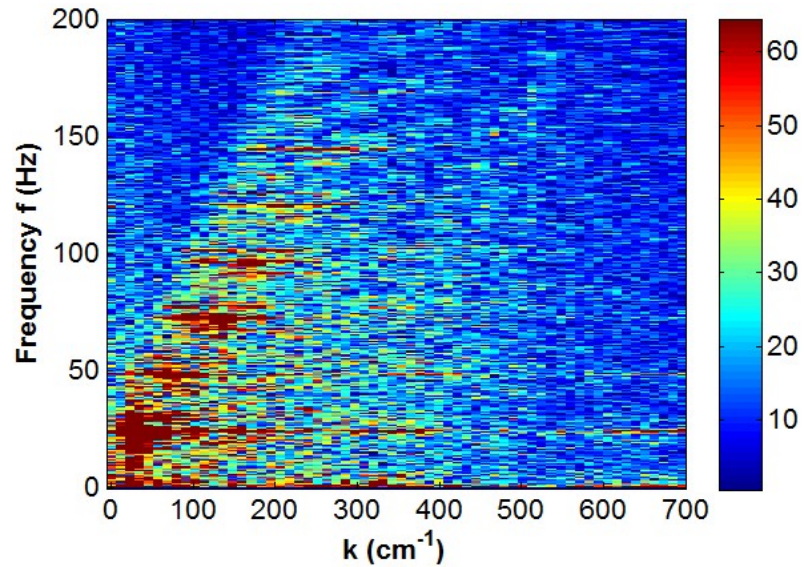


Fig. 5.14. Power spectrum for DAWs in the dust cloud. Each pixel denotes a value of $|\mathbb{I}(\omega, k)|$ which indicates the power of a specific wave.

5.4.4. DAW Dependence on Discharge Power and Gas Pressure

Employing the analysis techniques described in Sections 5.4.2 and 5.4.3, several fundamental wave parameters can now be measured experimentally under various conditions, i.e., different discharge powers and gas pressures. Fig. 5.15 (a) and (b) show measured representative fundamental frequencies and wave numbers for DAWs within a pressure range of 200 mTorr to 400 mTorr and discharge powers of 2 W to 15 W, respectively. Frequency measurements have less than 1% error, while the measured wave numbers are subject as much as to 10% uncertainty. As shown in Fig. 5.17 (a) and (b), the fundamental frequency and wave number increase with discharge power across all gas pressures.

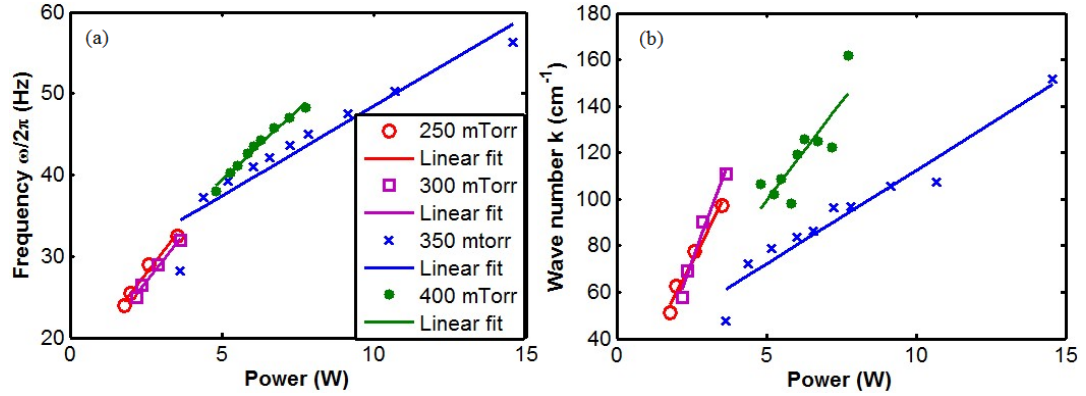


Fig. 5.15. (a) Fundamental frequencies and (b) wave numbers for DAWs produced in the dust cloud described in the text under various plasma conditions. The measured frequencies have uncertainties smaller than 1%, while the resulting wave numbers can have uncertainties as large as 10%.

The amplitudes of the DAWs shown increase as they propagate toward the lower electrode (see Fig. 5.16) for a gas pressure of 300 mTorr. As can be seen, these DAW amplitudes remain almost constant until reaching a critical point, after which they increase rapidly to a maximum value at $z \sim 0.5$ cm. The critical point is located at $z \sim 0.4$

cm, above which the dust cloud corresponds to the stable chain structure shown in Figs. 5.11 and 5.12. The relative uncertainties in the amplitudes reach a maximum at $z \sim 0.3$ cm (see Fig. 5.16 (a)) and are due to the lack of light reflected from the dust particles and the background plasma. The amplitudes of the DAWs in the region $0.4 \text{ cm} < z < 0.7 \text{ cm}$, where the DAWs can be clearly observed, are expanded in Fig. 5.16 (b), in which rapid increases in amplitudes ($0.4 \text{ cm} < z < 0.5 \text{ cm}$) and the saturation region ($0.5 \text{ cm} < z < 0.7 \text{ cm}$, where the amplitude does not increase any more) can be easily distinguished. An exponential fit to the amplitudes ($e^{-k_i z}$) of the DAWs formed in the regions between the starting point and the saturation point gives the wave growth rate $-k_i$, which is the negative of imaginary portion of the wave number (Flanagan and Goree 2010). The resulting growth rate, $-k_i$, with an approximate 40% uncertainty resulting from the exponential fit, is shown in Fig. 5.17.

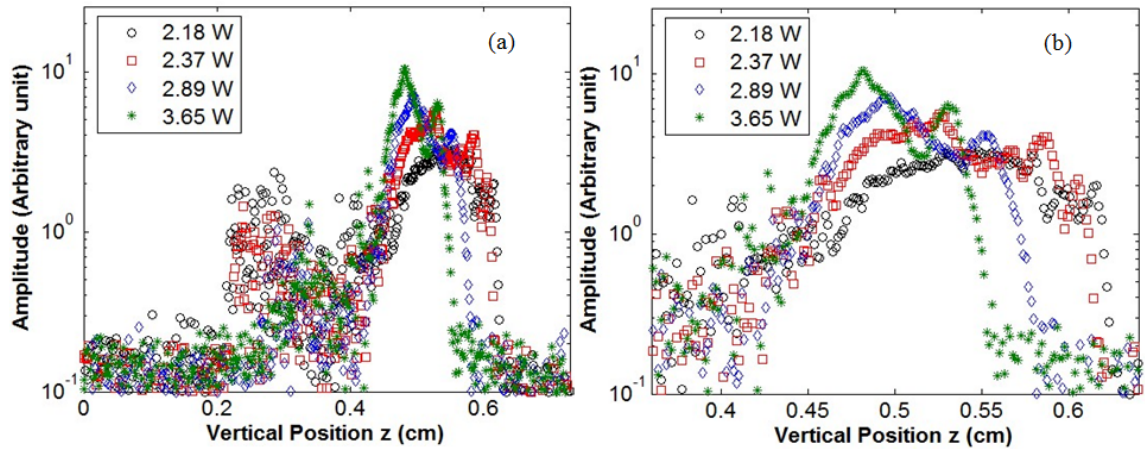


Fig. 5.16. Amplitudes of the DAWs within the entire dust cloud (a) and in only the regions where they can be visually observed (b). The relative large uncertainty at $z \sim 0.3$ cm is due to the lack of light reflected from the dust cloud. The waves start to grow at $z \sim 0.4$ cm; after reaching a maximum value the wave amplitude remains saturated.

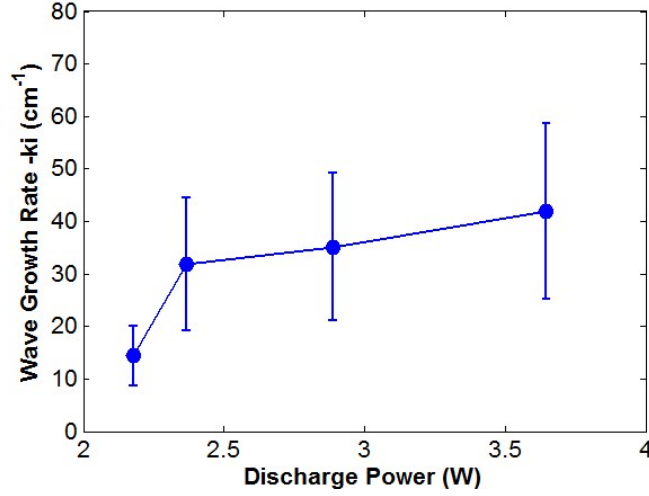


Fig. 5.17. Growth rates of DAWs in the dust cloud.

5.4.5. Development of Wave Nonlinearity

As shown in Figs. 5.12 and 5.16, DAWs grow in amplitude when propagating towards the lower electrode and can show significant nonlinearity. In order to examine the nonlinear component of the DAWs, self-excited DAWs were generated within the dust cloud for a neutral gas pressure of 300 mTorr at 2.18 W discharge power. A space-time diagram for this case is shown in Fig. 5.18 in which both the upper chain structure ($z < 0.20$ cm) and the lower wave instability ($0.20 \text{ cm} < z < 0.38$ cm) can be clearly distinguished. The fundamental frequency is confirmed to be 24.7 Hz and the corresponding wave number measured to be 57.1 cm^{-1} , resulting in a phase velocity $v_{ph} = 2.72 \text{ cm/s}$.

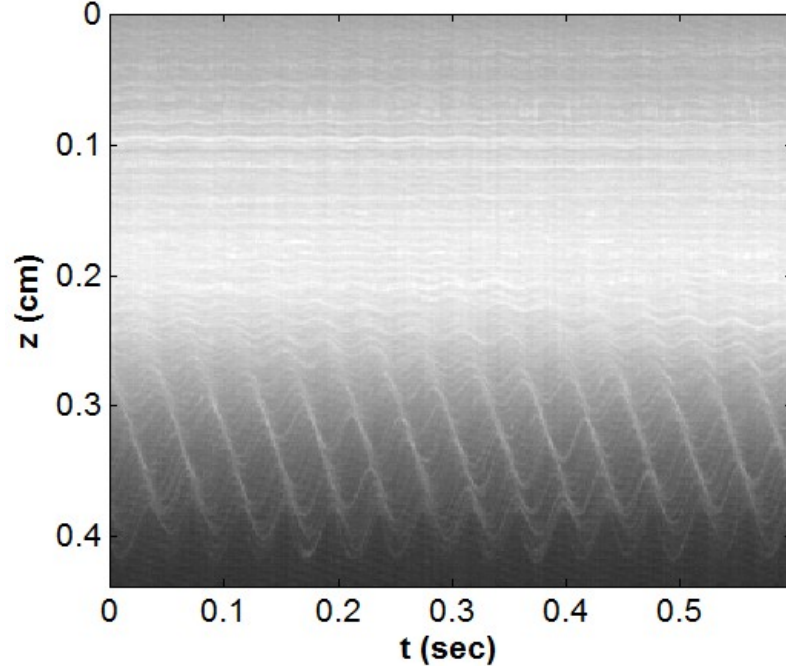


Fig. 5.18. Space-time diagram. The discharge power is 2.18 W and the gas pressure is 300 mTorr.

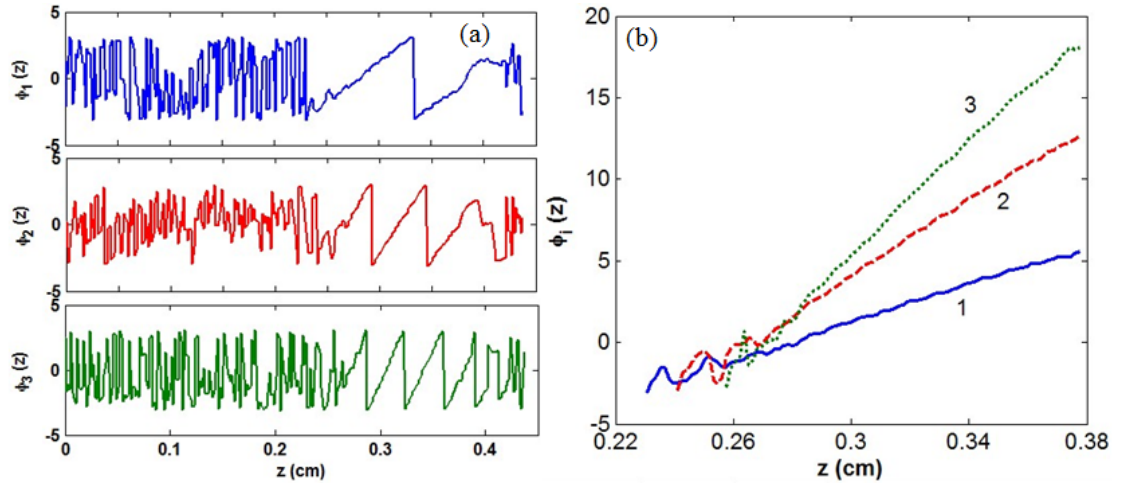


Fig. 5.19. The phases of the DAWs propagating in the dust cloud (a) and in the region $0.23 \text{ cm} < z < 0.38 \text{ cm}$ where the DAWs can be clearly observed (b) for the fundamental (blue), second harmonics (red), and third harmonics (green). $\phi_i(z)$ denotes the phase of the i^{th} harmonic. The 2π difference has been treated in (b). Linear fits to the phases give the corresponding wave numbers.

To examine the nonlinear nature of the DAWs, the fundamental, second, and third harmonics were chosen to produce the phase and amplitude development shown in Figs. 5.19. As shown in Fig. 5.19 (a), in the region $0.23 \text{ cm} < z < 0.38 \text{ cm}$ where the DAWs can be clearly observed, the phases are linearly distributed. A linear fit yields the values of the wave numbers as $k_1 = 57.1 \text{ cm}^{-1}$, $k_2 = 114.2 \text{ cm}^{-1}$, and $k_3 = 173.5 \text{ cm}^{-1}$. The relationship between the three, $k_3 = 3 k_1$, $k_2 = 2 k_1$, is the same as that observed in Flanagan and Goree's experiments (Flanagan and Goree 2011). In Fig. 5.20, the amplitudes of the harmonics can be seen to increase starting at a critical point ($z \sim 0.23 \text{ cm}$) reaching a maximum value at $z \sim 0.31 \text{ cm}$. An exponential fit between the initial and saturation points yields the corresponding wave growth rates, which are $-k_{i1} = 18.6 \pm 0.6 \text{ cm}^{-1}$, $-k_{i2} = 29.6 \pm 1.1 \text{ cm}^{-1}$, and $-k_{i3} = 38.1 \pm 1.6 \text{ cm}^{-1}$, as shown in Fig. 5.21.

Since the amplitudes of the waves represent the energy carried, it is of interest to compare the energy within the fundamental to that carried by the higher harmonics. Defining the energy index η ,

$$\eta = \frac{\sum_{i=2} A_i^2}{A_1^2}, \quad (5.6)$$

as the ratio of the sum of the powers of the harmonics to the power of the fundamental (i.e., the “*Total Harmonic Distortion (THD)*”), an indicator of the nonlinearity of the wave can be examined, as shown by Flanagan and Goree (Flanagan and Goree 2011). Harmonics up to fifth order are included, and the calculated energy index η is shown in Fig. 5.22. As shown, η increases as the DAWs propagate towards the lower electrode, reaching saturation (close to unity) at $z \sim 0.31 \text{ cm}$; this indicates the strong nonlinearity of the DAWs.

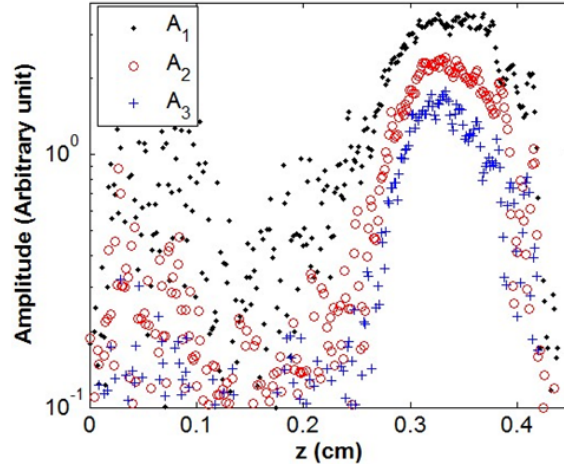


Fig. 5.20. The amplitudes of the fundamental, second, and third harmonics.

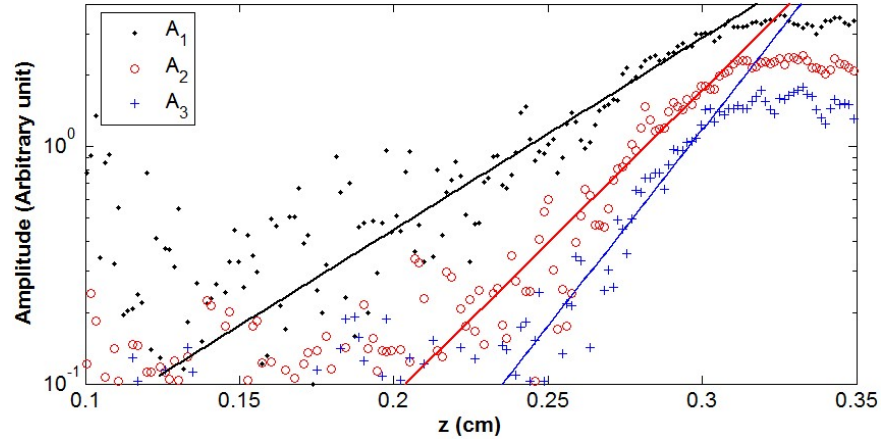


Fig. 5.21. Exponential fit for the development of wave amplitudes. The symbols denote the experimental data while the lines correspond to exponential fits.

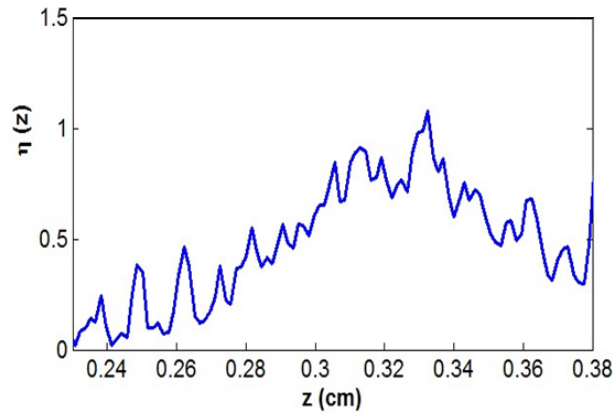


Fig. 5.22. The energy index distribution η in the vertical direction.

5.4.6. Electric Field Diagnostics

As mentioned in the previous sections, there is an initial point where a DAW begins to increase rapidly in amplitude. To understand the physical principle behind this phenomenon, it is necessary to first understand the electric field distribution inside the glass box.

In order to introduce minimum perturbation into the system, the particle-drop technique described in Chapter Four was used. First, a self-excited DAW was generated inside the glass box and data collected. Afterwards, the plasma was shut off and all dust particles removed from the system. The plasma was then re-ignited and the discharge conditions returned to the identical parameters under which the DAW was originally generated (298 mTorr gas pressure and 2.55 W RF power.) MF particles having diameters of $6.5 \mu\text{m}$ were then dropped into the system once the discharge became stable. Data was collected as the dust particles fell through the plasma to obtain their equilibrium positions. The particle's trajectory was extracted from the recorded video, allowing the particle's velocity and acceleration to be obtained through $v_i = (z_i - z_{i-1}) / \Delta t$ and $a_i = (v_i - v_{i-1}) / \Delta t$ where $\Delta t = 1 / 500 \text{ s}$ is the recording interval time employing a three-neighbor-averaging approach. According to Newton's Law, the particle's equation of motion is given by $ma = mg - m\beta v - F_E$. Solving for the electric force gives $F_E / mg = 1 - (\beta v + a) / g$. The electric force profiles for two free falling particles are shown in Fig. 5.23 (a). It can be seen that the electric force acting on the dust particle remains at almost zero until $z = 0.18 \text{ cm}$, after which it increases as the particle approaches the lower electrode. In other words, in the region above $z = 0.18 \text{ cm}$, the electric field resulting from the charged walls of the glass box and the background plasma

can be considered negligible. For comparison, Fig. 5.23 (b) and (c) show the phase and amplitudes of DAWs propagating in a dust cloud inside the glass box under the same discharge conditions, respectively. The starting point for the growth of the phase and amplitude is at approximately $z \sim 0.2$ cm. Fig. 5.23 (d) shows the velocity perturbation $\langle v^2 \rangle - \langle v \rangle^2$ for every particle having more than one period of trajectory information within the dust cloud (where, “ $\langle \rangle$ ” represents an average over time.) As shown in Fig. 5.24 (d), the velocity perturbation remains negligible ($\sim 10^{-6}$) until $z = 0.18$ cm before increasing by three orders of magnitude at $z = 0.38$ cm, where the amplitudes of the DAWs reach their maximum values. This trend is similar to the distribution found for the electric force.

The overlap of the initial growth points for the electric force, the phase and the amplitude of the DAWs and the particle velocity perturbation occurs for a reason. It is believed that a self-excited DAW is created due to an ion streaming instability (Merlino 2009; Flanagan and Goree 2010), where the instability overcomes neutral gas damping. As the ion streaming is proportional to the electric field E (Frost 1957) which increases toward the lower electrode (Douglass *et al* 2012), at a critical point the streaming instability increase significantly exciting a DAW. The experimental observation agrees with theoretical prediction.

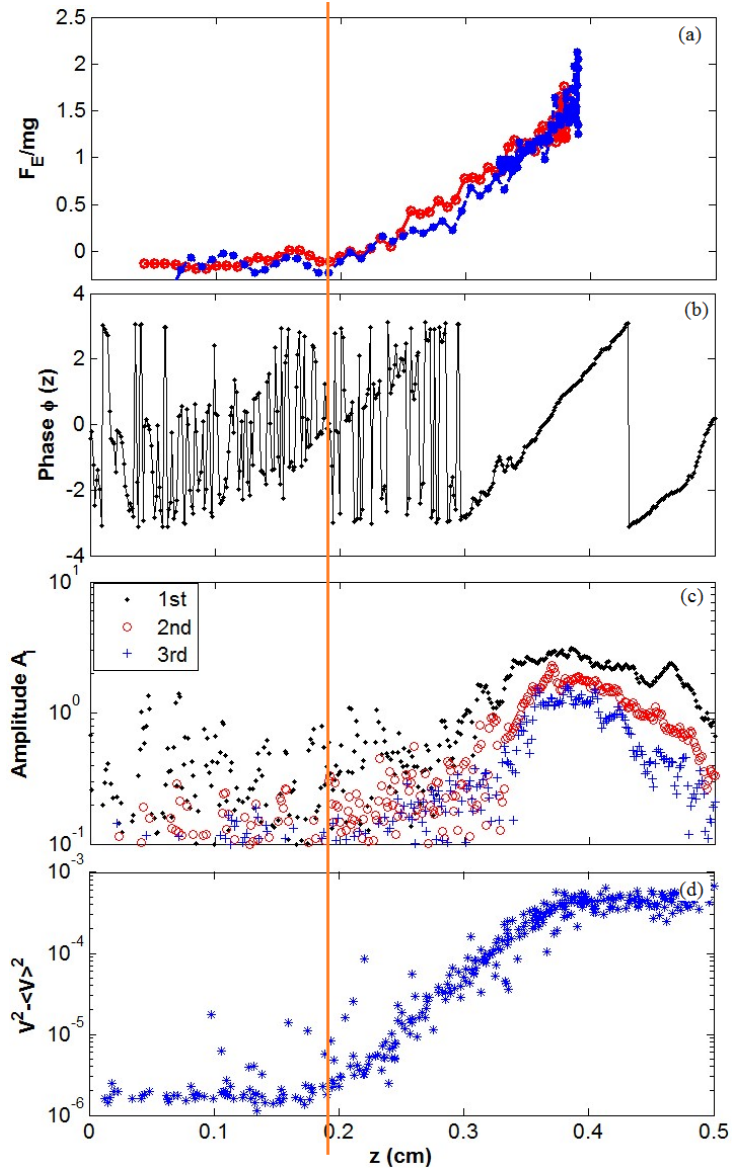


Fig. 5.23. (a) The electric forces acting on freely falling dust particles. (b) The phase and (c) the amplitudes of the DAWs propagating within a dust cloud. (d) The velocity perturbation $\langle v^2 \rangle - \langle v \rangle^2$ for every particle having more than one period of trajectory information. The orange vertical line indicates the initial point of the development for each aspect.

5.4.7. Interaction between Driven and Self-Excited DAWs

One commonly used technique to study the dispersion relationship for a DAW is through modulation of the plasma discharge parameters, for instance, modulating the discharge current (Thomas E *et al* 2007), power (Schwabe *et al* 2008), or bias on the

electrode (Trottenberg *et al* 2006). It was believed these modulations would couple to particular modes in the spectra of wave modes observed to exist in the self-excited wave modes.

In the experiments conducted here, two separate dust clouds were investigated. The first (Cloud I) included 1.5×10^4 dust particles in a plasma at 250 mTorr gas pressure and 3.8 W discharge power, while the second (Cloud II) included 2.5×10^4 dust particles, with 250 mTorr gas pressure and 1.5 W discharge power. Under these conditions, DAWs within the dust clouds occurred naturally. Employing both space-time diagram and power spectrum approaches, the frequencies and wave numbers for the self-excited DAWs in the two dust clouds were measured to be 24.2 Hz and 36.9 cm^{-1} and 20 Hz and 27.1 cm^{-1} , respectively. A series of sinusoidal modulations with frequencies between 1 and 100 Hz were then used to produce driven wave modes in an attempt to interact with the self-excited DAWs within the clouds. However, interaction between these wave modes was observed only over a limited set of frequencies: for Cloud I the frequency range was 10 – 32 Hz while for II the range was between 13 – 27 Hz.

In order to study the wave interaction, attention was focused on the frequency spectra. Employing the power spectrum technique, the spectrum in the frequency domain $|I(z, \omega)|$ was obtained and normalized by the maximum value $|I(z, \omega)|_{\text{max}}$. This provides frequency spectrum $I(\omega)$ over the entire wave propagation region allowing the interaction between driven and self-excited DAWs to be directly observed. The resulting frequency spectra for both the driven and self-excited DAWs in Cloud I are shown in Fig. 5.24. In Fig. 5.24, f_0 and f_I denote the self-excited and driven fundamental frequencies with $2f_0$, f_I and $3f_0$, f_I corresponding to the second and third harmonics. As shown in Fig.

5.24 (a), strong peaks at the fundamental frequency of 24.2 Hz, along with the higher harmonics of the self-excited DAW, are present. When a driven wave mode is superimposed on a self-excited DAW, the fundamental frequencies of both the driven and self-excited waves appear with mixing frequencies occurring (i.e., $f_0 + f_1, f_0 + 2f_1 \dots$) as shown in Fig. 5.24 (b)-(d) (driving frequency 10-20 Hz). The sum of these frequencies implies that waves propagate in the same direction while difference in these frequencies indicates propagation in the opposite direction. At higher driving frequencies (i.e., 22 Hz and above), there is strong coupling between the driven and self-excited wave modes. This has been observed to be linked to a single strong, narrow fundamental frequency peak in the frequency spectra as shown in Fig. 5.24 (e)-(f). There is no evidence of any self-excited wave mode when driving frequencies are close to or above 22 Hz for the self-excited frequency of 24.2 Hz. The same phenomenon was also observed in Cloud II where the critical frequency was shown to be 19 Hz for a self-excited frequency of 20 Hz. This is different from the phenomenon first observed by Williams and Duff (Williams and Duff 2010). In their experiments, it was observed that strong coupling occurred at lower frequencies (< 20 Hz) and decreased as the frequency increased. Mixing frequencies were not observed in their experiments. The observations here are also different from Thomas E *et al*'s (Thomas E *et al* 2007) where a wave number “lock” for a driven wave modes to self-excited modes was observed when the driving frequency was larger than the frequency of the self-excited DAW. These differences can most likely be attributed to the different discharge environments: in both Thomas E *et al* and Williams and Duff's experiments DC discharges were employed while a capacitive RF plasma was applied in the experiments discussed here. However, our observation of mixing

frequencies is consistent with Nosenko *et al*'s (Nosenko *et al* 2004) where an RF plasmas was also applied.

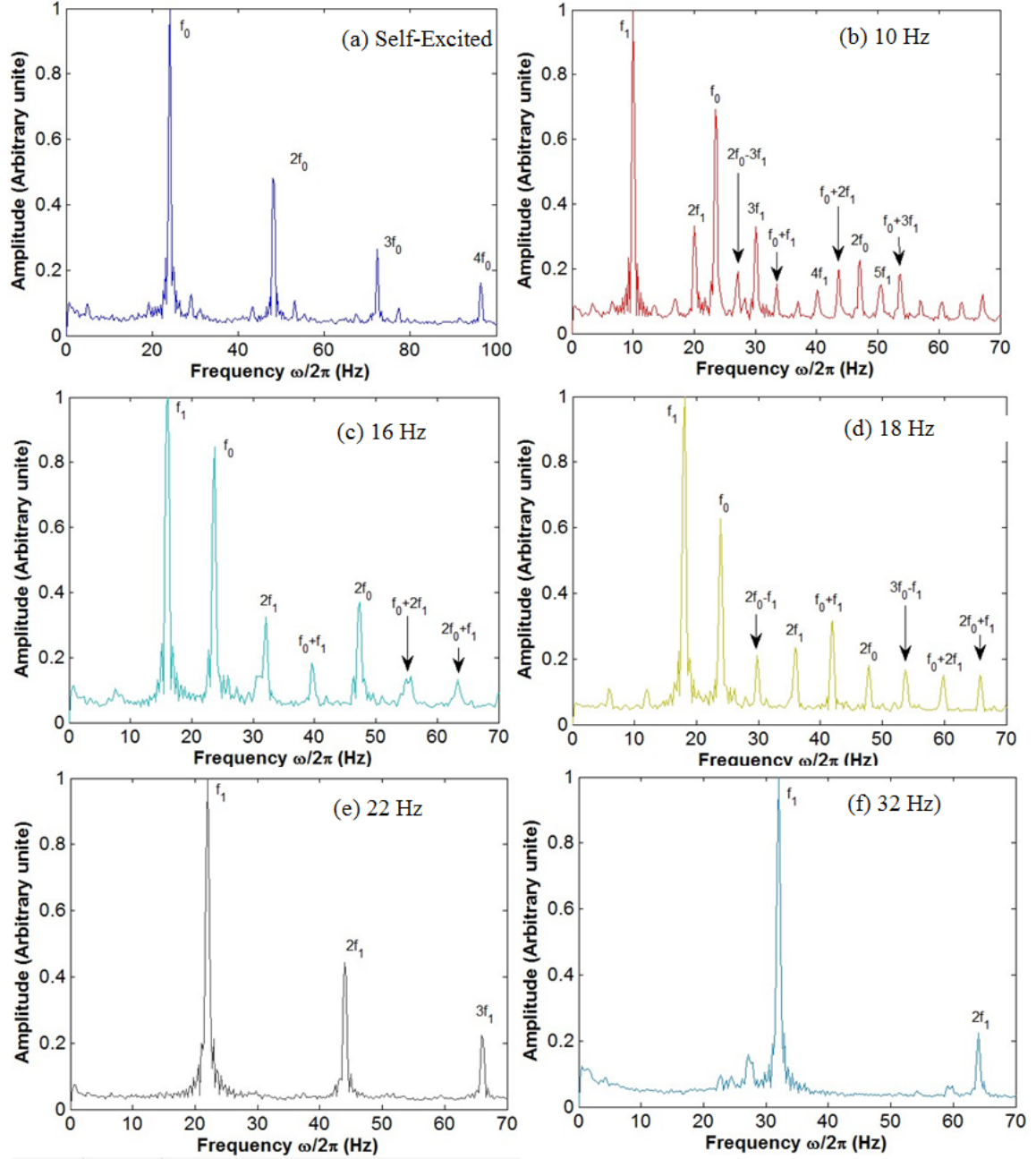


Fig. 5.24. The frequency spectra $|I(\omega)|$ for self-excited dust acoustic waves (a) and driven acoustic waves (b) - (f) in Cloud I. At lower frequencies, $f \leq 20$ Hz, the self-excited and driven wave modes interact with one another through wave-mixing, as signified by the occurrence of mixing frequencies. At higher frequencies, $f \geq 22$ Hz, strong coupling appears as signified by the single fundamental driven frequency peaks.

5.4.8. *Section 5.4 Summary*

In summary, in this section, instabilities within various dust clouds formed inside a glass box were investigated. Two commonly used analysis techniques, the space-time diagram technique and the power spectrum method, were introduced and then employed to investigate wave instabilities. It was determined that self-excited dust acoustic waves can be activated inside the glass box by either increasing the discharge power or decreasing the gas pressure. Both the frequency and wave number of these self-excited DAWs increase with discharge power with self-excited DAWs becoming highly nonlinear as they approach the lower electrode. Both an initial growth point and a saturation point exist in the dust cloud. This point coincides with the position of non-zero electric field, indicating that the non-zero electric field may be the driver behind the emergence of self-excited DAWs. Additionally, a driven modulated signal was applied to the lower electrode to provide an approach for studying the interaction between driven and self-excited waves. This interaction was shown to include both mixing and coupling modes, depending on the driving and self-excited frequencies. For the driving frequencies close to or above the DAW's self-excited frequency, coupling occurs. Otherwise, these two wave modes interact with one another primarily through mixing.

CHAPTER SIX

Effects on the Dispersion Relation of Dust Acoustic Wave

Parts of this chapter have been submitted for publication as: “Particle charge-variation, ion-drag-force fluctuation and dust temperature effect on the dispersion relationship of dust acoustic waves in a dusty plasma”, Zhuanhao Zhang, Truell Hyde, Lorin Matthews, Ke Qiao, and Jie Kong.

6.1. Introduction

As discussed previously, the presence of charged dust particles can act as a fourth component of the plasma (electrons, ions, atoms, and dust) while also affecting or even introducing wave modes, such as the dust lattice wave (DLW) and the dust acoustic wave (DAW). One of the most important properties of the DAW is the dispersion relation which is described, for an ideal dusty plasma, by Eq. 2.77. The dispersion relation for the DAW is strongly dependent on both the surrounding plasma and dust particle parameters, i.e., the electron and ion densities, particle charge, screening length, dust temperature, particle-particle interactions, etc. Any change in these parameters can lead to a modification of the dispersion relation. In this Chapter, three of these, the dust temperature, charge-variation, and the ion-drag-force fluctuation, are examined to determine the manner in which they impact the dispersion relation of the DAW. In section 6.2, previous investigations of these three effects are briefly described. A set of equations is used to theoretically calculate the dust particle and plasma parameters (e.g., the particle charge, electric field, and ion flow velocity) and is introduced in section 6.3. The ion-dust two stream instability theory and detailed calculations of the dispersion relation are introduced in section 6.4. Finally, theoretical results for the dispersion

relation and resulting instabilities are compared with experiment in section 6.5, followed by conclusions in section 6.6.

6.2. Previous Investigation on the Dispersion Relation of a DAW

Traditionally, the three major parameters impacting the dispersion relation of a DAW are believed to be the ion flow instability (Rosenberg 1993), the ionization instability (D'Angelo 1998), and the particle charge variation (Fortov et al 2000b). More recently, the effect that a finite dust temperature has on the DAW dispersion relation was determined by Rosenberg *et al* (Rosenberg *et al* 2008) and Thomas E (Thomas E 2010). The ion-drag-force has in general been ignored due the assumption that its amplitude is much smaller than the amplitude of either the electric or gravitational force. In the following, a general discussion concerning the effects of the charge variation, dust temperature, and ion-drag-force fluctuation is given.

6.2.1. Particle Charge Variation Effect

In 2000, a fluid model analysis of the dispersion relationship provided by Fortov *et al* (Fortov et al 2000b) showed that observed DAW instabilities in DC glow discharge dusty plasmas resulted from dust charge variations in the presence of external charge-dependent forces and ion drift. Similar experimental and analytical results were presented by Zobnin *et al* (Zobnin *et al* 2002) who showed that dust charge variations can lead to both wave damping and growth. In their analysis, traditional OML theory was employed to provide information on the charge variation. Although this technique was suitable for their experimental setup, which employed a DC discharge, the applicability of their theory for RF discharge plasmas is still unknown.

6.2.2. Dust Temperature Effect

Rosenberg *et al* (Rosenberg *et al* 2008) considered finite dust temperature effects on two stream ion-dust instabilities and found that they can significantly affect the DAW dispersion relation. Thomas E *et al* (Thomas E *et al* 2007; Thomas E 2010) and Williams *et al* (Williams *et al* 2008) showed that these finite dust temperature effects must be included in order to most accurately model experimentally measured dispersion relations and confirmed the kinetic dust temperature experimentally using a stereoscopic particle image velocimetry technique (Williams *et al* 2006). In their experiments, coupling between dust particles was assumed to be small, allowing an ideal gas model to be employed to represent the dust temperature. More recently it was shown that for small dust temperature ($T_d \sim 0.03$ eV), dust particles can strongly interact electrostatically with each other, impacting the resulting DAWs (Yaroshenko *et al* 2010) in a manner analogous to the thermal effect seen in high temperature ($T_d \sim 100$ eV) plasmas. In Yaroshenko *et al*'s work, this electrostatic interaction between dust particles was examined using an ideal dust crystal model.

It is important to note that when dust particles are in a liquid state, neither the ideal gas model nor the ideal crystal model can suitably represent the dust temperature effect theoretically. At the same time, the similarity between the effect of high and low dust temperatures on the dispersion relation of a DAW suggests that there may be some connection between the two. In order to rectify both of these, a new model which is able to properly express the dust temperature in the gaseous, liquid, or solid state is necessary. In each of the theoretical calculations or experimental measurements discussed above, the

ion drag force was neglected under the assumption that its effect on the dispersion relation of the DAW was minor. This assumption has not yet been proven.

In this Chapter, the effect that the dust temperature, the charge variation and/or the ion-drag-force fluctuation has on the DAW dispersion relation is examined and a comprehensive expression for the DAW dispersion relation is derived. The charge on the dust particles is determined by the balance between the ions and electrons to the particle's surface. Unlike the work previously discussed, the ion flux is chosen to be representative of that found in a one-dimensional ion drift model; i.e., DML theory is employed. A model having the ability to properly represent the dust temperature for the gaseous, liquid or solid state is also employed. It is shown that each of these can have a significant impact on the dispersion relation of DAWs, depending on the wavelength region examined.

6.3. Plasma and Dust Particle Parameters

In a dusty plasma, dust particles become negatively charged and levitate in the sheath region above the lower powered electrode (RF) or in the plasma bulk (DC) due to the force balance between the gravitational force, the ion drag force and the electric force:

$$m_d g + F_{0,ion} = E_0 Z_{d0} e, \quad (6.1)$$

where E_0 is the electric field and $F_{0,ion}$ and Z_{d0} are the ion drag force and particle charge number on the dust particles at the equilibrium position, respectively. Assuming an arbitrary ion flow velocity, a detailed calculation of the ion drag force yields (see Section 2.6.4):

$$F_{ion} = \sqrt{2\pi} r_d^2 n_i T_i \left\{ \sqrt{\frac{\pi}{2}} \operatorname{erf}\left(\frac{u}{\sqrt{2}}\right) \left[1 + u^2 + (1 - u^{-2})(1 + 2z\tau) + 4z^2\tau^2 u^{-2} \ln \Lambda \right] \right. \\ \left. + u^{-1}(1 + 2z\tau + u^2 - 4z^2\tau^2 \ln \Lambda) \exp\left(-\frac{u^2}{2}\right) \right\}. \quad (6.2)$$

The presence of an electric field therefore provides a plasma drift relative to the dust particles. In most cases, the resulting electron drift is much smaller than the thermal velocity (Joyce *et al* 2002), $u_e \ll v_{Te}$, allowing it to be ignored. However, under certain conditions (Thomas T *et al* 2006), the ion drift can be on the same order of magnitude as the thermal velocity and must be included, taking into account both the electric field and the ion mobility, $u_{i0} = \mu_i(E)E$ (Frost 1957), where

$$\mu_i(E) = \mu_{i0} \frac{p_0}{p} \left[1 + A \frac{E}{p} \right]^{-1/2} \quad (6.3)$$

with $\mu_{i0} = 0.146 \text{ m}^2 \text{ V}^{-1} \text{ s}^{-1}$, $p_0 = 133 \text{ Pa}$, and $A = 0.035 \text{ Pa m V}^{-1}$ for argon gas, and p is the neutral gas pressure (Thomas T *et al* 2006). In this case, the ion drift can be used to determine the charge on the dust particle. Employing the DML approach, the electron and ion flux currents can be expressed as (see Section 2.5.2):

$$I_e = \sqrt{8\pi} r_d^2 n_e v_{Te} \exp\left(\frac{e\varphi_d}{k_B T_e}\right). \quad (6.4)$$

$$I_i = \sqrt{2\pi} r_d^2 n_i v_{Ti} \left[\sqrt{\frac{\pi}{2}} \frac{1 + u^2 - 2e\varphi_d/k_B T_i}{u} \operatorname{erf}\left(\frac{u}{\sqrt{2}}\right) + \exp\left(-\frac{u^2}{2}\right) \right]. \quad (6.5)$$

In this case, φ_d is the dust particle's surface potential and the charge number can be related to this surface potential through $Z_d e = -4\pi\epsilon_0 r_d \varphi_d$. In the small drift limit, $u \ll 1$, Eq. (6.5) yields an ion flux current identical to that found assuming OML Eq. (2.22).

In order to evaluate the particle's charge within the dust cloud, the quasi-neutrality condition

$$n_e + Z_d n_d = n_i \quad (6.6)$$

must be assumed in order to close Eqs. (6.1) through (6.5). Figure 6.1 shows the change in the dust particle's charge number, the ion flow velocity, electron density, and ion drag force as a function of the ion density for differing dust cloud densities and particle sizes with a gas pressure of 200 mTorr. In the figures, r_{d1} , r_{d2} , and r_{d3} denote the radii of dust particles, which are $1 \mu\text{m}$, $3.25 \mu\text{m}$, and $6 \mu\text{m}$, respectively. As can be seen in Fig. 6.1 (a), dust particles in less dense clouds acquire more charge. This is most easily explained through the “close packing” effect (Barken *et al* 1994; Angelis and Forlani 1998) which shows that particle charge decreases with increasing dust particle density but increases with plasma density. According to Eq. (6.3), the ion flow velocity is linearly proportional to the electric field E when $AE/p \ll 1$, and to the square root of the electric field ($E^{1/2}$) when $AE/p \gg 1$. Due to the dust particle concentration, the local electric field increases resulting in an increase of the ion flow velocity, in agreement with Sukhinin *et al* (Sukhinin *et al* 2010), as shown in Fig. 6.1(b). As expected, figures 6.1 (a) and 6.1 (b) show that, compared to smaller dust particles, larger particles gain more charge due to their larger surface area and require a larger electric field (i.e., larger ion flow) to levitate due to their greater mass. Figure 6.1(c) indicates that the depletion of electrons is smaller when the dust particle density and radii are smaller, due to their smaller total surface areas. The ion drag force increases with the ion density and can become comparable to or even greater than the gravitational force (Fig. 6.1(d)).

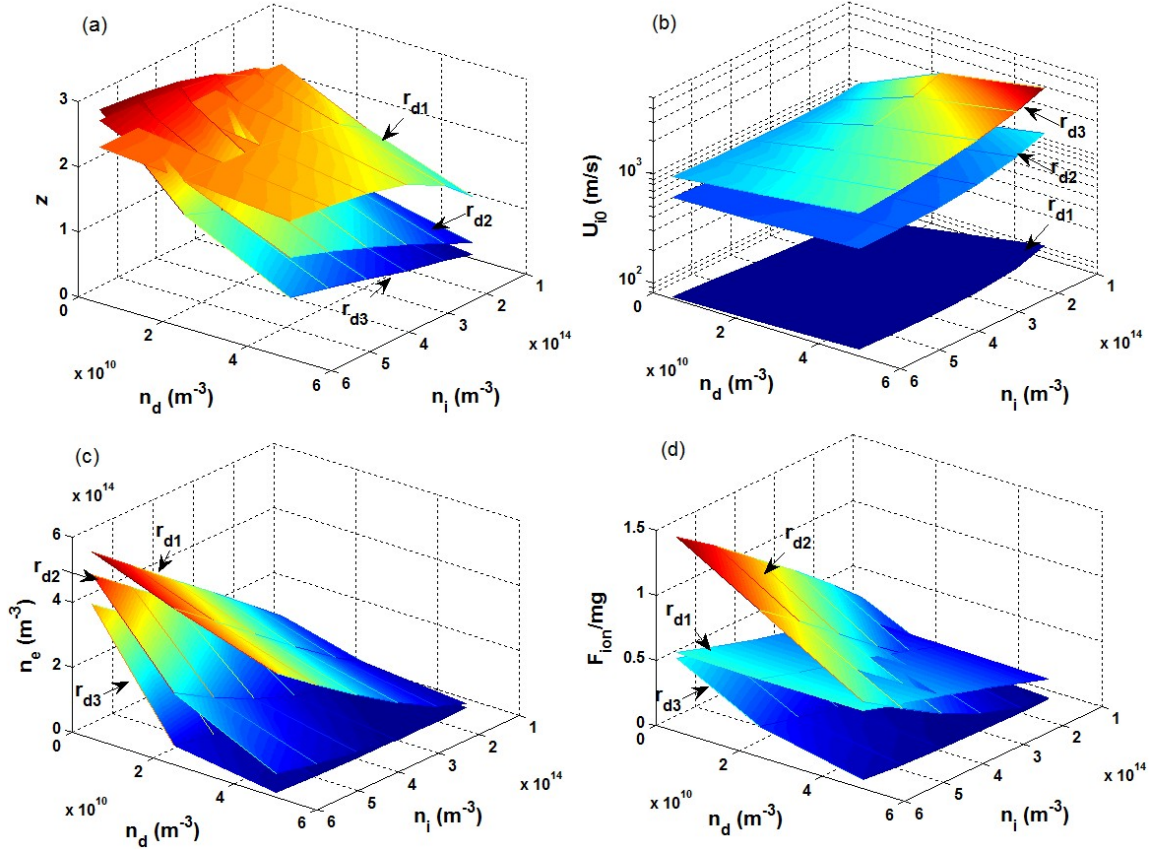


FIG. 6.1. Parameters for dust particles and plasma calculated employing Eqs. (6.1) through (6.6). (a) Particle normalized charge number; (b) ion flow velocity; (c) electron density; and (d) ion drag force. In the above, r_{d1} , r_{d2} , and r_{d3} denote the radii of the dust particles which are $1 \mu\text{m}$, $3.25 \mu\text{m}$, and $6 \mu\text{m}$, respectively.

6.4. Fluid Model Analysis

6.4.1. Susceptibility Equation

The dispersion relation for the DAW can be expressed as a sum of the susceptibilities for each species in the dusty plasma (Tsytovich *et al* 2001; 2002)

$$\varepsilon(\omega, k) = 1 + \chi_i + \chi_e + \chi_d = 0. \quad (6.7)$$

In Eq. (6.7), the electron and ion susceptibilities are defined as $\chi_{i,e} = \mp 4\pi e n_{i,e} / k^2 \phi_1$ and the dust susceptibility is given by

$$\chi_d = 4\pi e(Z_{d1}n_{d0} + Z_{d0}n_{d1})/k^2\varphi_1. \quad (6.8)$$

In each case, first order perturbations are denoted by the subscript “1”; for example, φ_1 and Z_{d1} represent first order perturbations of the local electrostatic potential and the charge on the dust particles, respectively. It is assumed all perturbations are small and have a space-time dependence which can be described by $e^{i(kx - \omega t)}$.

Employing linearized continuity and momentum equations, the ion and electron susceptibilities can be expressed as (D’Angelo and Merlino 1996)

$$\chi_\alpha = -\frac{\omega_{p\alpha}^2}{(\omega - u_{\alpha 0}k + i\gamma_{\alpha n})(\omega - ku_{\alpha 0}) - k^2T_\alpha / m_\alpha} \quad (6.9)$$

where, $\alpha = i, e$, $\omega_{p\alpha} = (4\pi n_\alpha e^2 / m_\alpha)^{1/2}$ are the ion and electron plasma frequencies, $u_{\alpha 0}$ is the stable flow velocity, and $\gamma_{\alpha n} = eE_0 / m_\alpha u_{\alpha 0}$ is the ion/electron – neutral collision rate.

6.4.2. Dust Temperature

For dust particles, if the dust temperature T_d is sufficient high ($T_d \sim 100$ eV), their interparticle interaction is negligible. In this case, the dust particles can be considered an ideal gas, and the dust pressure expressed by the ideal gas law, $P_{(g)} = n_d k_B T_d$ (Rosenberg *et al* 2008; Thomas E *et al* 2007). At the other limit, when T_d is extremely low ($T_d < 1$ eV), dust particles can easily form solid crystalline structures. In this case, the dust crystalline pressure can be expressed by (Kittel 1996)

$$P_{(cr)} = \frac{(1 + \alpha\kappa)\exp(-\alpha\kappa)}{3\alpha} N_{nn} \Gamma P_{(g)}, \quad (6.10)$$

where $\kappa = \Delta / \lambda_D$ is the lattice parameter, $\Delta = n_d^{-1/3}$ is the mean interparticle distance, and

$\Gamma = Q^2 / 4\pi\epsilon_0 \Delta k_B T_d$ is the coupling parameter. N_{nn} is defined as the number of nearest

neighbor particles; $N_{nn} = 8$ and $\alpha = 1.09$ for a bcc (body-centered cubic) lattice, while $N_{nn} = 12$ and $\alpha = 1.12$ for hcp (hexagonal closed packed) and fcc (face-centered cubic) lattices. The dust particles are considered to be in a gaseous state if $\Gamma < 1$, and in a solid state if $\Gamma > \Gamma_{cr} = 106 \exp(\kappa) / (1 + \kappa + \kappa^2 / 2)$ where $\Gamma_{cr}(\kappa)$ can be identified on the crystal-liquid curve in Fig. 2.15 (Vaulina and Khrapak 2000). For a DAW propagating within a dust cloud, the dust particles are usually in a liquid-like state and interact with their neighbors.

In order to obtain the equation of state for a dust system in the liquid phase, a linear interpolation approach (Gozadino *et al* 2003; Goedheer *et al* 2009) can be employed to yield:

$$P_{(l)} = P_{(g)}(1 - c) + P_{(cr)}c \quad (6.11)$$

with $c = (\Gamma - 1) / (\Gamma_{cr} - 1)$. The dust pressure can now be obtained as

$$P_d = C' m_d n_d \quad (6.12)$$

where

$$C' = k_B T_d [1 - c + c(1 + \alpha\kappa) \exp(-\alpha\kappa) N_{nn} \Gamma / 3\alpha] / m_d \quad (6.13)$$

is the “effective dust temperature” (Yaroshenko *et al* 2009). As shown, C' is a function of the dust temperature T_d and the coupling parameter κ .

6.4.3. Ion-Dust Two Stream Instability Theory

Assuming the dust particles do not act as either sources or sinks, the continuity and momentum equations can be written as

$$\begin{aligned}\frac{\partial n_d}{\partial t} + \frac{\partial(n_d u_d)}{\partial x} &= 0, \\ n_d m_d \left(\frac{\partial u_d}{\partial t} + u_d \frac{\partial u_d}{\partial x} + u_d \gamma_{dn} \right) &= n_d (m_d g + F_{ion} - Z_d e E) - \nabla P_d\end{aligned}\tag{6.14}$$

where γ_{dn} is the dust-neutral collision rate and $E = E_0 - \partial\phi/\partial x$ is the electric field.

Assuming small perturbations and no net dust flow, i.e., $u_{d0} = 0$, and with the help of the force balance Eq. (6.1), Eq. (6.14) can be linearized

$$-i\omega n_{d1} + i k n_{d0} u_{d1} = 0,\tag{6.15}$$

$$m_d (-i\omega + \gamma_{dn}) u_{d1} = -Z_{d1} e E_0 + F_{1,ion} + Z_{d0} e i k \phi_1 - i k C' m_d n_{d1} / n_{d0}.\tag{6.16}$$

On the right hand side of Eq. (6.16), the charge variation is included in the first term, the ion-drag-force fluctuation is expressed in the second term, and the dust temperature effect is involved in the last term. The particle charge perturbation is determined by the time evolution flux relation $-\partial Z_d / \partial t = I_i - I_e$. Linearizing Eqs. (6.4) and (6.5), the particle charge perturbation can be obtained using

$$Z_{d1} = -D I_{i0} \frac{k^2 \epsilon_0}{e} \phi_1,\tag{6.17}$$

where

$$\begin{aligned}D &= \frac{1}{i\omega - \eta} \left(\frac{\chi_i}{n_{i0}} F + \frac{\chi_e}{n_{e0}} \right), \\ F &= 1 - \frac{\sqrt{2\pi} r_d^2 G u_{i0} n_{i0}}{I_{i0}}, \\ G &= \sqrt{\frac{\pi}{2}} \left(\frac{-1 + 2e\phi_d / T_i + u^2}{u^2} \right) \text{erf}\left(\frac{u}{\sqrt{2}}\right) + \frac{1 - 2e\phi_d / T_i}{u} \exp\left(-\frac{u^2}{2}\right), \\ \eta &= \frac{r_d \omega_{pi}^2}{2u_{i0}} \text{erf}\left(\frac{u}{\sqrt{2}}\right) + \frac{I_{i0} e^2}{4\pi \epsilon_0 r_d T_e}.\end{aligned}\tag{6.18}$$

In the low ion flow limit, $u \ll 1$, $G \sim 1/u$, $F = 1$, and the results obtained above reduce to those found employing OML (Fortov *et al* 2000b). Taking the derivative of Eq. (6.2), the ion drag force perturbation can now be obtained as:

$$F_{1,ion} = Hu_1 + Jn_{i1} + Kz_1 \quad (6.19)$$

where

$$\begin{aligned} K &= \frac{2a^2}{u^2} e^{-u^2/2} n_i T_i \tau \left[\sqrt{2\pi} u (1 - 4z\tau \ln \Lambda) + e^{u^2/2} \pi (-1 + u^2 + 4z\tau \ln \Lambda) \operatorname{erf}\left(\frac{u}{\sqrt{2}}\right) \right], \\ H &= \frac{2a^2}{u^3} e^{-u^2/2} n_i T_i \left\{ \sqrt{2\pi} u \left[-1 + u^2 - 2z\tau + 2 \ln \Lambda (2 + u^2) z^2 \tau^2 \right] \right. \\ &\quad \left. + e^{u^2/2} \pi \left[1 + u^4 + 2z\tau (1 - 2z\tau \ln \Lambda) \right] \operatorname{erf}\left(\frac{u}{\sqrt{2}}\right) \right\}, \\ J &= a^2 e^{-u^2/2} T_i \left\{ \sqrt{2\pi} u^{-1} \left[1 + u^2 + 2z\tau (1 - 2z\tau \ln \Lambda) \right] \right. \\ &\quad \left. + e^{u^2/2} \pi \left[2 + u^2 + 2z\tau + u^{-2} (-1 + 2z\tau (-1 + 2z\tau \ln \Lambda)) \right] \operatorname{erf}\left(\frac{u}{\sqrt{2}}\right) \right\}. \end{aligned} \quad (6.20)$$

In this case, the coefficient K provides the contribution from the charge variation to the ion-drag-force fluctuation. Substituting Eqs. (6.15), (6.17), and (6.19) into (6.16), and combining with Eq. (6.8), the susceptibility of the dust particles can now be expressed as

$$\begin{aligned} \chi_d &= -DI_{i0}n_{d0} - \frac{\omega_{pd}^2}{\omega(\omega + i\gamma_{dn}) - C'k^2} + ik \frac{E_0 \varepsilon_0 I_{i0} D}{eZ_{d0}} \frac{\omega_{pd}^2}{\omega(\omega + i\gamma_{dn}) - C'k^2} \\ &\quad - i \frac{n_{d0} Z_{d0} k}{m_d} \left[\frac{DI_{i0} K e^2 / 4\pi a \varepsilon_0 T_e}{\omega(\omega + i\gamma_{dn}) - C'k^2} + \frac{\chi_i (J - H u_{i0} / V_{Ti} n_{i0})}{\omega(\omega + i\gamma_{dn}) - C'k^2} \right]. \end{aligned} \quad (6.21)$$

Thus, a linear dispersion relation can finally be assembled from Eqs. (6.7), (6.9), and (6.21). As shown on the right hand side of Eq. (6.21), the charge variation effect consists of several independent parts: the pure plasma flux (the first term), the plasma flux coupled to the electric field (the third term), and the plasma flux coupled to the ion-drag-

force fluctuation (the first term in the square brackets). The additional terms shown in the square brackets represent the contribution from the ion drag force combined with the charge variation and the dust temperature, which has been neglected in previous work as discussed in section 6.2.

It is easily observed that for very small D , the charge variation can be ignored; in this case, for no ion-drag-force fluctuation ($K = J = H = 0$), the susceptibility of the dust particle will be similar to the results presented by Rosenberg *et al* (Rosenberg *et al* 2008) and Yaroshenko *et al* (Yaroshenko *et al* 2009). However, unlike previous papers, a universal expression for dust particles residing either the gaseous, liquid, or solid state, is presented here.

When the dust temperature effect is negligible ($C' \sim 0$) and the ion-drag-force fluctuation terms can be neglected ($K = J = H = 0$), the susceptibility of the dust particle is similar to results presented by Fortov *et al* (Fortov *et al* 2000b) and Ivlev and Morfill (Ivlev and Morfill 2000). Rather than use an OML approach, a more reasonable ion current to the dust surface, resulting from a shifted Maxwellian ion velocity distribution (DML), which is representative of the majority of laboratory dusty plasma experiments to date, is used here.

Finally, in the simplest case, when the effects of the dust temperature and charge variation are both negligible and again ignoring the ion-drag-force fluctuation on the dust particles as well, i.e., $D = C' = K = J = H = 0$, the dispersion relation reduces to that presented by Joyce *et al* (Joyce *et al* 2002):

$$1 + \frac{1}{(k\lambda_{De})^2} - \frac{\omega_{pi}^2}{(\omega - u_{i0}k + i\gamma_{in})(\omega - ku_{i0}) - k^2T_i/m_i} - \frac{\omega_{pd}^2}{\omega(\omega + i\gamma_{dn})} = 0. \quad (6.22)$$

In the following sections, ω_0 will denote the solution of Eq. (6.22) for corresponding wave number k .

The remainder of this Chapter will investigate the effect that the dust temperature, charge variation, and ion-drag-force fluctuation can have on the dispersion relation of the DAW. The neutral drag effect, which mainly contributes to the damping of the DAW, will be ignored.

6.5. Analysis and Discussion

6.5.1. The Dust Temperature Effect ($D = 0, K = J = H = 0$)

The dust temperature effect is discussed first, $D = 0$, assuming that the ion-drag-force fluctuation can also be ignored, i.e., $K = J = H = 0$. In this case, the DAW dispersion relation equation becomes:

$$1 + \frac{1}{(k\lambda_{De})^2} - \frac{\omega_{pi}^2}{(\omega - u_{i0}k + i\gamma_{in})(\omega - ku_{i0}) - k^2 T_i / m_i} - \frac{\omega_{pd}^2}{\omega(\omega + i\gamma_{dn}) - C'k^2} = 0. \quad (6.23)$$

As discussed in section 6.4.2, C' represents the dust pressure and is a function of both the dust temperature T_d and the lattice parameter κ . Figure 6.2 shows that C' , for a dust cloud consisting of dust particles having radii of $3.25 \mu\text{m}$ and density 1.51 g/cm^3 , exhibits a minimum value when T_d reaches a critical value, $T_{d(crit)}$. Figure 6.3 shows the dependency of this critical value on the lattice parameter κ . In this case, the particle charge is assumed to be $-10^4 e$ and the mean interparticle spacing is fixed to be $300 \mu\text{m}$. For a fixed value of C' the fact that there are two solutions for the dust temperature (for example, as indicated in Fig. 6.2, when $C' = 2.59 \times 10^{-3} \text{ m}^2/\text{s}^2$ and $\kappa = 1$ where $T_d = 350 \text{ eV}$ and 10 eV), suggests that it is possible the dispersion relationship for the fluid-like

state (i.e., high dust temperatures) is related to one of the wave modes often seen in crystalline structures (i.e., low dust temperatures) (Ratynskaia *et al* 2004; Yaroshenko *et al* 2004; Khrapak *et al* 2003a; Piel *et al* 2006). Both solutions have been recently observed experimentally: a) at high dust temperatures in ($T_d \sim 300$ eV) experiments (Thomas E 2010) where the dust particles were treated as an ideal gas, and b) for strong electrostatic particle interactions ($T_d \sim 0.03$ eV) in experiments (Yaroshenko *et al* 2010; Nosenko *et al* 2009) in which the dust particles were shown to be strongly coupled to their neighbors through electrostatic interactions.

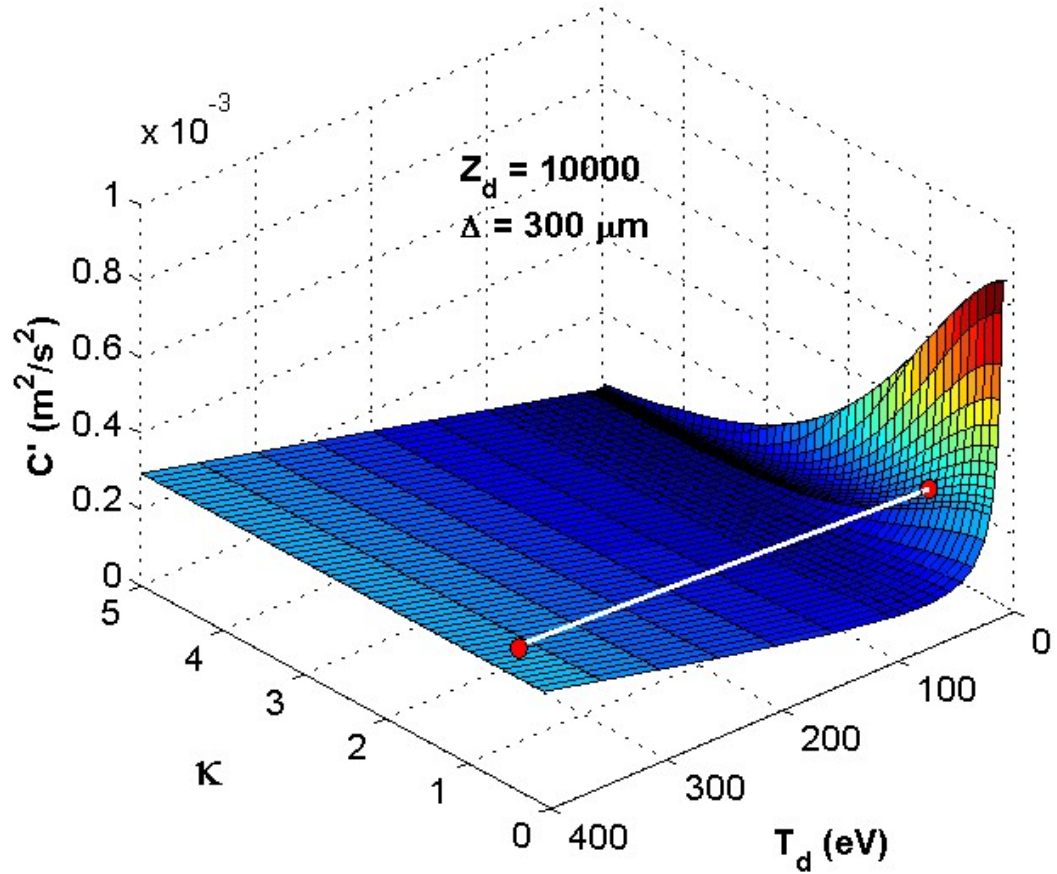


FIG. 6.2. C' as a function of the dust temperature and lattice parameter as given by Eq. (6.13). It can be seen that C' has a minimum value when the dust temperature reaches a critical point. The white line denotes $C' = 2.59 \times 10^{-3} \text{ m}^2/\text{s}^2$ when $\kappa = 1$, and the red dots denote the two corresponding solutions for T_d , i.e., 350 eV and 10 eV.

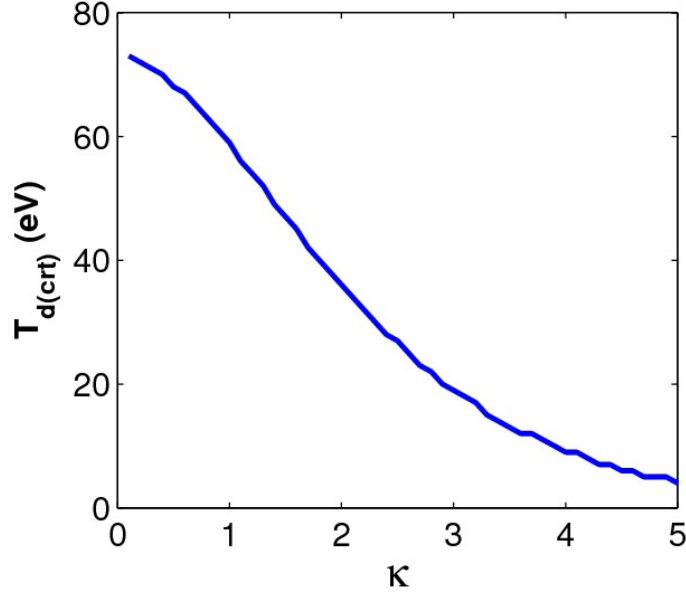


FIG. 6.3. Critical dust temperature which minimizes C' as a function of the lattice parameter.

Figure 6.4 shows results obtained from the DAW dispersion relation via Eq. (6.23) for dust particles having radii of $3.25 \mu\text{m}$ and dust temperatures falling between 0.01 eV and 300 eV. In this case, the interparticle spacing is fixed to be $300 \mu\text{m}$, the ion density is assumed to be $1 \times 10^{14} \text{ m}^{-3}$, and the gas pressure is 200 mTorr. According to Eqs. (6.1) - (6.6), the charge on a single particle under these conditions is calculated to be $-9924 (e)$, the electric field is 1561 V/m, the ion drift velocity is 652.6 m/s, the ratio of ion drag force to gravitational force is 0.17, and the dust plasma frequency is 107.8 rad/s. For this case, the critical dust temperature is $T_{d(crit)} = 29.03 \text{ eV}$. The DAW frequencies shown are normalized by ω_0 , as calculated using Eq. (6.22), to allow changes due to charge variation, dust temperature, and ion-drag-force fluctuation to be more easily seen. As shown, when the dust temperature effect is considered alone, the wave frequency decreases until a critical value of the dust temperature $T_{d(crit)} = 29.03 \text{ eV}$ is reached and then increases significantly as the dust temperature continues to increase. The resulting

frequency difference is most apparent in the short wavelength region ($k \geq 25 \text{ cm}^{-1}$, i.e., $k\lambda_D \geq 0.3$) where the dispersion relation for the DAW at the lowest and highest dust temperatures examined are similar, due to the two solutions that arise for the dust temperature at a specific C' as discussed above.

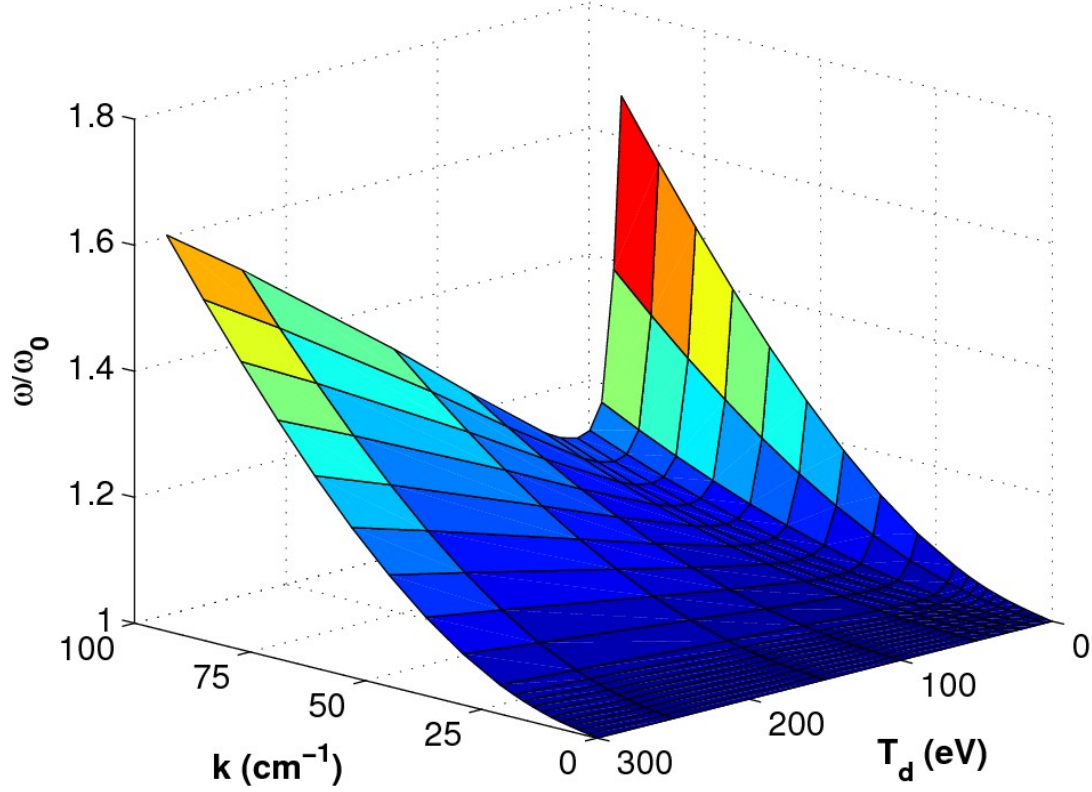


FIG. 6.4. The normalized dispersion relation for a DAW for dust particles at different dust temperatures. The solutions calculated from Eq. (6.23) are normalized using the solutions from Eq. (6.22).

6.5.2. The Charge Variation Effect ($C' = 0, K = J = H = 0$)

Next, the charge variation effect on the DAW dispersion relation was examined. In this case, the dust temperature effect is ignored and the ion drag force is fixed over a set of specified plasma parameters. Thus, $C' = 0, K = J = H = 0$ and the dispersion relation is determined by:

$$1 + \frac{1}{(k\lambda_{De})^2} - \frac{\omega_{pi}^2}{(\omega - u_{i0}k + i\gamma_{in})(\omega - ku_{i0}) - k^2T_i / m_i} - DI_{i0}n_{d0} - \frac{\omega_{pd}^2}{\omega(\omega + i\gamma_{dn})} + ik \frac{E_0 \varepsilon_0 I_{i0} D}{eZ_{d0}} \frac{\omega_{pd}^2}{\omega(\omega + i\gamma_{dn})} = 0. \quad (6.24)$$

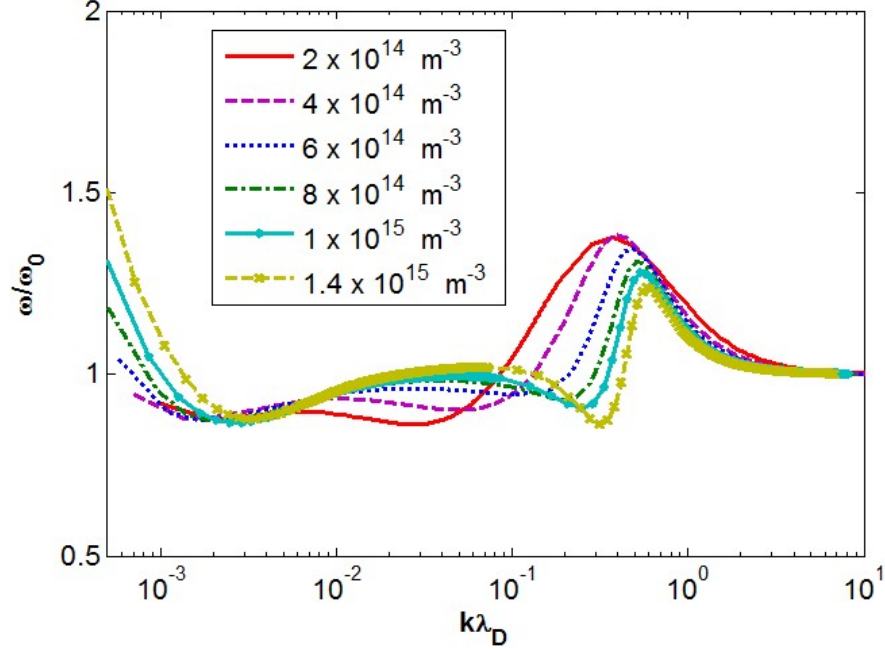


FIG. 6.5. The normalized DAW dispersion relation considered under dust charge variation alone. The lines denote results for ion densities $n_i = 2, 4, 6, 8, 10$, and $14 (\times 10^{14} \text{ m}^{-3})$, respectively. The data shown are solutions for Eq. (6.24) and are normalized using the solutions from Eq. (6.22).

Figure 6.5 shows the dispersion relation that results from Eq. (6.24) for a DAW in a dust cloud having an average interparticle spacing of $200 \mu\text{m}$, an ion density of $n_i = 2, 4, 6, 8, 10, 14 (\times 10^{14} \text{ m}^{-3})$ and a neutral gas pressure of 200 mTorr . In this case, the effect the charge variation has on ω/ω_0 is strongly dependent on the ion density and the wavelength region. As shown in Fig. 6.5, in the extremely long wavelength region ($k\lambda_D \leq 10^{-3}$), the charge variation effect becomes significant, strengthening as the ion density increases and rapidly decreasing as the wavelength decreases. However, in the long wavelength region ($10^{-3} \leq k\lambda_D \leq 10^{-1}$), the frequency remains almost constant; upon

reaching the short wavelength region ($10^{-1} \leq k\lambda_D \leq 1$), the frequency increases slowly before reaching a maximum value, after which it gradually decreases, becoming negligible in the extremely short wavelength limit ($k\lambda_D > 3$).

6.5.3. The Ion-Drag-Force Fluctuation Effect ($C' = 0, D = 0$)

Thirdly, the effect that the ion-drag-force fluctuation has on the DAW dispersion relation is examined. In this case, $C' = 0, D = 0$ and the dispersion relation of the DAW can be obtained employing the equation:

$$1 + \frac{1}{(k\lambda_{De})^2} - \frac{\omega_{pi}^2}{(\omega - u_{i0}k + i\gamma_{in})(\omega - ku_{i0}) - k^2 T_i / m_i} - \frac{\omega_{pd}^2}{\omega(\omega + i\gamma_{dn})} - i \frac{n_{d0} Z_{d0} k}{m_d} \frac{\chi_i (J - H u_{i0} / v_{Ti} n_{i0})}{\omega(\omega + i\gamma_{dn})} = 0. \quad (6.25)$$

Figure 6.6 again shows a dust cloud under identical conditions as those described earlier for ion densities of $n_i = 2, 4, 6, 8, 10, 14 (\times 10^{14} \text{ m}^{-3})$. In this case, the normalized frequency of the DAW remains almost constant across the long wavelength region ($k\lambda_D < 0.1$), but slowly increases as the wavelength decreases until it reaches a maximum value at $k\lambda_D \sim 0.1-0.2$. The ion-drag-force fluctuation effect strengthens significantly as the ion density increases, which is to expected since the ion drag force amplitude increases with ion density as shown in Eq. (6.2). Similar to the effect created by the charge variation, the ion-drag-force fluctuation effect becomes negligible in the short wavelength limit ($k\lambda_D > 1$). It is important to note that the ion-drag-force fluctuation effect can become comparable to or even larger than the charge variation effect when the ion drag force is beyond 20% of gravitational force in the region $k\lambda_D > 0.02$.

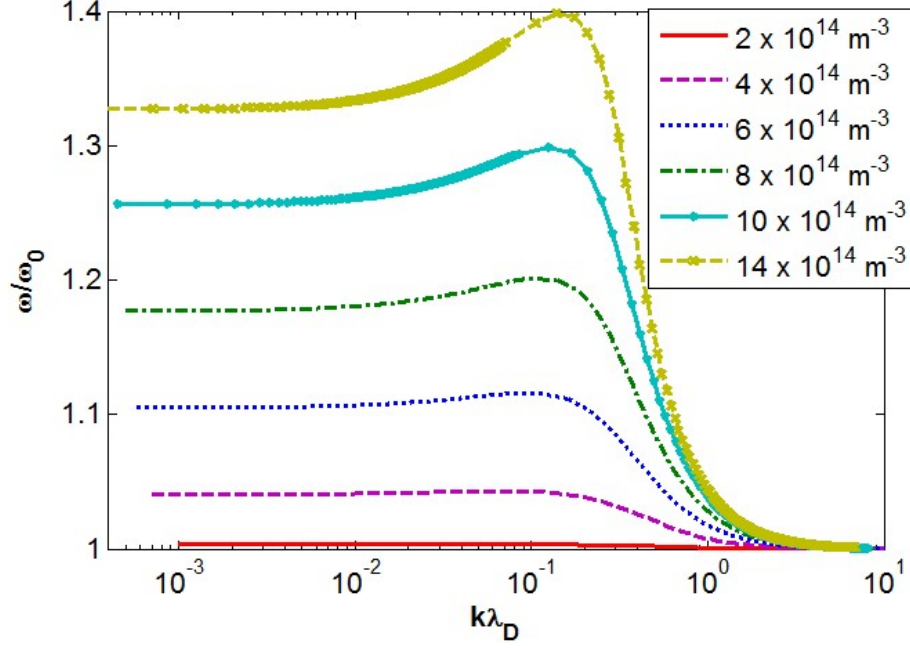


FIG. 6.6. The normalized dispersion relation for the DAW, considering the ion-drag-force fluctuation effect. The data shown are for ion densities $n_i = 2, 4, 6, 8, 10, 14 (\times 10^{14} \text{ m}^{-3})$, respectively and are the solutions of Eq. (6.25) as normalized by the solutions of Eq. (6.22).

6.5.4. Combination of the Three Effects

Finally, the combination of all three effects is considered. The dispersion relationship in this case is determined by the susceptibility equation:

$$\begin{aligned}
 1 + \frac{1}{(k\lambda_{De})^2} - \frac{\omega_{pi}^2}{(\omega - u_{i0}k + i\gamma_{in})(\omega - ku_{i0}) - k^2 T_i / m_i} - DI_{i0}n_{d0} \\
 - \frac{\omega_{pd}^2}{\omega(\omega + i\gamma_{dn}) - C'k^2} + ik \frac{E_0 \epsilon_0 I_{i0} D}{eZ_{d0}} \frac{\omega_{pd}^2}{\omega(\omega + i\gamma_{dn}) - C'k^2} \\
 - i \frac{n_{d0} Z_{d0} k}{m_d} \left[\frac{DI_{i0} K e^2 / 4\pi a \epsilon_0 T_e}{\omega(\omega + i\gamma_{dn}) - C'k^2} + \frac{\chi_i (J - H u_{i0} / v_{Ti} n_{i0})}{\omega(\omega + i\gamma_{dn}) - C'k^2} \right] = 0.
 \end{aligned} \tag{6.26}$$

Once again an identical dust cloud is investigated having ion densities $n_i = 2, 4, 6, 8, 10, 14 (\times 10^{14} \text{ m}^{-3})$. The dust temperature is assumed to be 100 eV. For this case, the calculated dust and plasma parameters, such as the electric field E_0 , the dust charge Z_d ,

the ion flow velocity u_{i0} , and the ion drag force F_{ion}/mg , at the location of the dust particles, are shown in Table 6.1.

Table 6.1. Dust and Plasma Parameters				
$n_i (\times 10^{14} \text{ m}^{-3})$	$E_0 \text{ (V/m)}$	$Q \text{ (-e)}$	$u_{i0} \text{ (m/s)}$	F_{ion}/mg
2	8400	1593	1768	0.004
4	4300	3170	1218	0.028
6	3100	4708	1005	0.088
8	2600	6185	903	0.194
10	2300	7573	837	0.298
14	1950	9977	754	0.465

Figure 6.7 shows the normalized dispersion relationship for DAWs in plasmas having ion densities $n_i = 2, 4, 6, 8, 10, 14 (\times 10^{14} \text{ m}^{-3})$ and a gas pressure at 200 mTorr. For the purpose of comparison, the contribution of each individual effect considered alone is included in each graph. As shown, the three effects play varying roles depending on the wavelength region and ion density. For example, the effect of the dust temperature is negligible in the long wavelength region $k\lambda_D < 0.2$; however, it increases significantly as the wavelength decreases and dominates in the extremely short wavelength regions $k\lambda_D > 1$ for all cases. In the transition zone (i.e., the short wavelength region $0.1 < k\lambda_D < 1$), the three effects are comparable for ion densities above $8 \times 10^{14} \text{ m}^{-3}$ where the ion drag force is at least 20% of the gravitational force. For this case, the ion-drag-force fluctuation effect dominates in the long wavelength region $0.001 < k\lambda_D < 0.1$; however, it becomes negligible across all wavelength regions when the amplitude is smaller than 10% that of gravity. Finally, in the extremely long wavelength region, $k\lambda_D$

< 0.001 , any variation in charge will dominate the behavior, while in the extremely short wavelength region ($k\lambda_D > 1$) both the charge variation and the ion-drag-force effect weaken rapidly as the wavelength increases.

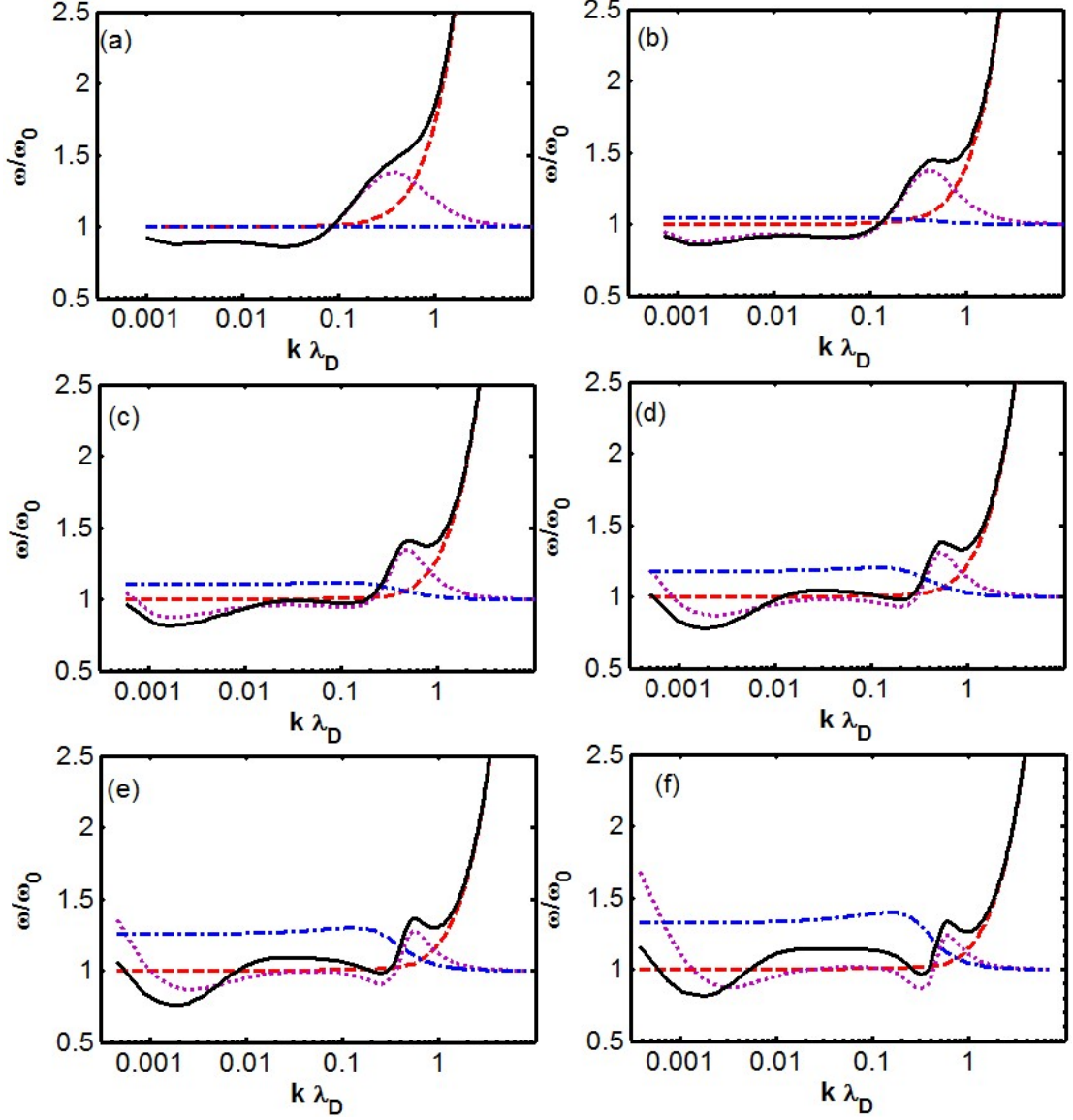


FIG. 6.7. The normalized dispersion relationship for a DAW considering changing dust temperature, charge variation, and ion-drag-force fluctuations in a plasma with ion densities $n_i =$ (a) 2, (b) 4, (c) 6, (d) 8, (e) 10, (f) 14 ($\times 10^{14} \text{ m}^{-3}$). The red dashed, purple dotted and blue dot-dash lines denote the solutions of Eq. (6.23), Eq. (6.24), and Eq. (6.25) as normalized by the solutions of Eq. (6.22), respectively. The solid black line represents the result of considering all three effects together, i.e., the solutions of Eq. (6.26) as normalized by the solutions of Eq. (6.22)

6.5.5. Comparison with Experiments

To verify the theoretical model proposed, the results given above were compared to recent experiments reported by Williams *et al* (Williams *et al* 2008). In these experiments, waves were observed in a suspension of silica microspheres having diameters of $1.5 \mu\text{m}$ and densities $2,000 \text{ kg/m}^3$ in the 3DPX device. Plasma parameters were measured using a double tipped Langmuir probe and determined to be $n_i \approx 5 \times 10^{13} \text{ m}^{-3}$, $T_i \approx 0.025 \text{ eV}$, $\lambda_D \approx 166 \mu\text{m}$ and $T_e \approx 3 \text{ eV}$. Two dust clouds with number densities of (a) $8.05 \times 10^9 \text{ m}^{-3}$ and (b) $1.35 \times 10^{10} \text{ m}^{-3}$ were examined under gas pressures of (a) 72 mTorr and (b) 70 mTorr, respectively. Employing the probe-measured plasma parameters given by Williams *et al*, Eqs. (6.1)-(6.6) yields $E_0 \approx 110 \text{ V/m}$, $Z_d \approx 3063$, $u_{i0} \approx 188 \text{ m/s}$, and $\omega_{pd} \approx 246 \text{ rad/s}$ for dust cloud (a); and $E_0 \approx 125 \text{ V/m}$, $Z_d \approx 2575$, $u_{i0} \approx 215.7 \text{ m/s}$, and $\omega_{pd} \approx 268 \text{ rad/s}$ for dust cloud (b).

Comparison of these theoretical results to the reported experimental data shows the calculated ion flow velocity to be smaller than the one reported for Williams's experiment. Comparison of the calculated charge shows this smaller ion flow velocity to be reasonable: in Williams's calculation, traditional OML theory was employed, while OML with ion drift theory (DML) was employed here. The comparable values of charge seen in both methods imply the ion flow velocity should indeed be smaller than the thermal velocity ($v_{Ti} \approx 246 \text{ m/s}$).

Figures 6.8 (a) and (b) provide a comparison between the experimental results referenced and the theoretical results obtained here. Our theory requires a value of $T_d = 100 \text{ eV}$ to best fit the experimental data for cloud (a) and a $T_d = 200 \text{ eV}$ to best fit the experimental data for cloud (b). In both cases, these values are smaller than those

reported experimentally (275 eV and 400 eV). This discrepancy in required dust temperature results from the different flow velocities used, different dust temperature model employed (i.e., an ideal gas model in Williams *et al*'s, while a comprehensive one used here), and inclusion of the effects of charge variation and ion-drag-force fluctuation. These factors considered are important: first, the effects of charge variation and ion-drag-force fluctuation were assumed to be negligible in Williams *et al*, however there was not enough evidence to show that this assumption was valid; second, the dust particles in the dust cloud were expected to interact with each other through a Coulomb force, and thus the ideal gas model for the dust pressure was questionable. Through the calculation done here for these cases, it is verified that the dust temperature is the dominant factor affecting the dispersion relationship for the DAW. This domination can be more easily seen in Fig. 6.9 in which the contribution from the effects of the charge variation and ion-drag-force fluctuation are shown to be less than 10% in the wavelength region considered.

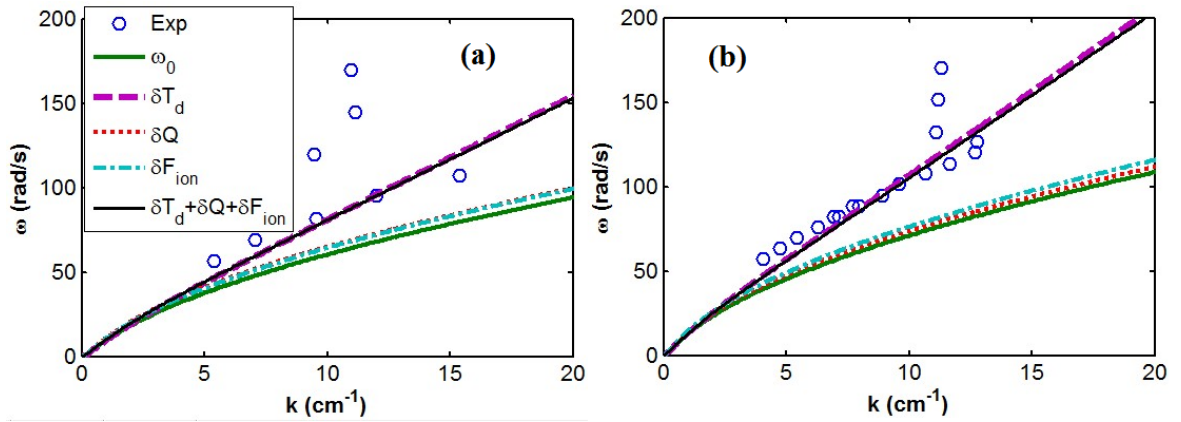


FIG. 6.8. Comparison between the theoretical results obtained in this work and Williams *et al*'s experimental data (Williams *et al* 2008). These theoretical results require values of $T_d = 100$ eV and 200 eV in order to provide a best fit to the experimental data from cloud (a) and (b) respectively. The green solid lines denote the traditional dispersion relationship as given in Eq. (6.22). The dashed purple, dotted red and dash-dotted blue lines denote the results obtained when each effect is considered alone. The black solid lines provide the best theoretical fit considering all three effects together.

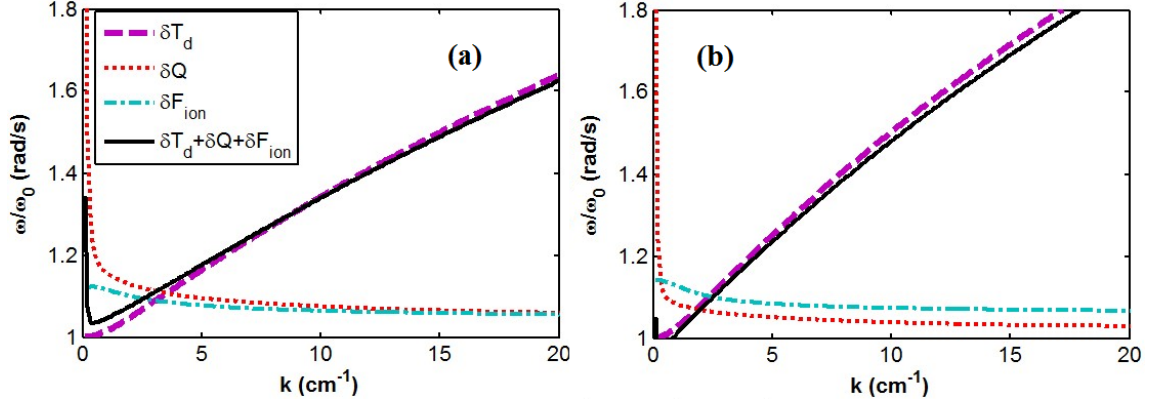


FIG. 6.9. The normalized dispersion relationship for a DAW under the conditions observed in Williams *et al*'s experiments for dust cloud *a* (a) and dust cloud *b* (b). It is noticed that in the wavelength region considered ($5 \text{ cm}^{-1} < k < 20 \text{ cm}^{-1}$) the effect of the dust temperature dominates on the dispersion relationship for the DAW.

6.5.6. Growth and Damping of a DAW

The growth and damping of a DAW are generally related to the imaginary part of the frequency or wave number. In this section, the role that the charge variation, dust temperature, and ion-drag-force fluctuation play on the growth and damping of a DAW is discussed.

Since the wave frequency and wave number are both complex, they can be written in the form $\omega = \omega_r + i\omega_i$ and $k = k_r + ik_i$. For the following, the instability of the DAW in the time domain is examined, thus $k_i = 0$. For $\omega_i > 0$, the wave is growing; on the other hand, the wave will be damped when $\omega_i < 0$. To simplify the problem, a few additional assumptions are necessary: (1) $\omega_i \ll \omega_r$; (2) weak neutral damping $\gamma_{dn} \ll \omega_r$; (3) weak ion-neutral collision $\gamma_{in} \ll ku_{i0}$. In this case, the traditional susceptibility as given in Eq. (6.22) can be written as

$$1 + \frac{1}{(k\lambda_{De})^2} + \frac{\omega_{pi}^2}{k^2(v_{ti}^2 - u_{i0}^2)} - \frac{\omega_{pd}^2}{\omega^2} = 0. \quad (6.27)$$

The solution of the real part of the frequency for Eq. (6.27) is

$$\omega_r = \frac{\omega_{pd} k \Lambda_D}{(1 + k^2 \Lambda_D^2)^{1/2}}, \quad (6.28)$$

where

$$\Lambda_D = \left[\frac{1}{\lambda_{De}^2} + \frac{\omega_{pi}^2}{v_{Ti}^2 - u_{i0}^2} \right]^{-1/2}. \quad (6.29)$$

In the low ion flow limit, $u_{i0} \ll v_{Ti}$, $\Lambda_D = \lambda_{De}$. Assuming the real part of the frequency is close to that given by the DAW dispersion relation (Eq. (6.26)) (Fortov et al 2000b), only the influence of the effects on the imaginary part of the frequency will be examined.

Pure Charge Variation. To consider the role a pure charge variation plays, only the first term on the RHS of Eq. (6.21) is required. In this case, the susceptibility equation now becomes

$$1 + \frac{1}{(k \Lambda_D)^2} - \frac{\omega_{pd}^2}{\omega^2} - D I_{i0} n_{d0} = 0. \quad (6.30)$$

Employing the solution for the real part of the frequency provided by Eq. (6.28), the imaginary part of the frequency can now be obtained by solving Eq. (6.30):

$$\omega_i = -\frac{1}{2} \frac{\omega_r^4}{\eta^2 \omega_{pd}^2} \frac{I_{i0} n_i}{k^2} \left(\frac{F}{\lambda_{Di}^2 n_i} + \frac{1}{\lambda_{De}^2 n_e} \right), \quad (6.31)$$

where F is positive and is expressed by Eq. (6.18). Thus, $\omega_i < 0$ indicates that a pure charge variation leads to a damping of the DAW, in agreement with the conclusions drawn by Fortov *et al* (Fortov et al 2000b).

Charge Variation Combined with Electric Force. In this case, the charge variation is included within the electric force. Thus, considering the effect of the charge variation combined with the electric force, the equation can be written as

$$1 + \frac{1}{(k\Lambda_D)^2} - \frac{\omega_{pd}^2}{\omega^2} + ik \frac{E_0 \epsilon_0 I_{i0} D}{e Z_{d0}} \frac{\omega_{pd}^2}{\omega^2} = 0. \quad (6.32)$$

The solution of Eq. (6.32) yields

$$\omega_i = \frac{\omega_r}{2\eta} \frac{E_0 \epsilon_0 I_{i0}}{e Z_0 k} \left(\frac{F}{\lambda_{Di}^2 n_i} + \frac{1}{\lambda_{De}^2 n_e} \right). \quad (6.33)$$

It can be seen that $\omega_i > 0$, indicating that the charge variation when combined with the electric force can create instabilities in the DAW, which again agrees with Fortov *et al* (Fortov et al 2000b).

Charge Variation Combined with the Ion Drag Force. In Eq. (6.19), the charge variation is seen to be coupled to the ion-drag-force fluctuation. Taking this coupling into account and including the effect of the charge variation in combination with the ion drag force, the solution of the equation of dispersion relation can be expressed as

$$1 + \frac{1}{(k\Lambda_D)^2} - \frac{\omega_{pd}^2}{\omega^2} - i \frac{kD}{\omega^2} K \frac{I_{i0} n_{d0} Z_{d0} e^2}{4\pi a \epsilon_0 m_d T_e} = 0. \quad (6.34)$$

For this case, the imaginary part of the frequency is solved to be

$$\omega_i = -\frac{\omega_r}{2\eta} \frac{K I_{i0}}{4\pi a T_e Z_0 k} \left(\frac{F}{\lambda_{Di}^2 n_i} + \frac{1}{\lambda_{De}^2 n_e} \right) \quad (6.35)$$

where K is positive and represented by Eq. (6.20). Thus, for $\omega_i < 0$, the effect of the charge variation combined with the ion drag force again leads to a damping of the DAW.

Pure Ion Drag Force. Finally, the pure ion drag force effect is considered. In this case, the equation for the dispersion relation can be written as

$$1 + \frac{1}{(k\Lambda_D)^2} - \frac{\omega_{pd}^2}{\omega^2} - i \frac{k\chi_i}{\omega^2} \frac{n_{d0}Z_{d0}(J - H u_{i0}/v_{Ti}n_{i0})}{m_d} = 0. \quad (6.36)$$

As above, the solution gives

$$\omega_i = \frac{Z_0 n_{d0}}{2\omega_{pd}\lambda_D m_d (1 + k^2 \lambda_D^2)^{1/2}} \left(J - H \frac{u_{i0}}{v_{Ti} n_{i0}} \right). \quad (6.37)$$

It is found that $J - H u_{i0}/v_{Ti} n_{i0} > 0$; thus, $\omega_i > 0$, and the effect of the pure ion drag force fluctuation is to cause the DAW to grow.

6.6. Conclusions

In this Chapter, the dispersion relations for DAWs were examined theoretically, using a fluid model analysis. The dust temperature effect, the charge variation effect, and the ion-drag-force fluctuation effect were all considered independently and together. It was shown that dust particles in strongly coupled, cold crystalline structures (i.e., low dust temperatures) and fluid-like active states (i.e., high dust temperatures) exhibit similar dispersion behavior. Employing a dispersion relationship calculation, it was shown that the charge variation, ion-drag-force fluctuation and dust temperature all play different roles depending on the wavelength regime. Over the short wave length region ($0.1 < k\lambda_D < 1$), these three effects are comparable and the ion-drag-force fluctuation effect cannot be ignored when its amplitude is close to or above 20% that of the gravitational force. To verify these theoretical results, the calculated values for the dispersion relationship were compared to recent experimental data (Williams *et al* 2008) and shown to be in excellent agreement. Finally, it was shown that the pure ion-drag-force fluctuation and charge

variation, when combined with the electric force, can contribute to the growth of DAW instabilities, while the pure charge variation and charge variation combined with ion-drag-force fluctuation lead to a damping of the DAW. The model given above provides a much more comprehensive understanding of the dispersion relationships and instabilities of the DAW, giving a clearer view of the regions in which these different effects have different weight. This should be of great importance for future experimental interpretation of waves in dusty plasma.

CHAPTER SEVEN

Summary and Future Work

In a dusty plasma, nano or micro scale particles act as additional charged species. A proper understanding of the role that dust particles play in both the universe and in industrial plasma applications, requires a solid understanding of the fundamental properties of a dusty plasma. This thesis has focused on the fundamental dynamics of dust particles in dusty plasmas, in particular the particle-particle interaction, one dimensional particle chains, and dust acoustic waves.

The first portion of the thesis investigated the particle-particle interaction within an RF plasma by examining collisions of two micron-sized MF particles conducted in a modified GEC reference RF cell within the HIDPL at CASPER. In comparison to previous work employing probes, lasers, or waves, etc., a minimal perturbation technique called a “single particle drop” was developed to allow detection of the horizontal confinement and the particle-particle interaction. This technique was shown to be a convenient and reliable approach for quickly determining both the particle charge and the screening length. The horizontal confinement provided by a cutout plate placed on the lower powered electrode was shown to be parabolic over a large range of spatial parameters and to be dependent on the discharge gas pressure. The measured particle-particle interaction was shown to be well fit by a screened Coulomb potential and to decrease with increasing pressure. It was also shown that the resulting particle charge number and screening length both decrease with increasing pressure. A charging model

previously employed to describe a DC system was for the first time shown to successfully model our RF system.

The second part of this thesis presented data describing particle chain structures and self-excited dust acoustic waves produced in small and large glass box containers. It was shown that under appropriate conditions a single dust particle chain can be formed within a small glass box with the number of particles in the chain controlled through adjustment of the discharge power and gas pressure. The oscillation spectra of the particles comprising the chain were investigated, including the resonance frequencies, the neutral drag coefficients, and the oscillation amplitudes and phases. It was determined that under certain conditions the particles within the chain divided into two groups, each exhibiting differing oscillation spectra.

One possible reason for this behavior is associated with the ion drag force, which is directed along the chain orientation. A dispersion relation for a DAW within the lower group was experimentally examined and shown to agree with theory. In a larger glass box, self-excited DAWs were shown to be generated by decreasing the gas pressure or increasing the discharge power. Two approaches were used to obtain this analysis, the space-time diagram and the power spectrum. Both the frequencies and wave numbers of the DAWs produced were shown to increase with discharge power and gas pressure. The DAWs were also seen to be highly nonlinear and the development of this nonlinearity was analyzed. Employing the single particle drop technique developed earlier, the electric force profile for a single particle was visualized. The coincidence of the non-zero electric force and the initial point of wave growth indicated that the non-zero electric force may be a cause for the occurrence of the self-excited DAWs. The interaction

between external bias modulation and self-excited DAWs was also examined, and the phenomenon of both mixing waves and wave-synchronization depending on the frequencies was observed.

The final part of the thesis provided a theoretical derivation designed to determine the effect that the dust temperature, the charge variation, and the ion-drag-force fluctuation has on the dispersion relationship of a DAW. A closed set of equations was derived and then applied in order to calculate the corresponding dust and plasma parameters. The model, which has the ability to represent the dust pressure for the gaseous, liquid, and solid states, was initially employed to investigate the dust temperature effect. It was determined that the dispersion relationship for DAWs in dust clouds with dust particles in a cold crystalline structure (i.e., low dust temperatures) and in an active liquid phase (i.e., high dust temperatures) have similar behaviors. The relative contribution from these three effects on the dispersion relationship for a DAW strongly depends on the wavelength region and ion density. For example, in the short wavelength ($k\lambda_D > 1$), the effect of dust temperature dominates, with the contributions from the charge variation and ion-drag-force fluctuation being negligible. It is important to note however, that the effect of the ion-drag-force fluctuation is noticeable when its amplitude is close to or above 20% that of the gravitational force. A comparison between our model and recent experiments showed good agreement. It was also shown that the pure charge variation and charge variation combined with the ion-drag-force fluctuation led the DAW to be damped, while the pure ion-drag-force fluctuation and charge variation combined with the electric force plays a role in causing the growth of wave instability.

The model developed provides a comprehensive understanding of DAWs in a dusty plasma, presenting a clear view of the regions where different effects have different weight. This should prove to be helpful for experimental interpretation of waves in dusty plasma.

There are several possible future investigations that could be conducted to expand on the results provided above. Additional experiments are already planned using the GEC RF reference cells within the HIDPL to continue the examination begun in this work on particle-particle interactions, glass box confinements, and wave dynamics.

Among these, the investigation of the particle-particle interaction should be extended to verify possible attractive forces (Ignatov 2003; Lampe *et al* 2000; Khrapak *et al* 2001; Tsytovich *et al* 1998). This might be possible through reduction of the background noise, although this would require a much quieter experimental environment.

Particle behavior for various locations within the glass box confinement should also be examined in greater detail. Currently, this phenomenon is assumed due to the confinement potential provided by the glass box. Although a better understanding of this confinement potential was reported in this thesis, the confinement potential for various discharge conditions is still not well understood.

Finally, in order to better understand dust acoustic waves, additional experiments examining the dispersion relation for dust acoustic waves need to be conducted for comparison with the model reported here. This is particularly true for cases when the effects of the charge variation and/or the ion-drag-force fluctuation are larger than those established by the dust temperature.

BIBLIOGRAPHY

- Allen, J.E., “Probe theory: the orbital motion approach”, *Phys. Scripta* 45, 497–503, 1992.
- Allen, J.E., Annaratone, B.M., de Angelis, U., “On the orbital motion limited theory for a small body at floating potential in a Maxwellian plasma”, *J. Plasma Phys.* 63, 299–309, 2000.
- Angelis U., and A. Forlani, “Grain charge in dusty plasmas”, *Phys. Plasmas*. 5, 3068, 1998.
- Arp, O., Block, D., and Piel, A., “Dust Coulomb Balls: Three-Dimensional Plasma Crystals”, *Phys. Rev. Lett.* 93, 165004, 2004.
- Arp, O., D. Block, M. Klindworth, and A. Piel, “Confinement of Coulomb balls”, *Phys. Plasmas* 12, 122102, 2005.
- Barge, L. B., “Charging Processes and Effects in a Coupled Dusty Plasma”, *Dissertation*, 1998.
- Barkan, A., D’Angelo, N., Merlino, R.L., “Charging of dust grains in a plasma”, *Phys. Rev. Lett.* 73, 3093–3096, 1994.
- Barkan, A., Merlino, R.L., and D’Angelo, N., “Laboratory Observation of the Dust Acoustic Wave Mode”, *Phys. Plasmas* 2, 3563, 1995.
- Barnes, M.S., Keller, J.H., Forster, J.C., O’Neill, J.A., Coultas, D.K., “Transport of dust particles in glow-discharge plasmas”, *Phys. Rev. Lett.* 68, 313–316, 1992.
- Basner, R., F. Sigeneger, D. Loffhagen, G. Schubert, H. Fehske, and H. Kersten, New J. Particles as probes for complex plasmas in front of biased surfaces, *Phys.* 11, 013041, 2009.
- Bittencourt, J. A., “Fundamentals of Plasma Physics”, Pergamon, New York, 1986.
- Bohm, D., “Minimum ionic kinetic energy for a stable sheath” in “The Characteristics of Electrical Discharges in Magnetic Field”, edited by A. Guthrie and R. K. Wakerling, p. 77, McGraw-Hill, New York, 1949.
- Bouchoule, A., “Dusty plasmas - Physics, Chemistry and Technological Impacts in Plasma Processing”, *John Wiley and Sons Ltd.*, 1999.

- Boufendi, L., and Bouchoule, A., “Industrial developments of scientific insights in dusty plasmas”, *Plasma Sources Sci. Technol.* *11(3A)*, 211-218, 2002.
- Chen, F. F., Chap. 4 in “Plasma Diagnostic Techniques”, edited by R. H. Huddlestone and S. L. Leonard, *Academic*, New York, 1965.
- Chen, F. F., “Introduction to Plasma Physics and Controlled Fusion, Vol. 1: Plasma Physics”, *Second Edition*, *Plenum Press*, 1984.
- Chu, J.H., I, L., “Direct observation of Coulomb crystals and liquids in strongly coupled rf dusty plasmas”, *Phys. Rev. Lett.* *72*, 4009–4012, 1994.
- Creel, J., “Characteristic Measurements within a GEC rf Reference Cell”, *Dissertation*, 2010.
- D’Angelo N., “Dusty plasma ionization instability with ion drag”, *Phys. Plasmas* *5*, 3155–3160, 1998.
- D’Angelo N. and R. L. Merlino, “Current-driven dust-acoustic instability in a collisional plasma”, *Planet. Space Sci., Vol. 44. No. 12*, pp. 1593 -1598, 1996
- Douglass, A., Land, V., Matthews, L., and Hyde, T., “Dust particle charge in plasma with ion flow and electron depletion near plasma boundaries”, *Phys. Plasmas* *18*, 083706, 2011.
- Douglass A., Victor Land, Ke Qiao, Lorin Matthews, and Truell Hyde, “Determination of the levitation limits of dust particles within the sheath in complex plasma experiments”, *Phys. Plasmas* *19*, 013707, 2012.
- Daugherty, J. E., Porteous, R. K., and Graves, D. B., “Electrostatic forces on small particles in low pressure discharges”, *J. Appl. Phys.* *73*, 1617, 1993;
- Eliezer, S., and Eliezer, Y., “The Fourth State of Matter: An Introduction to Plasma Science”, *Second Edition*, *IOP published*, 2001.
- Epstein, P. S., “On the Resistance Experienced by Spheres in their Motion through Gases”, *Phys. Rev.* *23*, 710, 1924.
- Farouki, R.T., Hamaguchi, S., “Thermal energy of crystalline one-component plasma from dynamical simulation”, *Phys. Rev. E* *47*, 4330–4336, 1993.
- Flanagan, T. M. and J. Goree, “Observation of the spatial growth of self-excited dust-density waves”, *Phys. Plasmas* *17*, 123702, 2010.
- Flanagan, T. M. and J. Goree, “Development of nonlinearity in a growing self-excited dust-density wave”, *Phys. Plasmas* *18*, 013705, 2011.

- Fortov, V. E., Nefedov, A. P., Torchinsky, V. M., Molotkov, V. I., Petrov, O. F., Samarian, A. A., Lipaev, A. M., and Khrapak, A. G., “Crystalline structures of strongly coupled dusty plasmas in dc glow discharge strata”, *Phys. Lett. A* 229, 317, 1997.
- Fortov, V. E., A. P. Nefedov, V. A. Sinel’schikov, A. D. Usachev, and A. V. Zobnin, Filamentary dusty structures in RF inductive discharge, *Phys. Lett. A* 267, 179, 2000a.
- Fortov, V. E., A. G. Khrapak, S. A. Khrapak, V. I. Molotkov, A. P. Nefedov, O. F. Petrov, V. M. Torchinsky, “Mechanism of dust–acoustic instability in a current glow discharge plasma”, *Phys. Plasmas* 7, 1374–1380, 2000b.
- Fortov, V. E., A. D. Usachev, A. V. Zobnin, V. I. Molotkov, O. F. Petrov, “Dust–acoustic wave instability at the diffuse edge of radio frequency inductive low-pressure gas discharge plasma”, *Phys. Plasmas* 10, 1199–1207, 2003.
- Fortov, V. E., Petrov, O. F., Usachev, A. D., and Zobnin, A. V., “Micron-sized particle-charge measurements in an inductive rf gas-discharge plasma using gravity-driven probe grains”, *Phys. Rev. E* 70, 046415, 2004a.
- Fortov, V. E., Khrapak, A. G., Khrapak, S. A., Molotkov, V. I., and Petrov, O. F., “Dusty Plasmas”, *Usp. Fiz. Nauk* 174, 495, 2004 [*Phys. Usp.* 47, 447, 2004b].
- Fortov, V. E., Ivlev, A. V., Khrapak, S. A., Khrapaka, A. G., Morfill, G. E., “Complex (dusty) plasmas: Current status, open issues, perspectives”, *Phys. Reports* 421, 1 – 103, 2005.
- Frost L. S., “Effect of Variable Ionic Mobility on Ambipolar Diffusion”, *Phys. Rev.* 105, 354-356, 1957.
- Gozadinos, A. V. Ivlev and J. P. Boeuf, “A fluid model for colloidal plasmas under microgravity G. conditions”, *New J. Phys.* 5 32.1–32.9, 2003.
- Goedheer W. J., V. Land and J. Venema, “Hydrodynamic and kinetic modelling of complex radio-frequency plasmas”, *J. Phys. D: Appl. Phys.* 42 194015, 2009.
- Hamaguchi, S., Farouki, R. T., Dubin, D. H. E, “Triple point of Yukawa systems”, *Phys. Rev. E* 56, 4671–4682, 1997.
- Hargis, P. J., Greenberg, K. E., Miller, P. A., et al. “The gaseous electronic conference radio-frequency reference cell: a defined parallel-plate radio-frequency system for experimental and theoretical studies of plasma-producing discharges”, *Rev. Sci. Instrum.* 65 (1), 140–154, 1994.

- Havnes, O., Aanesen, T. K., and Melandsø, F., “On Dust Charges and Plasma Potentials in a Dusty Plasma With Dust Size Distribution”, *J. Geophys. Res.* **95**, 6581–6585, 1990.
- Hayashi, Y., and Tachibana, S., “Observation of Coulomb-crystal formation from carbon particles grown in a methane plasma”, *Japan. J. Appl. Phys.* **33** L804–L806, 1994.
- Hebner G. A. *et al.*, “Direct Determination of Particle-Particle Interactions in a 2D Plasma Dust Crystal”, *Phys. Rev. Lett.* **87**, 235001, 2001.
- Hebner, G. A., Riley, M. E., and Marder, B. M., “Dynamic probe of dust wakefield interactions using constrained collisions”, *Phys. Rev. E* **68**, 016403, 2003.
- Hebner, G. A., Riley, M. E., “Measurement of attractive interactions produced by the ion wakefield in dusty plasmas using a constrained collision geometry”, *Phys. Rev. E* **68**, 046401, 2003.
- Hebner, G. A., Riley, M. E., “Structure of the ion wakefield in dusty plasmas”, *Phys. Rev. E* **69**, 026405, 2004.
- Hollenstein, Ch, The physics and chemistry of dusty plasma, *Plasma Phys. Control. Fusion* **42**, R93, 2000
- Homann, A., Melzer, A., Peters, S., and Piel, A., “Determination of the dust screening length by laser-excited lattice waves”, *Phys. Rev. E* **56**, 7138–7141, 1997.
- Homann, A., Melzer, A., and Piel, A., “Measuring the charge on single particles by laser-excited resonances in plasma crystals”, *Phys. Rev. E* **59**, R3835–R3838, 1998a.
- Homann, A., Melzer, A., Peters, S., Madani, R., Piel, A., “Laser-excited dust lattice waves in plasma crystals”, *Physics Letters A* **242**, 173–180, 1998b.
- Homann, A., Melzer, A., and Piel, A., “Measuring the charge on single particles by laser-excited resonances in plasma crystals”, *Phys. Rev. E* **59**, R3835, 1999.
- Hone, J., M. Whitney, C. Piskoti, and A. Zettl, “Thermal conductivity of single-walled carbon nanotubes”, *Phys. Rev. B* **59**, R2514, 1999.
- Hörlück, S. and P. Dimon, Statistics of shock waves in a two-dimensional granular flow, *Phys. Rev. E* **60**, 671, 1999.
- Hutchinson, I.H., “Ion collection by a sphere in a flowing plasma: 2. Non-zero Debye length”, *Plasma Phys. Control. Fusion* **45**, 1477–1500, 2003.
- Hutchinson, I.H., “Ion collection by a sphere in a flowing plasma: 3. Floating potential and drag force”, *Plasma Phys. Control. Fusion* **47**, 71–87, 2005.

- Ignatov, A.M., “Interaction between Dust Grains near a Conducting Wall”, *Plasma Physics Reports*, Vol. 29, No. 4, 2003, pp. 296–299. Translated from *Fizika Plazmy*, Vol. 29, No. 4, 2003, pp. 325–328.
- Ikezi, H., “Coulomb solid of small particles in plasmas”, *Phys. Fluids* 29, 1764-1766, 1986.
- Ivlev, A.V., Morfill, G., Fortov, V.E., “Potential of a dielectric particle in a flow of a collisionless plasma”, *Phys. Plasmas* 6, 1416–1420, 1999.
- Ivlev A. V. and G. Morfill, “Acoustic modes in a collisional dusty plasma: Effect of the charge variation”, *Phys. Plasmas* 7, 1094, 2000.
- Ivlev, A.V., Khrapak, S.A., Zhdanov, S.K., Morfill, G.E., Joyce, G., “Force on a charged test particle in a collisional flowing plasma”, *Phys. Rev. Lett.* 92, 205007/1-4, 2004a.
- Ivlev, A.V., Zhdanov, S.K., Khrapak, S.A., Morfill, G.E., “Ion drag force in dusty plasmas”, *Plasma Phys. Control. Fusion* 46, B267–B279, 2004b.
- Ivlev, A.V., Zhdanov, S.K., Khrapak, S.A., Morfill, G.E., “Kinetic approach for the ion drag force in a collisional plasma”, *Phys. Rev. E* 71, 016405/1-7, 2005.
- Joyce G., M. Lampe, and G. Ganguli, “Instability-Triggered Phase Transition to a Dusty-Plasma Condensate”, *Phys. Rev. Lett.* 88. 095006, 2002.
- Khrapak, S.A., Ivlev, A.V., and Morfill, G., “Interaction potential of microparticles in a plasma: role of collisions with plasma particles”, *Phys. Rev. E* 64 046403/1-7, 2001.
- Khrapak, S., D. Samsonov, G. Morfill, H. Thomas, V. Yaroshenko, H. Rothermel, T. Hagl, V. Fortov, A. Nefedov, V. Molotkov, O. Petrov, A. Lipaev, A. Ivanov, Y. Baturin, “Compressional waves in complex (dusty) plasmas under microgravity conditions”, *Phys. Plasmas* 10, 1–4, 2003a.
- Khrapak, S.A., Ivlev, A.V., Morfill, G.E., “Momentum transfer in complex plasmas”, *Phys. Rev. E* 70, 056405/1-9, 2004.
- Khrapak, S.A., Ratynskaia, S.V., Zobnin, A.V., Usachev, A.D., Yaroshenko, V.V., Thoma, M.H., Kretschmer, M., Hebner, H., Morfill, G.E., Petrov, O.F., Fortov, V.E., “Particle charge in the bulk of gas discharges”, *Phys. Rev. E* 72, 016406/1-10, 2005a.
- Khrapak, S. A., Ivlev, A. V., Zhdanov, S. K., and Morfill, G. E., “Hybrid approach to the ion drag force”, *Phys. Plasmas* 12, 042308, 2005b.

- Kittel C., “Introduction to Solid State Physics 7th edition”, *New York: Wiley*, 1996.
- Kong, J., T. Hyde, L. Matthews, K. Qiao, Z. Zhang and A. Douglass, “One-dimensional vertical dust strings in a glass box”, *Phys. Rev. E* **84**, 016411, 2011.
- Konopka, U., Ratke, L., and Thomas, H. M., “Central Collisions of Charged Dust Particles in a Plasma”, *Phys. Rev. Lett.* **79**, 1269–1272, 1997.
- Konopka, U., Morfill, G. E., and Ratke, L., “Measurement of the Interaction Potential of Microspheres in the Sheath of a rf Discharge”, *Phys. Rev. Lett.* **84**, 891, 2000.
- Lampe, M., Joyce, G., Ganguli, G., and Gavrishchaka, V., “Interactions between dust grains in a dusty plasma”, *Phys. Plasmas* **7**, 3851–3861, 2000.
- Lampe, M., Gavrishchaka, V., Ganguli, G., Joyce, G., “Effect of trapped ions on shielding of a charged spherical object in a plasma”, *Phys. Rev. Lett.* **86**, 5278–5281, 2001.
- Lampe, M., Goswami, R., Sternovsky, Z., Robertson, S., Gavrishchaka, V., Ganguli, G., Joyce, G., “Trapped ion effect on shielding, current flow, and charging of a small object in a plasma”, *Phys. Plasmas* **10**, 1500–1513, 2003.
- Land V., Smith, B., Matthews, L., and Hyde T., “Probing the Sheath Electric Field With a Crystal Lattice by Using Thermophoresis in Dusty Plasma”, *Transactions on Plasma Science*, Vol. 38, NO. 4, 2010.
- Lapenta, G., “Simulation of charging and shielding of dust particles in drifting plasmas”, *Phys. Plasmas* **6**, 1442–1447, 1999.
- Lepria, S., P. Sandri, and A. Politi, “The one-dimensional Lennard-Jones system: collective fluctuations and breakdown of hydrodynamics”, *Eur. Phys. J. B* **47**, 549, 2005.
- Liao, Chen-Ting, Lee-Wen Teng, Chen-Yu Tsai, Chong-Wai Io, and Lin I, “Lagrangian-Eulerian Micromotion and Wave Heating in Nonlinear Self-Excited Dust-Acoustic Waves”, *Phys. Rev. Lett.* **100**, 185004, 2008.
- Lifshitz, E.M., L.P. Pitaevskii, “Physical Kinetics”, Pergamon, Oxford, 1981.
- Liu, B., Goree, J., and Nosenko, V., “Radiation pressure and gas drag forces on a melamine-formaldehyde microsphere in a dusty plasma”, *Phys. Plasmas* **10**, 9-20, 2003.
- Liu, B. and J. Goree, “Phonons in a one-dimensional Yukawa chain: Dusty plasma experiment and model”, *Phys. Rev. E* **71**, 046410, 2005.

- McGhee, C. A., *et al.*, “HST observations of spokes in Saturn's B ring”, *Icarus* 173, 508-521, 2005.
- Melzer, A., Trottenberg, T., and Piel, A., “Experimental determination of the charge on dust particles forming Coulomb lattices”, *Phys. Lett. A* 191, 301-308, 1994.
- Melzer, A., Schweigert, V. A., and Piel, A., “Transition from Attractive to Repulsive Forces between Dust Molecules in a Plasma Sheath”, *Phys. Rev. Lett.* 83, 3194, 1999.
- Melzer, A., Schweigert, V. A., and Piel, A., “Measurement of the Wakefield Attraction for “Dust Plasma molecules”, *Physica Scripta. Vol. 61*, 494-591, 2000.
- Melzer, A. and Goree, J., “Fundamentals of dusty plasmas *Low Temperature Plasmas* vol 1” ed R Hippler, H. Kersten, M. Schmidt and K. H. Schoenbach (*New York: Wiley*) pp. 129, 2008.
- Merlino, R. L., A. Barkan, C. Thompson, and N. D’Angelo, “Laboratory studies of waves and instabilities in dusty plasmas”, *Phys. Plasmas* 5, 1607–1614, 1998.
- Merlino R. L., “Dust-acoustic waves driven by an ion-dust streaming instability in laboratory discharge dusty plasma experiments”, *Phys. Plasmas* 16, 124501, 2009.
- Mitchell, C. J., *et al.*, “Saturn's Spokes: Lost and Found.”, *Science* 311, 1587, 2006.
- Molotkov, V.I., A.P. Nefedov, V.M. Torchinskii, V.E. Fortov, A.G. Khrapak, “Dust acoustic waves in a dc glow-discharge plasma”, *JETP* 89, 477–480, 1999.
- Morfill, G. E., and Thomas, H., “Plasma crystal”, *J. Vac. Sci. Technol. A* 14, 490-495, 1996.
- Morfill, G. E., H. M. Thomas, U. Konopka, H. Rothermel, M. Zuzic, A. Ivlev, and J. Goree, “Condensed Plasmas under Microgravity”, *Phys. Rev. Lett.* 83, 1598, 1999.
- Northrop, T. G. and Birmingham, T. J., “Plasma drag on a dust grain due to Coulomb collisions”, *Planet. Space Sci.* 38, 319, 1990.
- Nosenko, V., K. Avinash, J. Goree, and B. Liu, “Nonlinear Interaction of Compressional Waves in a 2D Dusty Plasma Crystal”, *Phys. Rev. Lett.* 92, 085001, 2004.
- Nosenko V., S. K. Zhdanov, S.-H. Kim, J. Heinrich, R. L. Merlino and G. E. Morfill, “Measurements of the power spectrum and dispersion relation of self-excited dust acoustic waves”, *Europhys. Lett.* 88, 65001, 2009.
- Nunomura, S., Samsonov, D., and Goree, J., “Transverse waves in a two-dimensional screened-Coulomb crystal (dusty plasma)”, *Phys. Rev. Lett.* 84, 5141–5144, 2000.

- Nunomura, S. Goree, J., Hu, S., Wang, X., and Bhattacharjee, A., “Dispersion relations of longitudinal and transverse waves in two-dimensional screened Coulomb crystals”, *Phys. Rev. E* 65, 066402, 2002.
- Olthoff, J. K., and Greenberg, K. F., “The Gaseous Electronics Conference RF Reference Cell—An Introduction”, *J. Res. Natl. Inst. Stand. Technol.* 100, 327, 1995.
- Pandey, B. P. and Dutta, A., “The Bohm criterion for a dusty plasma sheath”, *Pramana Vol.* 65, NO 1, 117-124, 2005.
- Peters, S., Homann, A., Melzer, A., and Piel, A., “Measurement of dust particle shielding in a plasma from oscillations of a linear chain”, *Phys. Lett. A* 223, 389–393, 1996.
- Piel, A., M. Klindworth, and O. Arp, “Obliquely Propagating Dust-Density Plasma Waves in the Presence of an Ion Beam”, *Phys. Rev. Lett.* 97, 205009, 2006.
- Pramanik, J., B. M. Veeresha, G. Prasad, A. Sen, and P. K. Kaw, “Experimental observation of dust-acoustic wave turbulence”, *Phys. Lett. A* 312, 84, 2003.
- Quinn R. A., and Goree, J., “Particle Interaction Measurements in a Coulomb Crystal Using Caged-Particle Motion”, *Phys. Rev. Lett.* 88, 195001, 2002.
- Rao, N. N., Shukla, P. K., and Yu, M. Y., “Dust-Acoustic Waves in Dusty Plasma”, *Planet. Space Sci.* 38, 543, 1990.
- Ratynskaia, S.V., Khrapak, S.A., Zobnin, A.V., Usachev, A.D., Yaroshenko, V.V., Thoma, M.H., Kretschmer, M., Quinn, R.A., Morfill, G.E., Petrov, O.F., Fortov, V.E., “Experimental Determination of Dust-Particle Charge in a Discharge Plasma at Elevated Pressures”, *Phys. Rev. Lett.* 93, 085001, 2004.
- Riemann, K., “The Bohm criterion and sheath formation”, *J. Phys. D: Appl. Phys.* 24, 493, 1991.
- Riemann, K., “The influence of collisions on the plasma sheath transition”, *Phys. Plasmas* 4, 4158, 1997.
- Roca i Cabarrocas, P., Gay, P., and Hadjadj, A., “Experimental evidence for nanoparticle deposition in continuous argon-silane plasmas: Effects of silicon nanoparticles on film properties”, *J. Vac. Sci. Technol. A* 14, 655, 1996.
- Rosenberg, M., “Ion- and dust-acoustic instabilities in dusty plasmas”, *Planet. Space Sci.* 41, 229, 1993.

- Rosenberg M., E. Thomas, Jr, and R. L. Merlino, “A note on dust wave excitation in a plasma with warm dust: Comparison with experiment”, *Phys. Plasmas* 15, 073701, 2008.
- Roth, J. R., “Industrial plasma engineering Volume 2: Application to nonthermal plasma processing”, *Institute of Physics Publishing, Bristol and Philadelphia*, 2001.
- Rothermel, H., T. Hagl, G. E. Morfill, M. H. Thoma, and H. M. Thomas, “Gravity Compensation in Complex Plasmas by Application of a Temperature Gradient”, *Phys. Rev. Lett.* 89, 175001, 2002.
- Samarian, A.A., and James, B.W., “Sheath measurement in rf-discharge plasma with dust grains”, *Physics Letters A* 287, 125–130, 2001.
- Samarian, A. A., and James, B. W., “Dust as fine electrostatic probes for plasma diagnostic”, *Plasma Phys. Control. Fusion* 47, B629–B639, 2005.
- Sato, N., G. Uchida, T. Kaneko, S. Shimizu, and S. Iizuka, “Dynamics of fine particles in magnetized plasmas”, *Phys. Plasmas* 8, 1786, 2001.
- Schollmeyer, H., Melzer, A., Homann, A., and Piel, A., “Dust–dust and dust - plasma interactions of monolayer plasma crystals”, *Phys. Plasmas* 6, 2693, 1999.
- Schwabe, M., M. Rubin-Zuzic, S. Zhdanov, H. M. Thomas, and G. E. Morfill, “Highly Resolved Self-Excited Density Waves in a Complex Plasma”, *Phys. Rev. Lett.* 99, 095002, 2007.
- Schwabe, M., Zhdanov, S. K., Thomas, H. M., Ivlev, A. V., Rubin-Zuzic, M., Morfill, G. E., Molotkov, V. I., Andrey M Lipaev, Vladimir E Fortov and Thomas Reiter, “Nonlinear waves externally excited in a complex plasma under microgravity conditions”, *New J. Phys.* 10, 033037, 2008
- Schweigert, V. A., I. V. Schweigert, A. Melzer, A. Homann, and A. Piel, “Alignment and instability of dust crystals in plasmas”, *Phys. Rev. E* 54, 4155, 1996.
- Selwyn, G. S., Heidenreich, J. E., and Haller, K. L., “Particle trapping phenomena in radio frequency plasmas”, *Appl. Phys. Lett.* 57, 1876 1990.
- Sheridan, T. E., Dusty plasma ring model, *Phys. Scr.* 80, 065502, 2009.
- Shukla, P. K., Mamun, A. A., “Introduction to Dusty Plasma Physics”, *Institute of Physics Publishing, Bristol and Philadelphia*, ISBN 0 7503 0653 X, 2002.
- Smith, B. A., *et al.*, “Encounter with Saturn: Voyager 1 Imaging Science Results”, *Science, New Series* 212, 163-191, 1981.

- Smith, B. A., *et al.*, “A New Look at the Saturn System: The Voyager 2 Images”, *Science, New Series* 215, 504-537, 1982.
- Smith Jr., B. A. T., “An Experimental Study of Phase Transitions in a Complex Plasma”, *Dissertation*, 2005.
- Sparks, M., Theory of Electron-Avalanche Breakdown in Solids, in Laser-Induced Damage in Optical Materials, edited by A. J. Glass and A. H. Guenther (National Bureau of Standards, Washington, D. C., *Special Publication* 435, 1975), p. 331v.
- Sukhinin G. I. and A. V. Fedoseev, “Influence of dust-particle concentration on gas-discharge plasma”, *Phys. Rev. E* 81, 016402, 2010.
- Teng, Lee-Wen, Mei-Chu Chang, Yu-Ping Tseng, and Lin I, “Wave-Particle Dynamics of Wave Breaking in the Self-Excited Dust Acoustic Wave”, *Phys. Rev. Lett.* 103, 245005, 2009.
- Thomas, E., Jr., R. Fisher, and R. L. Merlino, “Observations of dust acoustic waves driven at high frequencies: Finite dust temperature effects and wave interference”, *Phys. Plasmas* 14, 12370, 2007.
- Thomas E., Jr., “Driven dust acoustic waves with thermal effects: Comparison of experiment to fluid theory”, *Phys. Plasmas* 17, 043701, 2010.
- Thomas, H., Morfill, G.E., Demmel, V., Goree, J., Feuerbacher, B., Mlmann, D., “Plasma crystal: Coulomb crystallization in a dusty plasma”, *Phys. Rev. Lett.* 73, 652–655, 1994.
- Thomas, H. M., , Gregor E. Morfill, Alexei V. Ivlev, Anatoli P. Nefedov, Vladimir E. Fortov, Hermann Rothermel, Milenko Rubin-Zuzic, Andrey M. Lipaev, Vladimir I. Molotkov, Oleg F. Petrov, “PKE-Nefedov Complex Plasma Research on the International Space Station”, *Micrograv. Sci. Technol.* 16, 317-321, 2005.
- Thomas T., B. Dietmar, and P. Alexander, “Dust confinement and dust-acoustic waves in weakly magnetized anodic plasmas”, *Phys. Plasmas* 13, 042105, 2006.
- Thompson, C., A. Barkan, N. D’Angelo, and R. L. Merlino, “Dust acoustic waves in a direct current glow discharge ” *Phys. Plasmas* 4, 2331, 1997.
- Tomme, E. B., Law, D. A., Annaratone, B. M., and Allen, J. E., “Parabolic Plasma Sheath Potentials and their Implications for the Charge on Levitated Dust Particles”, *Phys. Rev. Lett.* 85, 2518–2521, 2000.
- Trottenberg, Th, A Melzer and A Piel, Measurement of the electric charge on particulates forming Coulomb crystals in the sheath of a radiofrequency plasma, *Plasma Sources Sci. Technol.* 4, 450458, 1995, Printed in the UK.

- Trottenberg, T., D. Block, and A. Piel, “Dust confinement and dust-acoustic waves in weakly magnetized anodic plasmas”, *Phys. Plasmas* 13, 042105, 2006.
- Tsyтович, V.N., Khodataev, Ya.K., Morfill, G.E., Bingham, R., Winter, D.J., “Radiative dust cooling and dust agglomeration in plasmas”, *Comments Plasma Phys. Control. Fusion* 18 281–291, 1998.
- Tsyтович, V. N., and de Angelis, U., “Kinetic theory of dusty plasmas. I. General approach”, *Phys. Plasmas* 6, 1093, 1999.
- Tsyтович V.N., U. de Angelis, R. Bingham, “Low-frequency responses and wave dispersion in dusty plasmas”, *Phys. Rev. Lett.* 87 185003/1-4, 2001.
- Tsyтович V.N., U. de Angelis, R. Bingham, “Low frequency responses, waves and instabilities in dusty plasmas”, *Phys. Plasmas* 9, 1079–1090, 2002.
- Vaulina, O. S., Lisin, E. A., Gavrikov A. V., Petrov, O. F., and Fortov, V. E., “Determination of Pair Interaction Forces between Particles in Nonideal Dissipative Systems”, *Phys. Rev. Lett.* 103, 035003, 2009.
- Vaulina O. S., and Lisin, E. A., “Technique for analysis of interparticle interaction in nonideal dissipative systems with isotropic pair potentials”, *Phys. Plasmas* 16, 113702, 2009.
- Vaulina, O. S., and Khrapak, S. A., “Scaling law for the fluid-solid phase transition in Yukawa systems (dusty plasmas)”, *JETP, Vol. 90*, No. 2, 287–289, 2000.
- Vladimirov, S.V., S.A. Maiorov, O. Ishihara, “Molecular dynamics simulation of plasma flow around two stationary dust grains”, *Phys. Plasmas* 10, 3867–3873, 2003.
- Wang, X., Bhattacharjee, A. and Hu, S., “Longitudinal and Transverse Waves in Yukawa Crystals”, *Phys. Rev. Lett.* 86, 2569-2572, 2001.
- Williams J. D., E. Thomas, Jr., “Initial measurement of the kinetic dust temperature of a weakly coupled dusty plasma”, *Phys. Plasmas* 13, 063509, 2006.
- Williams, J. D., E. Thomas, Jr., and L. Marcus, “Observations of vertically propagating driven dust acoustic waves: Finite temperature effects”, *Phys. Plasmas* 15, 043704, 2008.
- Williams, J. D. and Duff, J., “Observation of the coupling of the driven dust acoustic wave”, *Phys. Plasmas* 17, 033702, 2010.
- Wurden, G. A., Wurden, A. J., and Gladstone Jr., I. M., “Plasma Tails: Comets Hale-Bopp and Hyakutake”, *IEEE Trans. Plasma Sci.* 27, 142, 1999.

- Yaroshenko, V. V., Annaratone, B. M., Khrapak, S. A., Thomas, H. M., and Morfill, G. E., “Electrostatic modes in collisional complex plasmas under microgravity conditions”, *Phys. Rev. E* 69, 066401, 2004.
- Yaroshenko V V, F Verheest, H M Thomas and G E Morfill, “The Bohm sheath criterion in strongly coupled complex plasmas”, *New J. Phys.* 11 073013, 2009.
- Yaroshenko V. V., V. Nosenko, and G. E. Morfill, “Effect of strong electrostatic interactions of microparticles on the dust acoustic waves”, *Phys. Plasmas* 17, 103709, 2010.
- Zafiu, C., Melzer, A., and Piel, A., “Nonlinear resonances of particles in a dusty plasma sheath”, *Phys. Rev. E* 63, 066403, 2001.
- Zhang, Z., Kong, J., Qiao, K., Truell, H., and Matthews, L., “Simple method to measure the interaction potential of dielectric grains in a dusty plasma”, *Phys. Rev. E* 82, 036401, 2010.
- Zobnin, A.V., Nefedov, A.P., Sinelshchikov, V.A., Fortov, V.E., “On the charge of dust particles in a low-pressure gas discharge plasma”, *JETP* 91, 483–487, 1999.
- Zobnin, A.V., A.D. Usachev, O.F. Petrov, V.E. Fortov, “Dust–acoustic instability in an inductive gas-discharge plasma”, *JETP* 95, 429–439, 2002.